SSDC–DP–017

SPHEREx Explanatory Supplement

Version: 2.0

Authors:
SPHEREx Science Data Center Team: (Rachel Akeson, Gregory Dubois-Felsmann, Andreas Faisst, Tamim Fatahi, Tatiana Goldina, Yuna Kwon, Dan Masters, Christina Nelson, Roberta Paladini, Gaby Torrini, Phani Velicheti)

SPHEREx Science Team Contributors: (Matthew Ashby, Yoonsoo Bach, James Bock, Sean Bryan, Brendan Crill, Olivier Doré, C. Darren Dowell, Candice Fazar, Howard Hui, Phil Korngut, Chi Nguyen, Michael Werner, Michael Zemcov)

Contents

1 Mission Overview **4**
1.1 Mission Objectives . . . 4
1.2 Spacecraft . . . 4
1.3 Payload . . . 5
1.4 Survey Strategy and Spectral Accumulation . . . 7
1.5 Mission and Science Operations Summary . . . 9
1.6 Acknowledgments . . . 10

2 The SPHEREx Data Products **11**
2.1 Reprocessing and Quick Release Versions . . . 11
2.2 Spectral Images . . . 11
2.3 Image Anomalies and Features . . . 14
2.4 Known Limitations . . . 18

3 The SPHEREx Data Processing **21**
3.1 Data Ingestion and Raw Image Processing . . . 21
3.2 Processing Steps . . . 22
3.2.1 Source Blooming, Snowball and and Transient Halo Flagging . . . 22
3.2.2 Nonlinearity Correction . . . 26
3.2.3 Variance Map . . . 27
3.2.4 Persistence Masks . . . 28
3.2.5 Bad Pixel Flagging . . . 30
3.2.6 Dark Subtraction . . . 33
3.2.7 Absolute Gain Correction . . . 33
3.2.8 Astrometry . . . 33
3.2.9 Source Masks . . . 36
3.2.10 Outlier Pixel Detection . . . 39
3.2.11 Zodi Prediction . . . 39
3.2.12 Level 2 DQA . . . 40
3.3 Photometric Measurements . . . 40
3.4 Mosaics . . . 44
3.4.1 Overview . . . 44
3.4.2 Input Data . . . 44
3.4.3 Data Loading and Preprocessing . . . 44

3.4.4 Spectral Channel Definition . . . 45
3.4.5 Mosaic Grid . . . 45
3.4.6 Reprojection Algorithm . . . 46
3.4.7 Mosaic building process . . . 46
3.4.8 Output File . . . 47
3.4.9 Data Quality and Flagging . . . 48
3.4.10 Known Issues . . . 48

4 Calibrations **50**
4.1 Calibration Products . . . 50
4.1.1 Absolute Gain Matrix . . . 50
4.1.2 Effective Point Spread Function (ePSF) models . . . 50
4.1.3 Dark Current . . . 51
4.2 Calibration Procedures . . . 51
4.2.1 Photometric/Absolute Gain Calibration Derivation . . . 51
4.2.2 Astrometric Calibration Derivation . . . 54
4.2.3 PSF Measurement . . . 56
4.3 Additional Products and Inputs . . . 58
4.3.1 Spectral WCS . . . 59
4.3.2 Spectral Channels . . . 60
4.3.3 Atmospheric Templates . . . 65
4.3.4 Additional Products . . . 65

A Spectral Image Header Example **71**
A.1 Transient Flags . . . 77

B Absolute Gain Matrix Header Example **78**

C Average EPSF Header Example **79**

D List of Acronyms **81**

Change Record

Version	Date	Description	Owner
0.1	2025-04-03	Initial draft.	Yuna Kwon
1.0	2025-07-02	Quick-Release Version Release.	Yuna Kwon
1.1	2025-08-13	Add pipeline version information, additional links to IRSA resources and corrections to L2 DQA criteria	Yuna Kwon and Rachel Akeson
1.2	2025-08-29	Add table for pipeline versions, clarify role of WCS-WAVE and Spectral WCS files	Rachel Akeson
1.2.1	2025-10-03	Add table for photoemtry flag usage	Rachel Akeson, Dan Masters
1.3	2025-10-13	Add updated for quick release 2 version of data and calibrations	Rachel Akeson, Andreas Faisst, Dan Masters, Roberta Paladini
1.3.1	2025-12-25	Change in Spectral WCS for photometry tool	Rachel Akeson
1.4	2026-01-23	Updates for pipeline version 6.5 including: significant updates to decrease the number of fine astrometry failures, new flagging for blooming, snowballs and cosmic ray halos, changes to persistence, beamsplitter ghost masking, and an updated nonfunctional pixel map.	Rachel Akeson, Andreas Faisst, Dan Masters, Roberta Paladini
1.5	2026-03-30	Updates for pipeline version 6.5.6 which addresses an error in the header of the PSF layer extension in the SPHEREx Spectral Image FITS files.	Rachel Akeson
1.6	2026-05-06	New section on mosaics, including algorithmic description of tool at IRSA	Rachel Akeson
2.0	2026-08-25	Major update for pipeline version R7. Includes significant updates to the following modules: Persistence Masks, Bad Pixel Flagging, Fine Astrometry, Outliers Pixel Detection, Zodi Prediction, Photometric Measurements, Point Spread Function, Spectral Channels and the header examples	Rachel Akeson, Andreas Faisst, Dan Masters, Roberta Paladini

(Document generated on September 2, 2026 from commit v1.0 of 2025-07-02.)

1 Mission Overview

1.1 Mission Objectives

The Spectro-Photometer for the History of the Universe, Epoch of Reionization, and Ices Explorer (SPHEREx) is a NASA Astrophysics Medium-class Explorer (MIDEX) mission, designed to perform the first all-sky spectral survey in the optical to Near-infrared (NIR) range, covering wavelengths from 0.75 to 5.0 μm. SPHEREx launched on 12 March 2025 at 03:10:12 UTC aboard a SpaceX Falcon 9 rocket from Vandenberg Space Force Base.

On May 1, 2025, the spacecraft began regular science operations following an In-Orbit Checkout (IOC) period during which the flight and ground systems were commissioned, and key survey parameters were optimized. Over its nominal 25-month science mission, SPHEREx will conduct four complete sky surveys, yielding 1.4 trillion spectral-spatial elements (voxels) per all-sky pass. The mission will construct a comprehensive three-dimensional cosmos map, enabling transformative insights into the origin and evolution of the universe. The mission addresses three principal science themes aligned with NASA's strategic astrophysics priorities [Bock et al., 2026]:

- **Probing Inflation and the Early Universe:** SPHEREx will acquire low-resolution spectra for over 450 million galaxies, enabling a three-dimensional reconstruction of the large-scale structure of the Universe across an unprecedented cosmological volume. These data will constrain primordial non-Gaussianity via the $f_{\rm NL}$ parameter, with a target sensitivity of $\sigma(f_{\rm NL}) \leq 1$, providing critical tests to distinguish between single- and multi-field inflationary models.
- **Tracing the Origin of Planetary Systems and Biogenic Ices:** SPHEREx will perform the largest spectroscopic survey of ice absorption features in circumstellar environments, observing young stellar objects, protoplanetary disks, and molecular clouds throughout the Milky Way. The mission will collect over 20,000 high-quality ice spectra, enabling statistically robust correlations between ice composition and environmental conditions.
- **Exploring Galaxy Evolution via the Extragalactic Background Light (EBL):** Through deep spectral imaging of the ecliptic poles, SPHEREx will measure spatial power spectra of EBL fluctuations. These data will disentangle the contributions of intra-halo light, faint dwarf galaxies, and sources from the Epoch of Reionization, providing new constraints on early galaxy populations and the cosmic star formation history.

In addition to its primary science objectives, SPHEREx will generate an archival dataset capturing a diverse range of astronomical phenomena [Crill et al., 2020, Ivezić et al., 2022, Bock et al., 2026], including:

- $\gtrsim$1 billion galaxy spectra
- $\gtrsim$450 million galaxy redshifts
- $\gtrsim$1 million quasar spectra
- $\gtrsim$100 million stellar spectra
- $\gtrsim$600,000 exoplanet target stars
- $\gtrsim$700,000 ice absorption spectra
- $\gtrsim$100,000 asteroid and comet spectra

1.2 Spacecraft

The SPHEREx spacecraft is based on the Ball Configurable Platform (BCP-100) bus, previously utilized in missions such as Imaging X-ray Polarimetry Explorer (IXPE) [Weisskopf et al., 2022]. Designed for operations in low Earth orbit (LEO), the platform delivers high pointing accuracy, thermal stability, and efficient data throughput.

Throughout the SPHEREx mission, the spacecraft operates in a sun-synchronous polar orbit. SPHEREx's operations are governed by geometric pointing constraints to mitigate Sun, Earth, and Moon contamination. Key spacecraft orbital parameters are summarized in Table 1.

It achieves high-precision three-axis stabilization through a combination of star trackers, a gyro-based Scalable Space Inertial Reference Unit (SSIRU), GPS, four reaction wheels, and three magnetic torque rods. Telemetry and command operations utilize the S-band for uplink (2 kbps) and low- or high-rate telemetry (32 kbps and 2 Mbps, respectively), while science data are transmitted via Ka-band downlink at 600 Mbps. Power is supplied by a body-fixed solar array paired with a 22.5 Ah lithium-ion battery, providing uninterrupted operation even during eclipse seasons. An onboard recorder stores up to eight days of science data (approximately 1074 Gbits), ensuring robust data capture between ground contacts.

Table 1: Orbital parameters of the SPHEREx spacecraft

Property	**Value**
Mean semi-major axis	7,037.41 km
Eccentricity	0.00034
Inclination	97.951°
Longitude of ascending node	27.06°
Argument of periapsis	121.8°
Time to periapsis	1,987 sec
Mean Local Time of Ascending Node (MLTAN)	6:00 AM
Orbital period	98 min

Key spacecraft functionalities are provided by the following subsystems: the Attitude Determination and Control Subsystem (ADCS), which maintains precise orientation; the Command and Data Handling (CDH) subsystem, including spacecraft avionics; Flight Software (FSW), responsible for receiving and executing survey sequences, as well as spacecraft control; the Electrical Power Distribution Subsystem (EPDS), which ensures continuous power delivery; the Telecommunications subsystem, supporting uplink and downlink operations; the Thermal Control subsystem, maintaining operating temperatures for critical electronics; and the Spacecraft Structure, which supports both the spacecraft bus and payload.

The spacecraft is not equipped with onboard propulsion. Consequently, orbital decay follows the natural evolution of the orbit, predominantly influenced by atmospheric drag. End-of-mission de-orbiting is achieved passively, with atmospheric re-entry expected within 25 years following the conclusion of science operations.

Detailed descriptions of each subsystem and its associated software architectures are provided in Alibay et al. [2023].

1.3 Payload

The SPHEREx payload includes a wide-field cryogenically cooled telescope and spectrophotometric imaging system optimized for spectral mapping. It features a 20-cm effective aperture, all-aluminum free-form Three Mirror Anastigmat (TMA) telescope with a broad Field of View (FoV) of 3.5° × 11.3°. The optical path is split by a dichroic beam splitter, allowing simultaneous observations in short- and mid-wave infrared bands. The entire assembly is thermally isolated from the spacecraft to maintain radiometric stability. With no moving parts beyond the one-time deployment of an aperture cover during IOC, the design emphasizes robustness, maximizing spectral throughput and operational reliability. A schematic illustration of the optical light path and an example of Linear Variable Filter (LVF) spectroscopy toward the Andromeda Galaxy are shown in Figure 1. Animation illustrating collecting signals through LVF is available on the SPHEREx/California Institute of Technology (Caltech) official website[1].

The SPHEREx instrument is organized into three primary subsystems: the optical subsystem (telescope, beam splitter, and Focal Plane Assemblies (FPA)s), the thermal subsystem (passive radiative cooling structure), and the Instrument Control Electronics (ICE) electronics (detector readout, onboard processing, and storage management)[Korngut et al., 2026].

Cryogenic telescope and detector temperatures are achieved entirely through passive means. A three-stage V-groove radiator system, comprised of nested conical photon shields, supplemented by a dedicated focal plane radiator, effectively dissipates heat to space, reducing telescope thermal emission, suppressing

[1] https://spherex.caltech.edu/page/survey

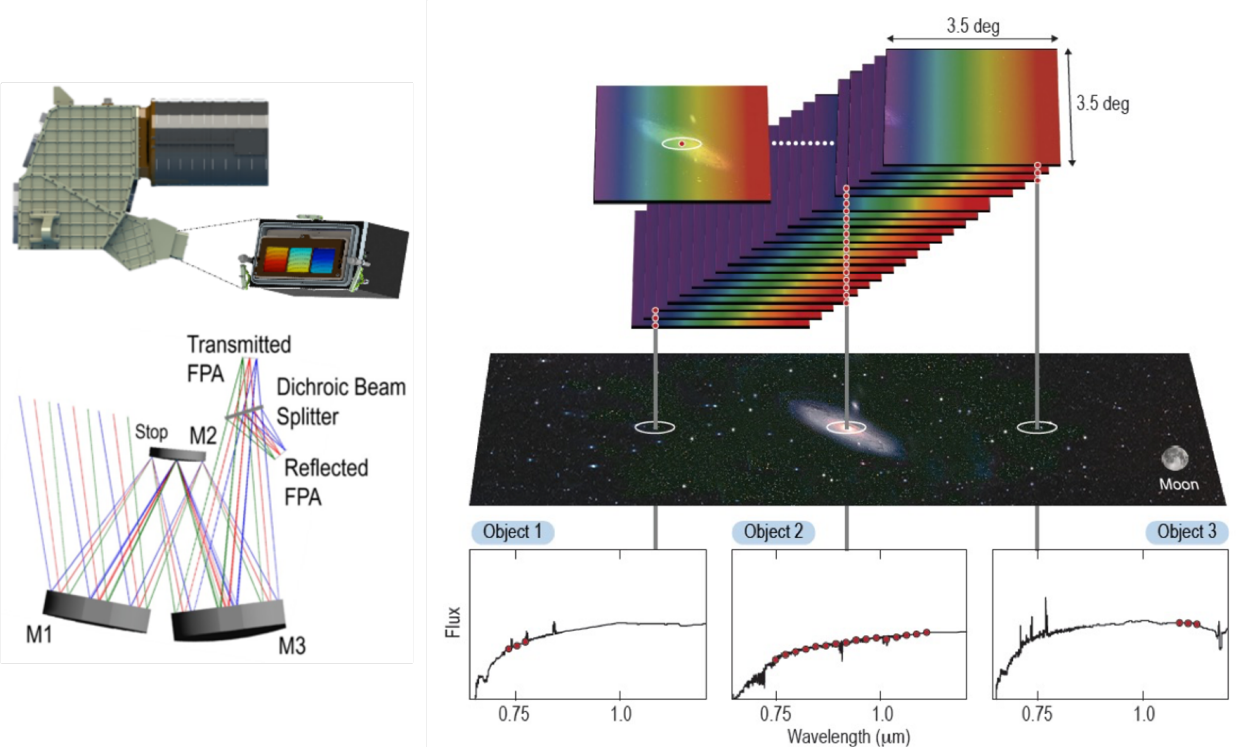

Figure 1: Light path through the SPHEREx optical system and an example illustration of LVF spectroscopy targeting the Andromeda Galaxy. (Credit: Image courtesy of SPHEREx-JPL/Caltech)

detector dark current and facilitating thermal stability throughout the mission. Key instrument parameters are summarized in Table 2 [Bock et al., 2026] and the normalized spectral resolution is shown in Figure 2. Figure 3 presents the preliminary expected all-sky point source sensitivity after four full-survey passes, assuming a median sky background photocurrent.

Table 2: SPHEREx Instrument Parameters

Parameter	**Value**
Effective aperture	20 cm
Focal ratio	f/3
Field of view	$2 \times (3.5° \times 11.3°)$; dichroic split
Wavelength coverage and design resolution	0.744–5.002 μm
• Band 1: $\lambda = 0.744$–1.116 μm; $R = 39$	
• Band 2: $\lambda = 1.099$–1.651 μm; $R = 41$	
• Band 3: $\lambda = 1.636$–2.421 μm; $R = 41$	
• Band 4: $\lambda = 2.423$–3.822 μm; $R = 35$	
• Band 5: $\lambda = 3.809$–4.420 μm; $R = 112$	
• Band 6: $\lambda = 4.412$–5.002 μm; $R = 128$	
Detectors	3× Hawaii-2RG 2.6 μm cutoff 3× Hawaii-2RG 5.3 μm cutoff
Read mode	Sample-Up-the-Ramp (SUR)
Frame time	1.5349 s
Exposure time	113.58 s
Pixel scale	$6.15'' \times 6.15''$

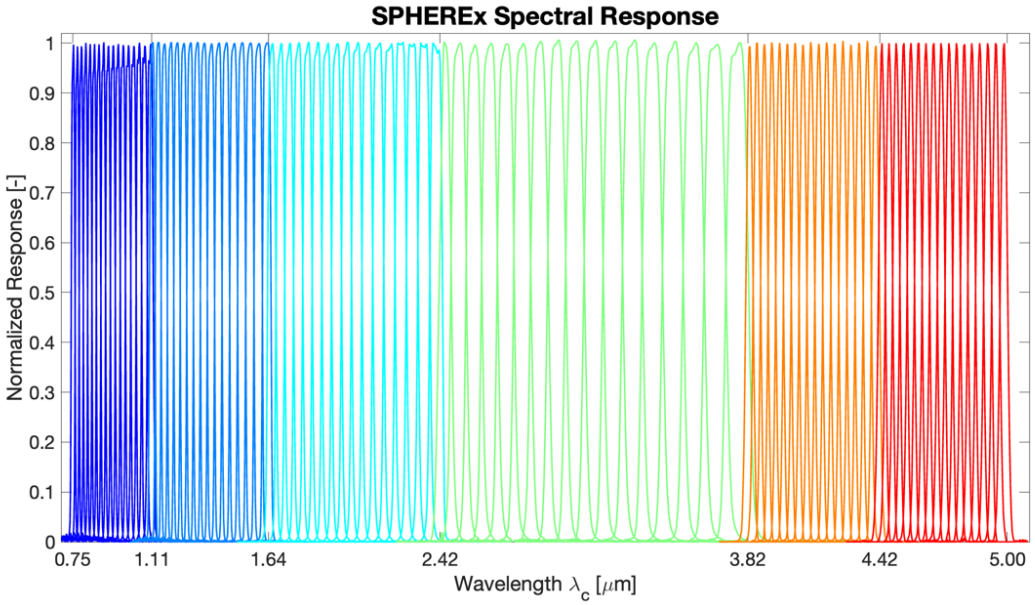

Figure 2: The measured normalized spectral response across the SPHEREx wavelength range.

The focal plane is divided into two FPAs, each consisting of three Teledyne H2RG HgCdTe 2k × 2k detector arrays. A dichroic beam splitter separates the short-wavelength and long-wavelength channels: the Short-wave Infrared (SWIR) FPA covers 0.75–2.44 μm (in reflection) and operates at 62 K, while the Mid-wave Infrared (MWIR) FPA spans 2.40–5.01 μm (in transmission) and operates at 45 K. Each detector is paired with an LVF, positioned above the array, which allows each pixel to sample a narrow spectral bandpass. As the sky drifts across the field of regard given Earth-, Sun-, and Moon- avoidance constraints, successive exposures at offset positions reconstruct full low-resolution spectra for each celestial source.

The detectors employ SUR readout mode to optimize Signal-to-Noise (S/N) performance. Custom-built Video8 Application-Specific Integrated Circuit (ASIC) boards, developed by SPHEREx/Caltech, perform low-noise readout, real-time photocurrent estimation, and onboard data compression. The ICE system manages digitized sample processing and compression before transferring the data to dedicated onboard storage for subsequent downlink. Detailed specifications of the detectors are provided in Crill et al. [2020], and further descriptions of the ICE hardware and firmware can be found in Korngut et al. [2026].

1.4 Survey Strategy and Spectral Accumulation

SPHEREx takes observations that deliver the required all-sky and deep field coverage. We plan these observations using the Survey Planning Software (SPS) developed for SPHEREx. Unlike other surveys with repeating geometric scan strategies, the unique requirements of the SPHEREx mission led us to develop the SPS to plan observations on-the-fly that deliver high time on science and high sky coverage. More details are available in Bryan et al. [2026]. Among other capabilities, the SPS plans science observations, pauses observations for downlinks, mitigates outages due to passage through the elevated radiation environment of the South Atlantic Anomaly, plans slews to avoid bringing the telescope close to the Moon while slewing, and selects a safe place to point in rare cases when no science targets are observable.

The SPS only plans observations that are in the allowable pointing zone. Operating from low-earth orbit, the SPS plans attitudes for SPHEREx that avoid pointing near the Sun, Moon, and Earth. The SPS also keeps the solar panel pointed close enough to the Sun to meet power requirements. To mitigate the shuttle glow observed in flight during experiments conducted in IOC, the SPS also avoids pointing the telescope near the direction of flight. Taken together, these constraints define the time-varying allowable pointing zone.

SPHEREx has a single main target list that includes targets from the all-sky survey as well as targets in both deep fields. All targets are organized into *target groups*. To move to a desired target group,

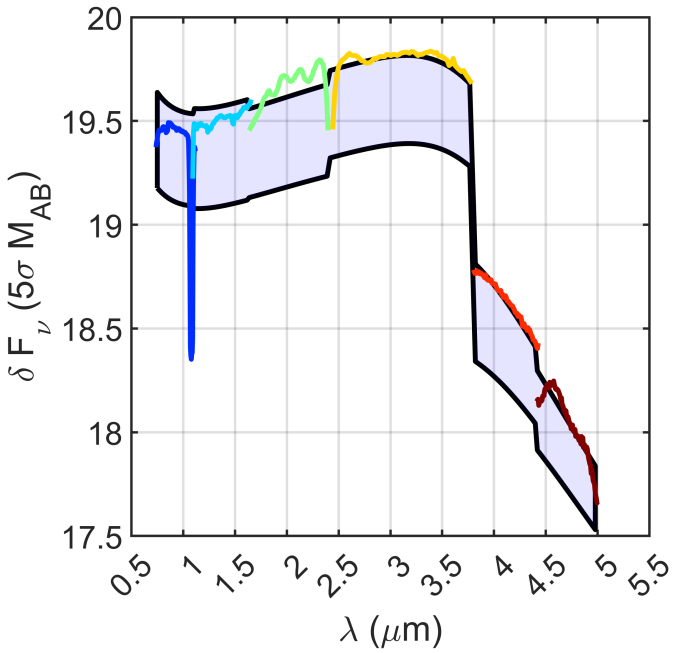

Figure 3: Projected all sky sensitivity based on flight performance assuming 4 observations per wavelength and the median measured photocurrent across the sky. The colored lines indicate the wavelength range covered in each of the six bands. The gray area encompasses the projected mission sensitivity and uncertainty at the time of submission of the SPHEREx concept study report in 2018. In all cases other than the helium contaminated 1.083 μm channel, the actual performance is as-good-as or better than the original projected performance estimates. Figure from Korngut et al. [2026].

SPHEREx executes a *large slew* maneuver. After the observatory settles at this attitude, SPHEREx takes a single exposure, then executes a *small slew* maneuver to the next target in the group, and continues taking exposures followed by small slews until the target group is about to move out of our allowable pointing zone. The SPS then plans a large slew to the next target group, and observing continues in this way throughout our science operations. To plan these slews efficiently, the SPS selects the sequence of target groups to minimize the number of time-expensive large slews and maximize the number of observations made within a target group before it moves out of the allowable pointing zone.

A single target group consists of 17 pointings at an identical ecliptic longitude and spaced by one channel width in ecliptic latitude. For any single spectral channel, completing a target group yields a square region of full coverage in that single spectral channel. To achieve full coverage in all spectral channels across the entire sky, we distribute these target groups in a great circle around the equator at all longitudes to form a single latitude ring (Fig. 4). We construct similar latitude rings at great circles at all latitudes, naturally with fewer target groups in the latitude rings at higher latitudes. To mitigate pointing error as well as distortion in the optical system, we overlap the latitude rings, and also overlap the target groups within each latitude ring. This yields an All-Sky target list that achieves full spectral and spatial coverage, efficiently distributes observing time evenly in solid angle across the sky, and contains overlap as mitigation and redundancy.

To efficiently align all observations in the All-Sky Survey, the observatory is always rotated about the telescope boresight such that the wide axis of the field of view aligns with lines of constant ecliptic latitude. This rotation angle is the ecliptic Position Angle (PA) of the observatory, and is measured relative to the line of constant ecliptic latitude passing through the telescope boresight. To meet the solar panel illumination requirements, during ascending halves of the orbit we align the observatory with a PA of 0°, and during descending halves of the orbit the observatory is aligned with a PA of 180°. This also plays a key role in the definition of the surveys. Survey 1 is composed of data taken during the first 12.5 months of science operations with PA = 0°, Survey 2 is composed of data taken during the first 12.5 months of science operations with PA = 180°, Survey 3 is composed of data taken during the second 12.5 months of science operations with

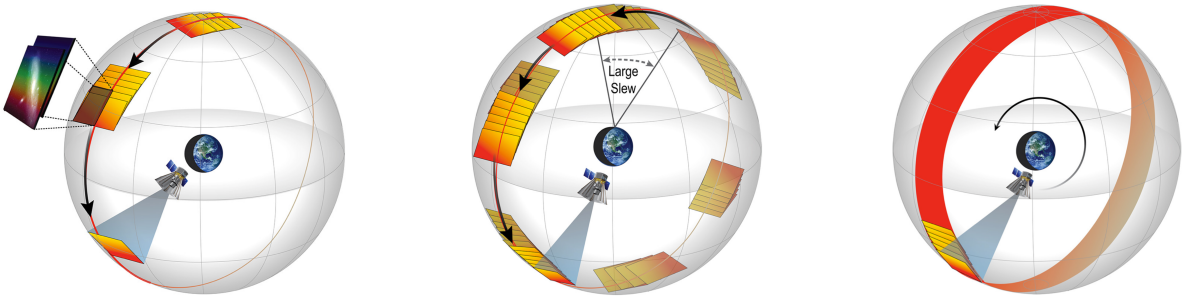

Figure 4: SPHEREx completes full spectral sampling near the terminator, governed by multiple pointing constraints. As the orbit progresses, the observable arc of sky gradually rotates, enabling full-sky spectral coverage twice every year. Throughout the mission, SPHEREx will accumulate approximately 5×10^{12} spatial-spectral elements. (Credit: Image courtesy of SPHEREx-JPL/Caltech)

PA = 0°, and Survey 4 is composed of data taken during the second 12.5 months of science operations with PA = 180°.

Each target in the All-Sky Survey is spaced by an angle on the sky that corresponds to one spectral channel in the LVF. To enable internal data consistency checks and to ensure full spectral coverage even of narrow spectral features, Surveys 3 and 4 are shifted on the sky relative to Surveys 1 and 2 by an angle on the sky that corresponds to half of a spectral channel. This shift Nyquist-samples the spectra taken across the entire sky, twice, when data is combined across the full mission.

SPHEREx conducts a Deep Survey to collect data to achieve our galaxy formation science goals. One field is located at the north ecliptic pole, and the other is located near the south ecliptic pole. The southern deep field is offset slightly from the pole to avoid foregrounds and bright stars. The Deep Survey target list was developed to meet the power spectral sensitivity required by the extragalactic background light investigation. The strategy was to design a repeatable tiling pattern that, together with the sky rotation observed at the poles across the year from our sun-synchronous orbit, would achieve the required coverage. The pointing targets that make up this pattern at each pole are generated by a separate tool from the core survey software. The pattern is constructed by stepping the boresight along the spectral direction to create target groups similar to those in the All-Sky Survey. Unlike the All-Sky Survey, in the Deep Survey target list, these target groups are highly overlapping to yield deep repeated coverage.

1.5 Mission and Science Operations Summary

SPHEREx is a collaborative mission involving multiple institutions, with mission operations led by Jet Propulsion Laboratory (JPL) in Pasadena, California. The mission is led by Principal Investigator (PI) Dr. Jamie Bock based at Caltech, which was also responsible for the payload development in partnership with JPL. The spacecraft and telescope were designed, constructed, and tested by BAE Space and Mission Systems (BAE), which also led observatory-level integration and testing. The payload, including the telescope, optics, and focal plane assemblies, as well as the passive thermal control subsystem, was designed, integrated, and tested by Caltech and JPL. The Korea Astronomy and Space Science Institute (KASI) contributes as an instrument and science partner, and provides a specialized cryogenic testing chamber for instrument testing. Science data processing is managed by the SPHEREx Science Data Center (SSDC) at Caltech/IPAC, with long-term data archiving handled by the NASA/IPAC Infrared Science Archive (IRSA). The SPHEREx Science Team (SST), composed of researchers from Caltech, JPL, KASI, and numerous partner institutions, is responsible for scientific analysis across SPHEREx's three primary themes (Sect. 1.1).

The Mission Operations Team manages mission operations, including command sequencing and flight system performance monitoring. It also oversees the operation of the SPS, which was provided by Arizona State University. Spacecraft communications are executed via NASA's Near Space Network (NSN) ground stations using S-band (low rate uplink and downlink) and Ka-band (high rate downlink). Science data

and select telemetry are routed to the SSDC. There, data are depacketized, calibrated, and processed for scientific use. The SSDC also implements algorithms developed in collaboration with the PI and SST to produce the data processing pipeline and data products described in Sections 2 and 3.

The Mission Operations Team at JPL is responsible for running the SPS and Planning Generation and Simulation Operations (PGSO) and uplinking the resulting command sequences to the spacecraft. In general, two survey plans are loaded per week, and these plans are designated by the week of the year (e.g., Week 20 in 2025 `2025W20`), whether a given plan is the first or second half of the week (1 or 2) and a letter designating the version (`A`, `B`, etc.), resulting in a final name of, e.g. `2025W20_2B`. Note that the first plan of the science survey (`2025W17_4B`) has a 4 instead.

1.6 Acknowledgments

If you use data from SPHEREx in a publication, please include the following acknowledgment:

This publication makes use of data products from the Spectro-Photometer for the History of the Universe, Epoch of Reionization and Ices Explorer (SPHEREx), which is a joint project of the Jet Propulsion Laboratory and the California Institute of Technology, and is funded by the National Aeronautics and Space Administration.

2 The SPHEREx Data Products

This document provides a comprehensive overview of the SPHEREx Quick Release (QR) data products and Data Release (DR) products. The data processing pipeline and calibrations used for both the QR products and DR products continues to evolve and improve as the mission proceeds. To access SPHEREx data, see `https://irsa.ipac.caltech.edu/Missions/spherex.html`, which includes links to the available data search, visualization, and download options.

Figure 5 illustrates the data processing flow and the associated data products. Main data products, shown in green, will be publicly distributed via IRSA and are described in detail in their respective sections, as noted by reference numbers shown in parentheses. Ancillary or intermediate products, shown in orange, are generated during internal processing and either contribute to the creation of the main products or are embedded within them (e.g., as layers in Multi-Extension FITS (MEF) files). Data pre-processing and product generation steps, shown in pink, are elaborated in Section 3.2. Arrows in the diagram indicate the directional flow of data, emphasizing the transformation from raw telemetry to science-ready outputs.

2.1 Reprocessing and Quick Release Versions

The calibrated spectral images are produced within a few days of data acquisition and are available at IRSA within 60 days of observation. Following the completion of Year 1 (includes survey 1 and survey 2 = DR1) and Year 2 (includes survey 1 to survey 4 = DR2), all SPHEREx science data will undergo a complete reprocessing using the most up-to-date version of the Level 1-3 pipeline. These reprocessings will incorporate the best available calibrations, processing parameters, and updated algorithms based on analysis of the initial processing results. Year 1 (DR1) and Year 2 (DR2) releases will also include additional data products and this document will be updated accordingly once those data are released.

While the original plan did not include a reprocessing of quick release data before the Year 1 reprocessing, the SPHEREx team made significant updates to the calibrations based on the first few months of science survey data and the SSDC has utilized these updates to perform a reprocessing of data collected between the start of the science survey and October 2025. These data are available in IRSA as QR2 and this document has been updated accordingly. While the previous version of data (now labeled QR1) will be available to download, we strongly encourage all users to switch to using QR2 data, given the calibration improvements, particularly the PSF (sec. 4.2.3) and absolute gain calibration (sec. 4.2.1). The QR2 files correspond to pipeline versions from 6.4 to 6.5.6 and the full list of updated calibrations is in Table 4. Due to improved calibrations and their impact on data quality, the exact file list for QR1 and QR2 is slightly different and science users should NOT combine files from the two releases.

For the Year 1 reprocessing which produced the DR1 products, a major update of the pipeline was undertaken, corresponding to pipeline versions R7.0 and up. Details are included in the subsections below and include significant updates to Persistence Masks, Bad Pixel Flagging, Fine Astrometry, Outliers Pixel Detection, Zodi Prediction, Photometric Measurements, and derivation of the Point Spread Function. Additionally, the absolute gain and spectral calibrations have been updated. Calibrated images using this version of the pipeline (referred to as R7) are labeled as DR1 for reprocessed survey 1 and 2 data and QR3 for survey 3 and 4 data. The first several weeks of survey 3 and 4 data (May 16, 2026 to July 19, 2026) were initially processed with pipeline version 6.5.6 and the QR3/R7 versions will be released in the archive with the DR1 data in late fall 2026. Due to the change in calibrations, we advise caution when combining QR2 and QR3 data. The spectrophotometry tool has been updated to apply the new gain calibrations to QR2 data.

2.2 Spectral Images

Spectral image files are produced by the SSDC Level 2 pipeline for each sky pointing and detector. While no zodiacal light subtraction is applied, each file includes an estimated background level (using the model described in Crill et al. [2025]) to support downstream analysis. These products are released to the public as part of the QR process within 60 days of on-orbit acquisition. In addition, all spectral images collected to date will be re-processed and re-released during the annual Data Releases after the completion of Years 1 and 2.

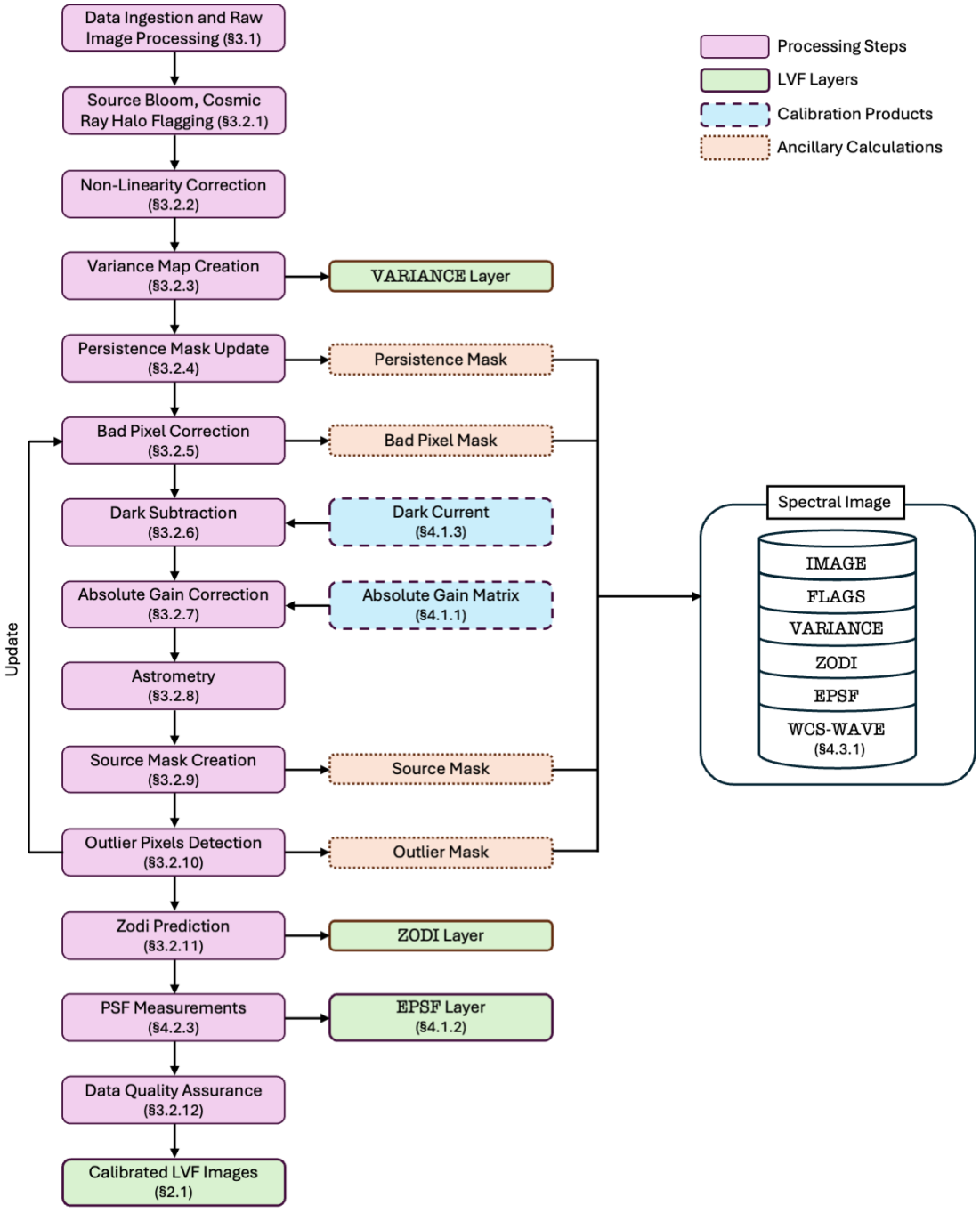

Figure 5: SPHEREx data processing flowchart and associated products. Pink boxes represent individual data processing steps. Green boxes with bold outlines denote data products that include layers of spectral images. Orange boxes with dotted outlines indicate ancillary calculations used in or derived from the main processing pipeline. Blue boxes with dashed outlines correspond to calibration products. Arrows illustrate the flow of inputs and outputs between components. Section numbers in parentheses refer to detailed descriptions in the text. Layer information for a multi-extension spectral image is shown.

Filename Convention Each spectral image file is named according to a standardized convention that encodes the observation ID (including survey planning period, and large and small slew counters), detector number, and Header and Data Unit (HDU) processing time. Table 3 provides a representative example of the filename structure and its components. Each large slew has a maximum of 4 small slews, so the allowed small slew counter range is 1 to 4. Some large slews will have less than 4 small slews.

Table 3: Example of filename convention

ID Type	**String form**
Full image name	level2_2025W22_2B_0001_1D3_spx_l2b-v4-2025-152.fits
Observation ID	2025W22_2B_0001_1
• Survey Planning Period	2025W22_2B
• Large Slew Counter†	0001
• Small Slew Counter‡	1
Detector #	3
Processing Time	2025-152 (152nd day of the year 2025)

Notes: †: Starts from 0, ‡: Starts from 1.

Data Format Each spectral image is stored as an MEF file comprising six HDUs: five image extensions and one binary table. The contents of each extension are as follows:

- **IMAGE** Calibrated surface brightness flux in scientific units (MJy/sr), stored as a 2,040 × 2,040 pixel array.
- **FLAGS** Bitmap of per-pixel status and processing flags, also 2,040 × 2,040 in size. (Sects. 3.2.5, 3.2.9, 3.2.10)
- **VARIANCE** Per-pixel variance estimate in units of $(\mathrm{MJy/sr})^2$, provided in a 2,040 × 2,040 array. (Sect. 3.2.3)
- **ZODI** Model-estimated zodiacal light background in units of MJy/sr, given as a 2,040 × 2,040 array. (Sect. 3.2.11)
- **EPSF** Image cube of over-sampled ePSFs, provided as 441 rows, representing a 21 × 21 grid for detectors 1, 2, 4, 5 and 6 and with 451 rows representing a 11 × 41 grid for detector 3. Point Spread Function (PSF) is normalized to its integral and dimensionless. (Sect. 4.2.3).
- **WCS-WAVE** Spectral World Coordinate System (WCS) lookup table mapping pixel coordinates to central wavelengths and bandwidths, formatted as a binary table with 3 columns and 1 row. (Sect. 4.3.1). The fidelity of this lookup table is suitable for visualization, but for science analysis, the Spectral WCS files (Sec. 4.3.1) should be used.

A python notebook assembled by IRSA demonstrates how to explore these images extensions, see `https://caltech-ipac.github.io/irsa-tutorials/tutorials/spherex/spherex_intro.html`.

Note on PSF layer header issue in QR2 files In the original release of spectral image files for QR1 and QR2, there is an error in the header description. This issue impacts both the stand-alone PSF calibration product and the PSF layer in the individual files.

The PSF cube planes are stored in order of increasing x-index across the grid, but the header incorrectly indicates increasing y-index. As a result, software that relies on the header information to select a PSF for a given location on the detector may retrieve the wrong PSF cube plane. The magnitude of this error depends both on the source location and the variation of the PSF across the detector. The error is largest in two of the corners and can result in a photometry error of +/-5% as compared to using the correct PSF.

As of March 31, 2026, QR2 files available at IRSA have been corrected for this issue. Files with pipeline versions from 6.4 to 6.5.5 have the suffix "+psffix1" appended to indicate corrected files. Files with pipeline

version of 6.5.6 and greater were processed with the correct header already. IRSA hosts a python tutorial notebook which provides a method to fix locally stored files and explains how to retrieve the PSF and the version of the image products. New versions of the Exposure-averaged PSF calibration product are available at IRSA, but the reference string for the calibration in the spectral image FITS header has not been updated. More information can be found in the PSF Erratum webpage. Note that this issue does not apply to QR3 or DR1 calibrated images.

Image Header Description The header of a spectral image file encodes key metadata used for identification, calibration tracking, and scientific analysis. Key fields include the observation ID, detector number, product creation time, exposure start time (in UTC), and total exposure duration. Astrometric metadata, such as coordinate system definitions and optical distortion parameters, are also recorded to support accurate spatial registration. Each file header contains unique identifiers for the calibration products applied during processing, along with an approximate mapping between pixel coordinates and their corresponding central wavelengths. Additional metadata relevant to downstream analysis includes spacecraft and instrument parameters – for example, mean detector array and telescope mirror temperatures during the exposure.

The header also includes information on the planned pointing for the telescope boresight (`SPS_LON_ECL`, `SPS_LAT_ECL`, and `SPS_PA_ECL`) in ecliptic coordinates as specified in the survey plan. These values are the same for all 6 bands in each observation. The `SPS_PA_ECL` keyword can be used to determine which survey a given observation belongs to:

- From $t = 0$ to 12.5 months, all-sky data taken with PA = 0 is Survey 1
- From $t = 0$ to 12.5 months, all-sky data taken with PA = 180° is Survey 2
- From $t = 12.5$ to 25 months, all-sky data taken with PA = 0 is Survey 3
- From $t = 12.5$ to 25 months, all-sky data taken with PA = 180○ is Survey 4

The pointing targets for Surveys 3 and 4 are shifted by 6′ with respect to Surveys 1 and 2 to provide finer spectral sampling.

The RA and DEC calculated per band as part of the astrometric calibration (Sect. 3.2.8) are available in the standard `CRVAL1` and `CRVAL2` keywords. The header also records the full list of data processing modules executed to generate the file, including associated software versioning. A representative header structure is shown in Table A.35, with all entries specific to the illustrated example.

In spectral image files, the long-keyword convention (`HIERARCH`)[2], originally developed by the European Southern Observatory (ESO), is used to support header keywords that exceed the standard 8-character Flexible Image Transport System (FITS) limit. This convention ensures compatibility with automated metadata parsing during file ingestion and analysis. The `IMAGE` extension contains a WCS header that provides an approximate pixel-to-wavelength mapping.

Data Product Size Each spectral image file is approximately 67 MB in size.

2.3 Image Anomalies and Features

A small percentage of the SPHEREx on-sky data show a range of image artifacts, atmospheric features, and anomalies. Some of these were predicted before launch, while others are stronger or more frequent. A list of these issues is given below, along with example images. Later versions of the SPHEREx data pipeline will address some of these issues. A list of images where the substantial portion of the image is contaminated is maintained at `https://spherex.caltech.edu/page/anomalyimages`.

Anomalies Defined as signals that originate from the behavior of the optics or detectors, or from interactions with cosmic rays or other particles.

- **Frame edge ghost (Fig. 6 left):** Sources which are focused into a narrow 'frame edge' region just outside the detector FoV can scatter light into the detector active area. This ghost has a roughly

[2] `https://fits.gsfc.nasa.gov/registry/hierarch_keyword.html`

triangular shape and can be produced by any of the four edges of each detector. Due to the precise positioning during sequences of small slews, ghosts on the left or right edge can appear in multiple exposures.

- **Linear bright source ghost (Fig. 6 center):** Very bright sources off the top or bottom of the detectors can produce linear ghosts as shown in the figure. This ghost is stronger in the longer wavelength bands and does not depend on the precise positioning of the source.
- **Beam splitter ghost (Fig. 6 right):** Very bright sources can show a reflection from the Dichroic Beam Splitter (DBS) consisting of a $\sim 10'$ diameter disk. The ghost is most prominent in the beam splitter transition region near the wavelength boundary of Bands 3 and 4, but the ghost is also present at lower levels elsewhere in Bands 3–6.

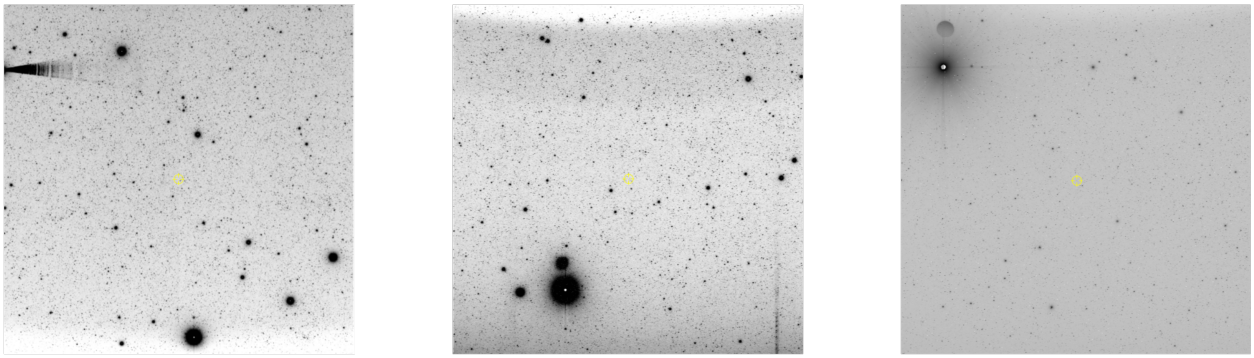

Figure 6: Left: Example of a frame edge ghost (top left of image). Center: Example of a linear bright source ghost (lower right corner). Right: Example of a beam splitter ghost (upper left corner).

- **8° ghost (Fig. 7 left):** A stray light artifact produced by very bright stars approximately 8° from the centers of Bands 2 to 6 has been found in a fraction of exposures in those bands.
- **Moon stray light feature at detector edge (Fig. 7 right):** A fraction of exposures in Bands 1, 4, 5, and 6 show excess emission at the left or right edges, believed to be attributable to stray light when the Moon illuminates the telescope assembly.

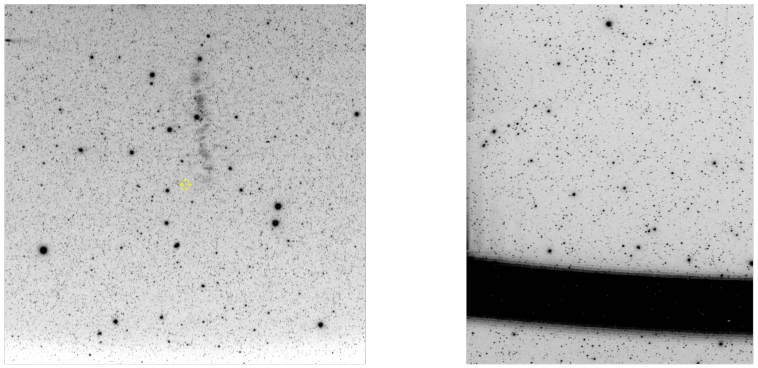

Figure 7: Left: In the upper middle of exposure, a complex and diffuse stray light artifact produced in Band 4 by a very bright star approximately 8° away. Right: Excess emission along the lower left edge of a Band 1 exposure, caused by Moon stray light. (The brighter, horizontal band is the 1.083 μm atmospheric He line.)

- **Extended cosmic ray signatures:** Every SPHEREx image includes detector pixels impacted by cosmic rays. The vast majority of these events directly impact only one pixel, and above a threshold of $\sim$100 photoelectrons, the cosmic ray signal is removed by the onboard transient detection. However, as with other missions such as JWST, many of the cosmic rays also affect neighboring pixels, including

ones that do not trigger the transient detection. Electrical crosstalk to nearest neighbors is one common path to an extended cosmic ray signature (Fig. 8 bottom left). Less frequently, events with paths near the plane of the detector array, with especially large deposited energy, or clustered in a shower, will affect multiple pixels directly. These events include 'snowballs[3]', which produce a core of pixels flagged with `OVERFLOW` and `TRANSIENT`, along with an extended halo of unflagged pixels (Fig. 8 bottom right). For R7, additional flags have been added (see Sec. 3.2.1) for these effects.

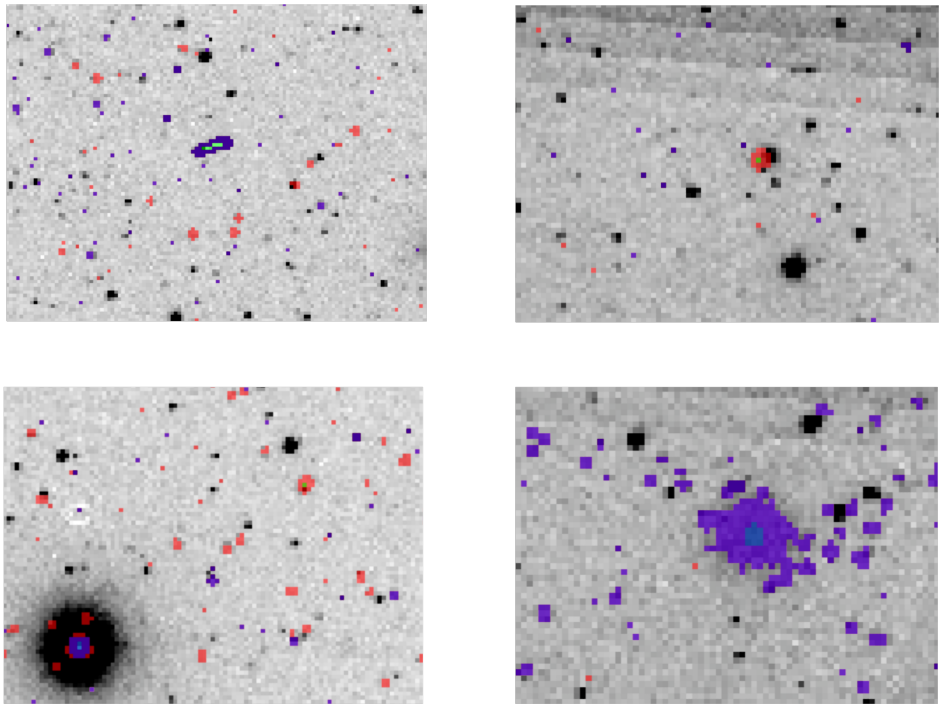

Figure 8: Examples of anomalous cosmic ray flagging. The gray scale is the spectral image flux, and the displayed flags are `TRANSIENT` (red), `OVERFLOW` (green), and `SUR_ERROR` (blue). Note that red and blue flags on the same pixel will appear as purple. Larger cosmic rays will have `OVERFLOW` flags in the center of the transient group. Snowballs have very large centers and are often accompanied by a number of nearby smaller transients. In all cases, pixels surrounding the transients show excess signal, possibly due to crosstalk or blooming. Top Left: Very early cosmic ray (center exhibits a transient prior to transient flagging and is flagged for `OVERFLOW` only), Top right: Late cosmic ray, Bottom left: Late cosmic rays with blooming source in bottom left of image, Bottom right: Early snowball.

- **Cosmic-ray-induced glow:** Cosmic rays also induce a faint, diffuse glow in the SPHEREx detectors, which is more visible when the Transient fraction is large. The glow is strongest in Bands 1 and 2 and produces a spectral gradient with more emission on the long-wavelength side. The glow response in Bands 4–6 is weak overall, with a brighter rim along the four edges of the detector array.
- **Crosstalk (Fig. 9):** In addition to the aforementioned crosstalk among neighboring detectors, occurring at the percent level, crosstalk also produces weaker artifacts at larger distances. These have been observed to take three forms in SPHEREx: 1) a negative image of a bright source displaced vertically by the readout row skipping spacing of ∼32 rows; 2) a smear resulting from a slowly decaying response to a bright source in the last read pixel of the prior row; 3) crosstalk among detector readout channels spaced by a multiple of 64 pixels horizontally. In R7, the first two of these crosstalk types are flagged in the image (see Sec. 3.2.9).

Features Defined as signatures from atmospheric or non-astrophysical objects.

[3] `https://jwst-docs.stsci.edu/known-issues-with-jwst-data/shower-and-snowball-artifacts#gsc.tab=0`

- **Atmospheric He Emission line (Fig. 10 upper row):** Bands 1 and 2 include emission from the atmospheric He line at 1.083 μm [Brammer et al., 2014], varying from a factor few to a factor of 30 greater surface brightness than the Zodiacal, or Zodi Light (ZL) background. The line amplitude varies over the orbit and with time, but astrophysical sources are visible behind the emission, and the variance layer of the LVF includes the impact of this emission line. The line is strong enough to produce weak but detectable spectral leak features in Band 1 (in pixels with bandpass center near 0.84 μm) and Band 2 (near 1.49 and 1.25 μm).
- **Auroral emission lines (Fig. 10 bottom row):** Near-infrared emission lines are a prominent feature of the aurora, appearing particularly in Bands 1 and 2, with occasional much fainter lines in Bands 3, 4, and 5. These lines are generated by excited atoms and molecules in the upper atmosphere, primarily nitrogen (N_2). The lines vary with solar activity, are more frequently seen when SPHEREx is above the polar regions, and are generally much fainter than the 1.08 μm He line. These spectral features can be a factor of a few brighter than the ZL background.
- **Other atmospheric lines:** Other emission lines from Earth's atmosphere with variable amplitude can be present at 0.78, 0.84, 0.93, 1.13, 1.81, 2.63, 2.75, 4.03, and 4.64 μm.
- **Shuttle glow (Fig. 11):** Shuttle glow is an emission that arises when spacecraft in low Earth orbit interact with the residual atmosphere, particularly atomic oxygen [Viereck et al., 1991]. As the spacecraft travels through this environment, high-speed atomic oxygen impacts surfaces in the ram

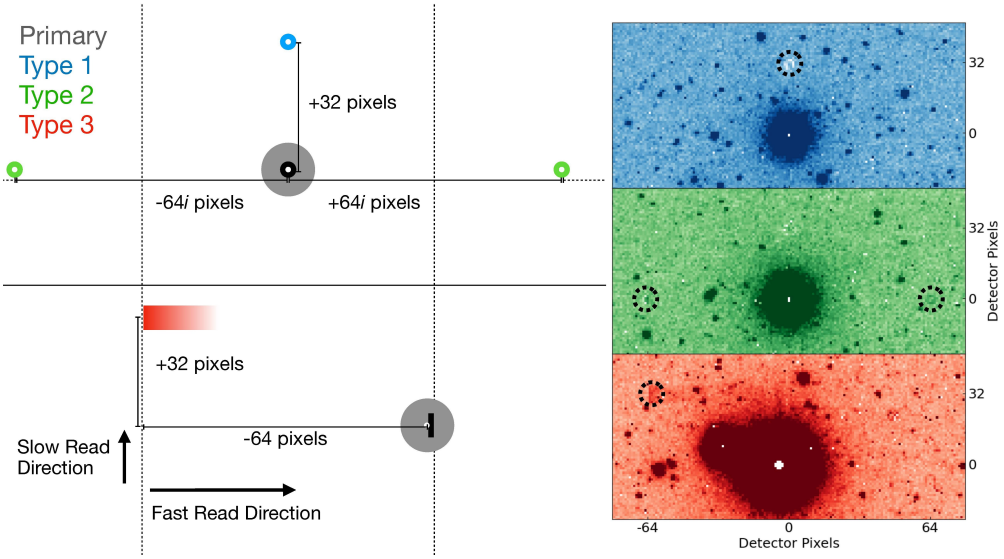

Figure 9: Overview of SPHEREx crosstalk. We observe three types of electrical crosstalk that are present when bright sources illuminate the detector array. Bright sources in this illustration are shown in "negative" form, where more flux is rendered in a darker tone. At the center of these bright regions are early overflow pixels with no determinable flux measurement, and so are assigned NaN and thus appear white. Pixels with unusually low or negative flux may also appear white on this scale. Electrical crosstalk Type 1 (blue) is an image of the large photocurrent pixels (dark circle) around a bright source (saturated pixels displayed in white at the center of the dark circle) displaced by 32 pixels in the slow read (row-to-row) direction, consistent with the NSKIP parameter of the row-chopping technique. Electrical crosstalk Type 2 (green) generates repeated sources at multiples of 64 pixels in both the positive and negative directions in the fast read (column-to-column) direction. This is thought to be due to true electrical crosstalk, as these pixels are read simultaneously. Electrical crosstalk Type 3 (red) is a smeared signal, but only occurs for bright (but not saturated) pixels at the edge of a channel. We suspect this may be due to some kind of hysteresis sensitive to large signal step functions in the Video 8 readout system. The right-hand panels show examples of each type of crosstalk color coded as in the schematic, with the incident stars being HD88230, HD87357, and HD233705. Dotted circles highlight the crosstalk images in each case. From Fazar et al. [2026]

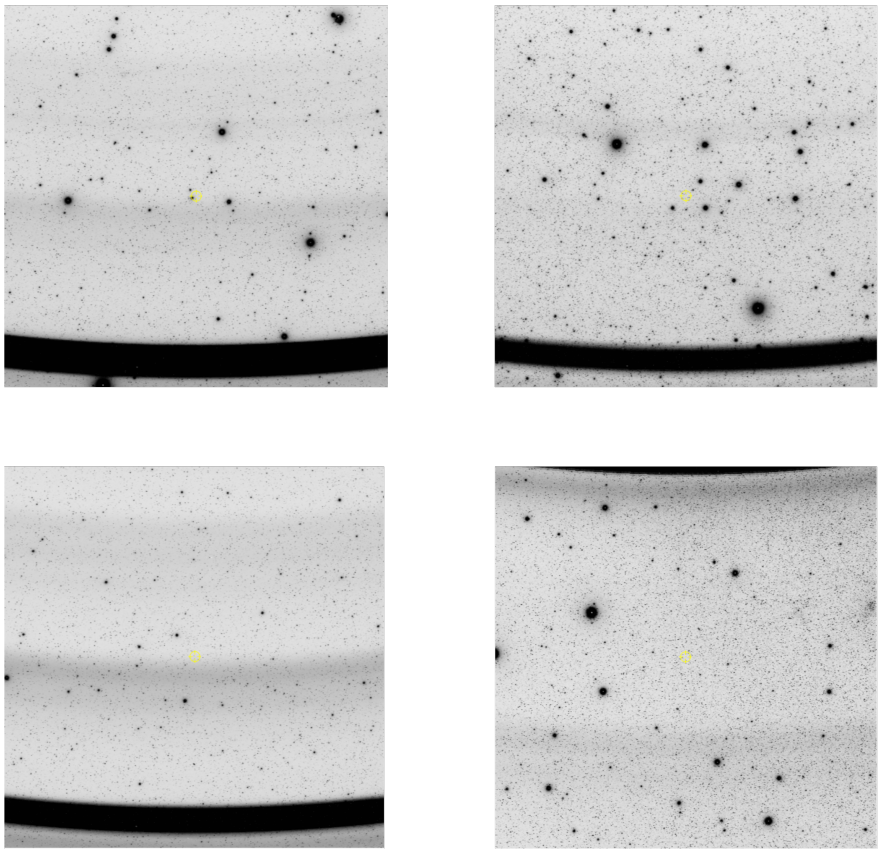

Figure 10: Features from atmospheric lines. Top and Bottom Left: Strong He lines in Band 1, Top right: Weak He lines in Band 1, Bottom left: He and auroral lines in Band 2.

direction, exciting surface materials and producing a faint glow, including in the near-infrared. To mitigate this effect, the SPHEREx survey plan limits the allowable ram angle during observations. In addition, a one-dimensional shuttle glow spectral template was constructed during commissioning calibration.

- **Diffuse Optical Transients (Fig. 12):** Roughly 1 % of exposures show diffuse and ephemeral features believed to be foreground objects or particles transiting quickly through or near the FoV.
- **Earth orbiting satellites (Fig. 13):** Streaks due to Earth-orbiting satellites can be seen in many images. The brightest examples can be several pixels wide and are flagged on board as transients and may also have SATELLITE_HALO (Sec. 3.2.1) flags. Fainter satellite streaks are flagged by the outlier module with the STREAK flag (Sec 3.2.10). Satellite streaks near the noise level may not be flagged.

2.4 Known Limitations

Incorrect source masking As described in Section 3.2.9, the spectral images include flags for pixels which have significant flux contributions from known sources. The size of the source mask is set by the magnitude from the Reference Catalog. If the estimated magnitude for the relevant pixel is incorrect, the mask will be too large or too small (Fig. 14).

Pixels at the dichroic edge (Fig. 14) The long-wavelength side of Band 3 and the short-wavelength side of Band 4 each have rows of pixels where the sensitivity and spectral responses are impacted by the DBS. Pixels where the throughput is below 50% have the `DICHROIC` flag set (see Table 16). While the gain calibration includes the decreased throughput, users should exercise caution when working with sources in

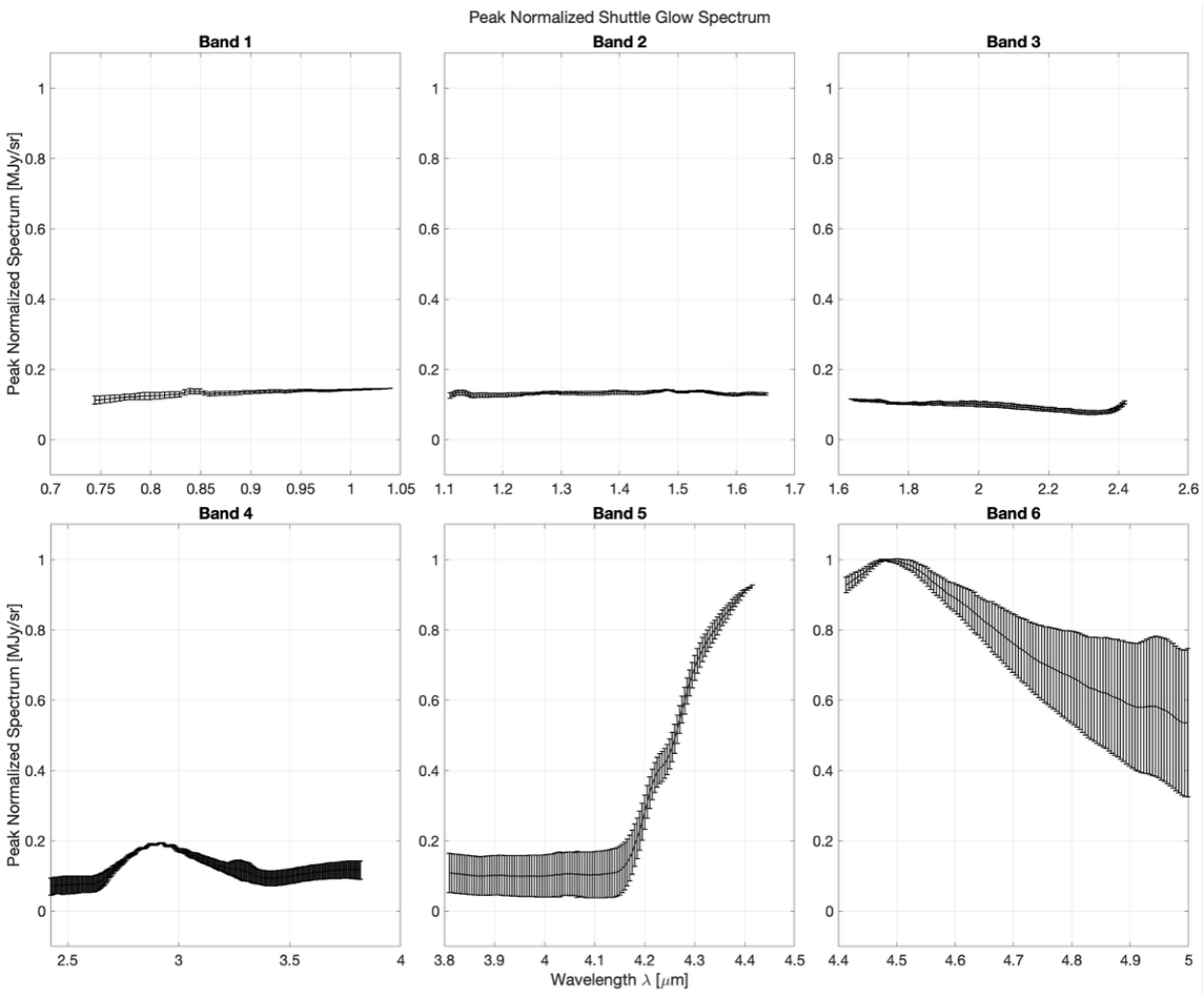

Figure 11: Shuttle glow emission spectrum. The template is flux-calibrated in MJy/sr across detectors and peak-normalized, showing that most of the contamination originates at ∼2.9 μm in Band 4 and at ∼4.5 μm in Bands 5 and 6.

these areas of the detectors, as the noise will be increased and the photometric calibration will be more uncertain.

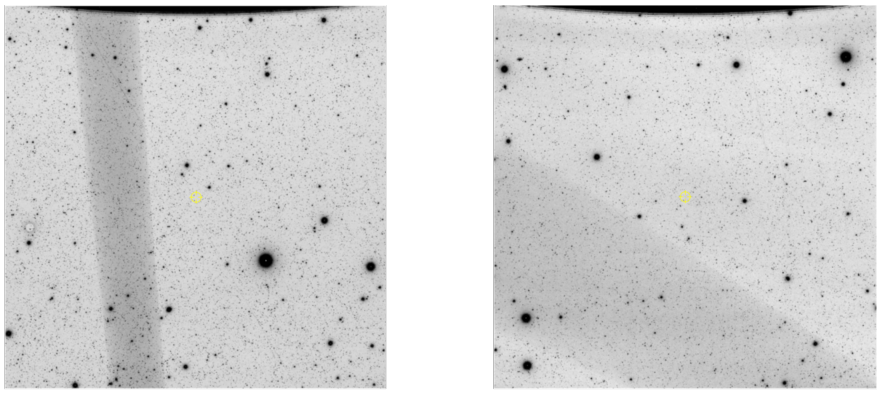

Figure 12: Examples of diffuse optical transients.

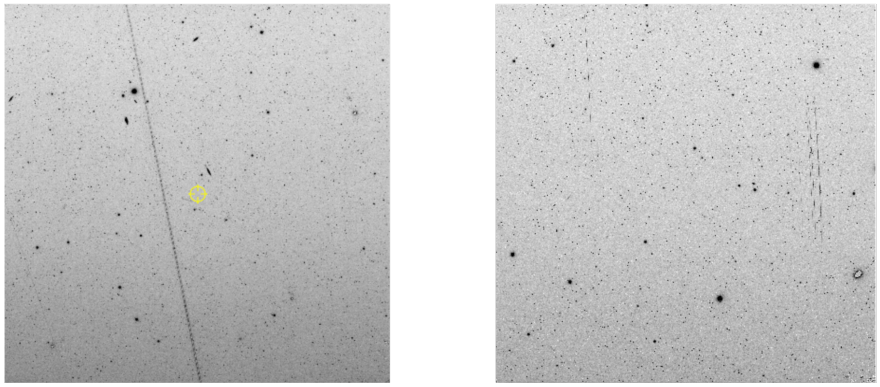

Figure 13: Examples of spectral images with satellite streaks.

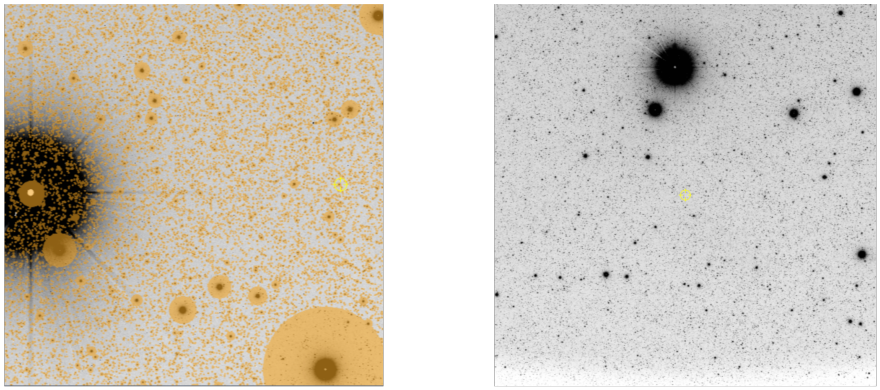

Figure 14: Left: example of a source mask which is too small, the source mask flag is shown in orange. Right: a Band 3 image showing the dichroic-impacted pixels at the bottom of the frame. Note that this example has been selected to emphasize the dichroic pixels and the current calibration provides better results.

3 The SPHEREx Data Processing

Data Processing Operation The SPHEREx data pipeline follows a tiered structure consisting of five distinct processing levels:

- **Level 0:** Raw telemetry processing, including on-board data handling, ingestion, decompression, and basic quality assessment.
- **Level 1:** Conversion of raw measurements into engineering units, such as photocurrent in electrons per second.
- **Level 2:** Photometrically and astrometrically calibrated spectral images and data cubes; calibrated spectral images form the QR data products.
- **Level 3:** Forced photometry performed at predefined reference positions, yielding catalogs
- **Level 4:** High-level science data products, including derived parameters such as galaxy redshifts, ice column densities, and deep image mosaics.

The pipeline described in this document includes Levels 1 to 3. The pipeline also derives the relevant calibrations. Section 4 describes the calibration products, the algorithms used to derive them, and the current performance. For SPHEREx, the traditional flat field and photometric gain products are combined into the Absolute Gain Matrix (Sect. 4.2.1) due to the wavelength variations across the band. Details on the pipeline infrastructure and interfaces are given in Akeson et al. [2026].

The SSDC is responsible for the development, implementation, and operation of processing pipelines from Level 1 through Level 3, in collaboration with the SST. Level 4 science products and advanced analysis algorithms are developed by the SST, tailored to the mission's three scientific pillars. All public data products will be distributed through IRSA, which hosts an interactive suite of tools for data searching, visualization, and retrieval.

The SPHEREx spectral images and associated calibration products released as part of the QR data set (Sect. 2) are processed by the SSDC. This section outlines the data processing procedures and algorithms, where applicable, that are applied to produce these QR products. Each subsection corresponds to the numbered pink boxes in Figure 5, which trace the data generation workflow.

The pipeline version is encoded in one of the header keywords in the spectral images (VERSION). Table 4 lists the pipeline versions used in quick release processing and a brief summary of the relevant changes between them.

3.1 Data Ingestion and Raw Image Processing

The tasks described in this section correspond to Level 0 and Level 1 of the SPHEREx data processing pipeline.

Onboard the observatory, the instrument's warm electronics compute pixel-level slopes from the detector readouts, compress and packetize the data, and transfer them to the spacecraft for temporary storage. The spacecraft then telemeters these science packets to the ground via Ka-band multiple times per day (typically ∼5). Upon receipt, the raw data are downlinked through the NASA NSN. At Caltech/IPAC, the SSDC ingests science data packets from Data Acquisition Processing & Handling Network Environment (DAPHNE) via Ka-band and engineering telemetry and navigation data from the Ground Data System (GDS) via S-band. These data streams are combined to generate Level 0 raw images. Each ingestion event includes the generation of a File Receipt Report, which is sent to GDS, and a push notification from DAPHNE confirming the availability of new data. At this stage, raw images and associated metadata are staged for processing by downstream pipelines.

After each downlink, the data packets are decompressed, and any missing pixel blocks are flagged. Coarse astrometry is determined based on the survey plan and geometric offsets. This initial pointing solution is accurate to $2' - 10'$ (and a rotation of a few degrees) and is to be refined later by the fine astrometry module (Section 3.2.8). To validate the SUR readout mode, an 8×34 pixel subsection of the detector is extracted and compared against the full SUR sequence to monitor noise performance and temporal stability. The raw pixel data are then converted from Analog Digital Units (ADU) to engineering units (electrons per second). For a small number of pixels, the Level 1 processing sets the pixel value to `NaN`. This is done if the on-board

Table 4: Processing pipeline versions used for quick release data

Version	Description
6.2.1	Initial version with calibrations derived from IOC and early science survey data
6.2.2	Changes to processing infrastructure, no changes for calibrated images
6.2.4	Updated PSF model in calibrated images
6.3.0	Updated proper motion application for astrometry and source masking
6.4.0	Version for qr-2 data; updates to PSF model, absolute gain, nonfunctional pixel map, spectral WCS and WAVE-WCS layer in image files, variance map and persistence parameters; inclusion of spacecraft location and velocity in spectral image header; updated SPHEREx Reference Catalog
6.5.3-6.5.5	Updates to qr-2 data including: significant updates to decrease the number of fine astrometry failures, new flagging for blooming, snowballs and cosmic ray halos, changes to persistence, beamsplitter ghost masking, and an updated nonfunctional pixel map. Applies to qr-2 data taken after 12/15/2025.
6.4+psffix1-6.5.5+psffix1	Files produced in previous versions of the pipeline with fixed PSF FITS layer header
6.5.6	Update to qr-2 to fix header description of PSF FITS layer ordering
7.0 - 7.2	Major pipeline update for Data Release 1, including significant updates to Persistence Masks, Bad Pixel Flagging, Fine Astrometry, Outliers Pixel Detection, Zodi Prediction, Photometric Measurements, and derivation of the Point Spread Function. Calibrations, including the absolute gain and spectral WCS have been updated.

error bit and either the early overflow or `SUR_ERROR` flags are set (see Table 15). Corrections are applied for amplifier chain drifts using reference pixels and interleaved phantom pixels. These corrections are flagged and recorded alongside the image data.

The resulting calibrated files are written in a standardized format and archived. As part of the Level 1 file creation, templates for three of the atmospheric emission lines described in Sec. 2.3 - Helium, aurora, and shuttle glow - are correlated with the image. The templates for each line are available as calibration products at IRSA (see descriptions in Sec. 4.3.3). The helium line fit properties and amplitude and the correlation coefficients for the aurora and shuttle glow are provided in the Level 2 file header. Note that emission from these lines is NOT subtracted from the calibrated images, although the Helium line emission is removed from images used to calculate the flat field. Before advancing to Level 2 processing, each Level 1 image file undergoes a series of automated quality checks. A subset of these validation results is communicated back to the Mission Operations System (MOS) for operational monitoring.

3.2 Processing Steps

Following Level 0 and Level 1 processing, Level 2 data processing is performed. At this stage, Level 1 images undergo astrometric and photometric calibration using a combination of ancillary catalogs and internally generated calibration products from the pipeline.

3.2.1 Source Blooming, Snowball and and Transient Halo Flagging

Source Blooming occurs when an astronomical source continues to photo-generate charge after the pixel has reached full well. This results in apparent spillover of the excess photo-generated charge into neighboring pixels which changes their charge collection rate (slope). In SPHEREx data, this can lead to early transient flagging if the source is bright enough to saturate the affected pixel within the first half of the exposure, a common occurrence in Bands 1, 2 and 3. Transient detection truncates the SUR algorithm and returns the slope corresponding only to frames prior to the transient. As the exposure progresses, neighboring pixels also fill, causing this phenomenon to bleed outward (or bloom, like a flower) from its source. This eventually terminates in a ring of late transients surrounding the early transient(s) as the effect continues into the second half of the exposure. Beyond the late transient ring, either the slope change is too gradual to be detected as a transient or the pixels in the first late transient ring do not reach saturation.

We have also observed a non-negligible number of Cosmic Rays of varying energies and Snowballs (very energetic cosmic rays and/or radioactive decay events), which also suddenly deposit charge within a pixel well, triggering transient flagging and resulting in excess photocurrent in proximity of these transient events, likely due to depositions of charge in neighboring pixels below the detection threshold or interpixel capacitance (IPC). Therefore, this processing step is designed to enlarge the size of each Cosmic Ray and Snowball event in the flag layer to avoid including this excess emission in science data.

In a similar way, transiting satellites that trip the transient flag will often include excess current measured in neighboring pixels due to charge depositions below the flagging threshold. Bright satellites that saturate pixels along their track will generate additional signal that extends beyond nearest neighbor pixels that appears as a satellite glow or halo. These pixels are flagged with a similar algorithm in this module to avoid including this excess emission in science data.

In addition, the central regions of Snowballs and large Cosmic Ray events produce excess persistence current, along with the blooming regions through the early transients surrounding sources (see Section 3.2.4). Typical smaller Cosmic Rays and satellite tracks, however, which also may trigger the early-transient flag, do not. Therefore, distinguishing among these phenomena is an important part of this algorithm.

Input and Output Description This step of processing requires access to the Level-1 flag layer, the slope-fit image and the following header keywords: DETECTOR (band) and TELAPSE (total duration of the integration ramp). The total number of electrons collected in the well of each pixel (i.e, the fluence) is computed by multiplying the slope-fit (in e^-/s) by the TELAPSE keyword value (in s). The following band-dependent fluence thresholds are used:

Table 5

Band	F_over
1 - 3	50000 e^-
4 - 6	30000 e^-

We also need the fraction of pixels that are transient-flagged, TRANS_FRAC, given by the header keyword N_TRANSIENT divided by the total number of active pixels (2040×2040).

The output of the algorithm is four new flags:

BLOOM: This indicates that the transient flags in the indicated pixels are most likely due to Source Blooming and not a direct optical or Cosmic Ray transient effect. The slopes of pixels with this flag may be useful for some science analyses but will likely suffer from excess persistence current in subsequent images.

SNOWBALL: This flag identifies the "Snowball" events seen in some infrared detectors (including the SPHEREx_H2RGs) in which very large quantities of electrons are released. These events are typically round and produce detectable photocurrent well beyond the source pixel(s). Since Snowballs and large Cosmic Rays triggering the OVERFLOW flag share flag layer characteristics, this algorithm flags both of these events as SNOWBALL but sets the HALO radius to represent the size of the event. SNOWBALL flagged pixels that are also flagged for OVERFLOW will likely suffer from excess persistence current in subsequent images.

HALO: This flag indicates a high probability that a pixel is significantly affected by a transient event in a neighboring pixel via, e.g., charge depositions below the flagging threshold or interpixel capacitance. The main purpose of this flag is to allow the 'halos' around Cosmic Rays and Snowballs to be discarded from science analyses.

SATELLITE_HALO: This flag indicates a high probability that a pixel is significantly affected by a satellite track in a neighboring pixel via, e.g., charge depositions below the flagging threshold or interpixel capacitance. The main purpose of this flag is to allow the 'halos' around satellite tracks to be discarded from

science analyses.

Description of Algorithm The algorithm consists of two steps. First, identifying Source Blooming, Snowballs and other transient events; and second, applying the extended halo (HALO) flag.

Step 1. Identifying Source Blooming and Snowball This step is based on the information associated with the flag combinations provided in Table 6. Only functional pixels (i.e., not flagged as NONFUNCT) in the 2040×2040 active pixel region are used.

Table 6

Label	TRANSIENT	OVERFLOW	SUR_ERROR
NON_FLAG	0	0	0
EARLY_TRANSIENT	1	0	1
LATE_TRANSIENT	1	0	0
ONLY_OVERFLOW	0	1	0
EARLY_OVERFLOW	0	1	1
LG_EARLY_TRANS	1	1	1
LG_LATE_TRANS	1	1	0

Because of the similarity in flagging combinations, Blooming sources are identified first followed by Snowball sources. In both instances, saturated CORE pixels in a contiguous region are identified first and their associated mantles are found by an outward search from the core according to the criteria laid out in Table 7, Table 8 and Table 9. Blooming sources have one or more types of CORE_BLOOM_PIXELS and one or more types of MANTLE_BLOOM_PIXELS along with a circular shape and a decreasing signal that is larger than the background as you search outward from the mantle. Snowball sources have CORE_SNOW_PIXELS and MANTLE_SNOW_PIXELS of the same type (see Table 9) and typically approach background levels outside of the transient-flagged region.

Table 7: CORE_BLOOM_PIXELS

Label	MINIMUM FLUENCE
ONLY_OVERFLOW	F_*over*
EARLY_OVERFLOW	N/A
LG_EARLY_TRANS	F_*over*

Table 8: MANTLE_BLOOM_PIXELS

Label	MINIMUM FLUENCE
ONLY_OVERFLOW	F_*over*
EARLY_TRANSIENT	0.2×F_*over*
LATE_TRANSIENT	0.1×F_*over*

Note that high transient fractions interfere with the algorithm. Therefore, for images with TRANS_FRAC > 0.1 additional restrictions apply, such as requiring circular shape, limiting fluence ranges and/or limiting the radius of the identified grouping. These limitations differ between Source Blooming and Snowball identification. The resulting flags in these high transient scenarios are used to determine the predicted persistence current in subsequent images. In rare cases where there are large-scale early transient regions and the recorded background signal is above the minimum signal threshold due to a transient foreground such as the fluctuation of aurora during an image, bloom detections may reach the limiting radius, currently set

to 25 pixels, and may also result in square bloom regions. In this case, the predicted persistence current of these early transient pixels flagged for bloom will be artificially inflated, leading to these pixels being flagged for persistence for longer than necessary in subsequent images.

Table 9

	CORE_SNOW_PIXELS		MANTLE_SNOW_PIXELS	
Type	Label	MINIMUM FLUENCE	Label	MINIMUM FLUENCE
1	LG_EARLY_TRANS	< F_*over*	EARLY_TRANSIENT	any
2	LG_LATE_TRANS	any	LATE_TRANSIENT	any
3	ONLY_OVERFLOW	< F_*over*	EARLY_TRANSIENT	any
4	EARLY_OVERFLOW	N/A	LATE_TRANSIENT	any

Step 2. Non-Overflow Bloom Flagging It has also been observed that there are cases where pixels illuminated by a source exhibit the TRANSIENT flag without also triggering the OVERFLOW flag. This may be due to sub-pixel pointing jitter, variable star signal or pre-saturation charge repulsion from the central pixel (also known as the brighter-fatter effect). In these cases, the flux recorded in the transient pixel is commensurate with a source. Thus, after the identification of Source Blooming and Snowballs, the algorithm searches the remaining pixels for groups of blooming transients without an OVERFLOW center, i.e., contiguous pixels containing both EARLY_TRANSIENT and LATE_TRANSIENT flags according to the criteria in Table 10, prioritizing the greatest fluence. As high transient images will encourage false positives, images identified as HIGH_TRANS are ignored, as are pixels flagged NONFUNCT and pixels already flagged BLOOM or SNOWBALL. The identification of Non-Overflow Source Blooming proceeds along the same lines as for Source Blooming and Snowballs.

Step 3. Transient Halo Flagging The HALO flag only applies to the 2040×2040 active pixel region and is set for pixels surrounding SNOWBALL collections as well as transients not identified as with either SNOWBALL or BLOOM. In particular, three distinct cases are considered for flagging:

- **Snowball Halo Flagging:** For each group of n_{SNOW} pixels identified as a Snowball or high-energy Cosmic Ray, the centroid of these pixels containing the OVERFLOW flag is determined. From the pixel centroid, the region where the halo excess current exceeds 0.1 e/s extends out in a circle with a radius approximately equal to:

$$r_{HALO} = \sqrt{2 \times n_{SNOW}} \tag{1}$$

  All pixels within this radius are flagged with HALO.

- **Saturating Satellite Halo Flagging:** If the pixel distance between the centroid and the furthest pixel in the collection exceeds that of r_{HALO} determined by Snowball halo flagging, this is most likely a saturating satellite streak and not a Snowball. In this case, we apply a halo flag that mimics the Snowball halo, but with an extended shape. To do this we determine the skeleton of the track following the overflow pixels, obtain a distance map from the skeleton to the nearest edges of the

Table 10: Non-Overflow Bloom Pixel Candidates

Type	Label	MINIMUM FLUENCE
1	EARLY_TRANSIENT	0.5 F_*over*
2	EARLY_TRANSIENT	0.1 F_*over*
3	LATE_TRANSIENT	0.1 F_*over*

saturating satellite track as a function of the position (s) along the skeleton, r_{edge}, and apply a halo that is proportional to the cross-skeleton distance. These pixels are set to the SATELLITE_HALO flag.

- **Remaining Transient Flagging:** For each pixel in the 2040×2040 active pixel region with non-zero TRANSIENT flag that is not already identified as BLOOM or SNOWBALL, the 4 immediate edge-adjacent neighbors are set to the HALO flag.

3.2.2 Nonlinearity Correction

This processing unit corrects for detector Non-Linearity (NL), which arises from declining gain as charge accumulates within each H2RG pixel (e.g., Zengilowski et al. 2020). As a prerequisite to correction, observed (uncorrected) photocurrent measurements are converted into (uncorrected) electron counts by incorporating the pixel-specific integration time. This transformation enables precise application of the NL correction. The corresponding inputs and outputs of this processing step are summarized in Table 11.

Table 11: Inputs and Outputs of the NL Correction Module

Input	Output
Uncorrected photocurrent images, NL correction parameters, Charge thresholds for algorithm applicability, SUR parameter settings	NL-corrected photocurrent images, Binary flag

Input and Output Description The NL correction module is applied exclusively to the 2,040 × 2,040 pixel photo-sensitive region of each detector, excluding both phantom pixels and reference rows (see Sect. 3.1). The input NL calibration parameters are derived from ground-based testing in which the detector array is illuminated with diffuse, constant intensity and the signal is recorded for each frame of an exposure.

The output files retain the same FITS image format, units, and size as the input, except that the detector signals have been linearized. For instance, signal levels near the upper end of the dynamic range are boosted to approximate the response of an ideal linear detector.

Description of Algorithm The SUR parameters are set on board such that slope fits use only samples below the Overflow threshold, which is set at approximately half of the full-well capacity of the detectors. In this range, the nonlinearity is described to sufficient accuracy using a quadratic:

$$Q_{\rm observed} = Q_{\rm collected}(1 - Q_{\rm collected}/Q_{\rm nl}), \tag{2}$$

where $Q_{\rm collected}$ is the true charge deposited in the pixel, $Q_{\rm observed}$ is the observed signal in the pixel (in the same units and using the calibration applicable at low charge), and $Q_{\rm nl}$ is the nonlinearity parameter. The on-board electronics measures slope fits to $Q_{\rm observed}$ vs. sample index during the exposure, and it is the task of the nonlinearity module to estimate $Q_{\rm collected}$ and therefore the correction factor $(1 - Q_{\rm collected}/Q_{\rm nl})^{-1}$. Typical values for $Q_{\rm nl}$ are 1.4E6 e^- for Bands 1–3 and 0.8E6 e^- for Bands 4–6. The correction factor is 1.05–1.08 for full-length exposures that reach the Overflow threshold at the end.

Assuming the model in Equation 2, combined with some SUR parameters and some algebra, the corrected photocurrent for each pixel is found to be:

$$F = \frac{Q_{\rm nl}\left[1 - \sqrt{1 - 4T_{\rm fr}(N + {\rm SURDLY})F'/Q_{\rm nl}}\right]}{2T_{\rm fr}(N + {\rm SURDLY})}, \tag{3}$$

where F' is the observed photocurrent, $T_{\rm fr} \approx 1.53$ seconds is the frame duration, SURDLY = 3 is the index of the first frame used in the slope fit, and N is the index of the last frame used in the slope fit. For

uninterrupted SURs, $N = \mathrm{SURLIM} = 77$. For an Overflow-interrupted SUR, N is derived through iterated solution of Equation 3 and:

$$N = \mathrm{minimum}\left(\mathrm{SURLIM},\ \texttt{floor}\left[\frac{Q_{\mathrm{nl}}(1-\sqrt{1-4Q_{over}/Q_{nl}})}{2T_{fr}F}\right]\right), \tag{4}$$

where Q_{over} is the Overflow threshold in charge units. If the `SUR_ERROR` flag is set (see Sect. 3.2.4 and Table 9), then no correction is applied, i.e., $F = F'$. If the `TRANSIENT` flag is set (see Sect. 3.2.4 and Table 9), then an estimate is made for the value of N since it is not known exactly.

For pixels with low confidence in the nonlinearity correction due to poor intrinsic linearity or inadequate calibration data, the `NONLINEAR` flag is set by this module (see Sect. 3.2.4 and Table 9).

3.2.3 Variance Map

This processing unit generates per-pixel variance maps for each detector array, producing an estimate of the variance based on the downlinked ramp or flux images processed on board. The method is based on the derivations present in Robberto [2007], which describe the statistical foundations for variance estimation under various non-destructive readout schemes used in infrared detectors. Variance estimates are derived from the raw image data and updated at each step in SSDC Level 2 pipelines where the flux image is processed, ensuring the propagated variance remains accurate. The corresponding inputs and outputs of this processing step are summarized in Table 12.

Table 12: Inputs and Outputs of the Variance Map Module

Input	**Output**
Level 1 detector images, Per-pixel electronic noise map	Variance map, Binary flag

Input and Output Description The inputs to this module include the Level 1 FITS image (2,072 × 2,176), which contains both phantom pixels and repeated samplings of the reference rows, expressed in engineering units (in e^-/s). Additional inputs include a per-pixel electronic noise map for each array, with dimensions of 2,048 × 2,048 pixels (in e^-), and an accompanying flag map. Reference pixels are retained in the variance calculation to support trending and analysis. The electronic noise model accounts for both Correlated Double Sampling (CDS) noise and excess readout noise, characterized through pre-flight laboratory measurements. However, shot noise due to dark current is excluded from this estimate, as it is incorporated separately from the image itself – dark current is not subtracted at this processing stage.

The output consists of a variance map with the same dimensions (2,072 × 2,176, in $(e^-/s)^2$), representing the maximum likelihood estimate of combined Poisson and electronic noise per pixel. Variance values for phantom pixels may be set to `NaN`, while those for reference pixels (including repeated samplings) are directly sourced from the 2,048 × 2,048 electronic noise map. A corresponding flag is also generated to indicate uncertainty in the variance estimate, triggered in cases of overflow or when transient events disrupt integration.

Note: While the variance module initially produces a variance layer with dimensions of 2,072 × 2,176 in units of $(e^-/s)^2$, subsequent calibration to physical units reduces the array size to 2,040 × 2,040 and converts the units to $(\mathrm{MJy/sr})^2$. This final calibrated version is the only variance product exposed to users and is delivered as the `VARIANCE` layer of the spectral image (Sect. 2.2).

Description of Algorithm The underlying mathematics of this module follows the framework detailed in Robberto [2007]. For SPHEREx, the detector readout scheme involves uniformly sampling the accumulating signal, consistent with the method described in Section 2.2 of that reference. Accounting for both readout and Poisson noise contributions, the maximum likelihood estimator for the total signal variance is derived

by combining Equations 1.39 (readout noise) and 1.49 (Poisson noise) in Robberto [2007]:

$$\texttt{Var} = \left[\sigma_{\rm CDS}^2 \frac{6(N-1)}{N(N+1)} + \frac{6}{5}\frac{N^2+1}{N^2-1} F \cdot T_{\rm int}(N)\right] \ , \tag{5}$$

where $\sigma_{\rm CDS}$ is the CDS readout noise for a given pixel, N is the number of reads, F is the measured slope of the accumulating signal, and $T_{\rm int}(N)$ is the integration time for N reads. This expression estimates the variance of the total integrated signal. To compute the variance of the measured slope, the result is divided by $T_{\rm int}(N)^2$.

However, laboratory testing revealed an additional excess readout noise component that effectively increases the CDS noise. Since pre-flight testing directly measures per-pixel electronic noise, these values are used in place of modeled noise estimates. Incorporating this lab-based variance, Equation 5 becomes:

$$\texttt{Var} = \left[\sigma_{\rm det}^2(ij, N) + \frac{6}{5}\frac{N^2+1}{N^2-1} F \cdot T_{\rm int}(N)\right] \ , \tag{6}$$

where $\sigma_{\rm det}^2(ij, N)$ represents measured per-pixel electronic noise variance for detector pixel (i, j) and for a total of N reads.

There are two specific cases in which the commanded number of reads can differ from the actual number used in slope estimation:

- **Overflow:** For bright sources that saturate a pixel mid-ramp, the effective number of reads N is inferred from the measured flux and the overflow threshold at which sampling ceased. In such cases, the estimated N is substituted into the Poisson term on the right-hand side of Equation 6 to evaluate variance. Given the dominance of photon noise in this regime, the electronic noise term can be neglected.
- **Transient interruption (e.g., cosmic ray hit):** If the integration is disrupted by a transient event, the actual number of usable reads is unknown. In this scenario, the module defaults to using the per-pixel electronic variance for the minimum possible number of reads to yield a conservative estimate of total variance.

If a pixel is flagged as both `OVERFLOW` and `TRANSIENT`, the variance is estimated using the overflow prescription above (photon noise will dominate electronic noise).

3.2.4 Persistence Masks

This processing unit applies a parameterized analytic model to estimate the level of persistent flux in each pixel based on the cumulative exposure history of the survey. Image persistence is a well-documented artifact in H2RG detectors, characterized by a slowly decaying residual signal from previous exposures – typically arising where bright sources previously illuminated the array. This residual flux can contaminate subsequent science images. According to the prevailing model described by Smith et al. [2008], image persistence originates from charge traps within the detector diode depletion region. These traps accumulate charge during standard photodiode operation and release it gradually following a detector reset. Based on the persistence estimates, downstream modules generate masks to flag and exclude pixels likely to be affected, thereby mitigating contamination in the science data. The corresponding inputs and outputs of this processing step are summarized in Table 13.

Input and Output Description The input to this module consists of 2,040 × 2,040 slope-fit images from SUR (in e^-/s) for each of the six detectors, along with associated Level-1 binary flag maps that include SUR transient, overflow, and pixel error indicators (corresponding to the `TRANSIENT`, `OVERFLOW` and `SUR_ERROR` flags, see Sect. 3.2.5 and Table 16). Additional flag inputs include `BLOOM` and `SNOWBALL` flags to distinguish between persistence behaviors of pixels associated with source blooming and snowballs or high energy cosmic ray impacts, see Sect. 3.2.1. This module also requires the elapsed time between the end of the previous exposure and the start of the current one, as well as exposure time and the coefficients of the persistence current model from prior exposures. This information is then used to derive persistence-state model coefficients for the current observation.

Table 13: Inputs and Outputs of the Persistence Mask Module

Input	**Output**
Slope-fit images from SUR, SUR, SNOWBALL and BLOOM flags from level 1 data, Elapsed time between consecutive exposures, Elapsed time of each exposure (`TELAPSE`), Persistence model parameters from previous exposure (s)	Binary array of Persistence flags

The output comprises a series of FITS files containing 2,040 × 2,040 arrays with the predicted persistence image for each detector and the resulting mask image for the current exposure. Pixels in the persistence image exceeding the predefined threshold are flagged as contaminated and recorded in the mask to be excluded from downstream analysis.

Description of Algorithm The persistence current $I_p(t)$, in units of e^-/s, is modeled as a sum of exponentially decaying terms:

$$I_p(t) = \sum_{n=1}^{N} A_n \; C_n e^{-t/\tau_n}, \tag{7}$$

where A_n is an exposure-dependent coefficient based on the value of the coefficient from previous exposures, the elapsed time t since the end of the most recent exposure and the prior exposure's fluence F, given by

$$F = f \times t_{int}, \tag{8}$$

where f is the exposure's slope-fit and t_{int} is the exposure's elapsed time from start to stop, `TELAPSE`. The coefficients C_n are unitless scaling factors, and τ_n is the decay constant for term n in seconds. The coefficients C_n are selected such that the summation, when $A_n = 1$, approximates the form $1/(t+1)$, with $t = 0$ defined at the detector reset following an illuminating exposure. Each array is assigned fixed values for C_n and τ_n, typically spanning 6 to 8 terms.

For exposure m, the coefficient A_{n_m} accounts for persistence from the previous exposures by exponentially decaying their contribution over the time elapsed since that exposure to the end of the most recent exposure. This is recursively encompassed in the second term of Equation 9:

$$A_{n_m} = B_n(f_{m-1}, t_{\rm int}) + B'_n(f_{m-2}, t_{\rm int})\, e^{-(t_{{\rm slew}_{2\to1}} + t_{\rm int})/\tau_n}, \tag{9}$$

where B_n and B'_n are retrieved from a lookup table based on the slope fit from exposures $m-1$ and $m-2$, respectively and $t_{{\rm slew}_{2\to1}}$ is the time between the end of exposure $m-2$ and the beginning of $m-1$ in seconds. This formulation assumes persistence is additive. If the the elapsed times differ between exposures, the notation generalizes as $t_{\rm int} \to t_{{\rm int}_{m-1}}$ and $t_{{\rm int}_{m-2}}$ in the first and second coefficients respectively, and the average elapsed time replaces $t_{\rm int}$ in the exponential term.

In the absence of previous exposures, both B_n and B'_n are zero, yielding $A_{n_m} = 0$. When only a single prior exposure exists, $B'_n(f_{m-2}) = 0$. For subsequent exposures ($L = m+1$), the contribution from exposure m is preserved as:

$$B'_n(f_{L-2}, t_{\rm int}) = A_{n_m}. \tag{10}$$

The persistence current predicted for exposure m is evaluated at the temporal midpoint of exposure m:

$$I_p(t_m) = \sum_{n=1}^{N} A_{n_m}\, C_n e^{-t_m/\tau_n}, \tag{11}$$

where A_{n_m} is from Equation 9, and

$$t_m = t_{{\rm slew}_{1\to0}} + \tfrac{1}{2} t_{\rm int}, \tag{12}$$

with $t_{{\rm slew}_{1\to0}}$ denoting the time between the end of exposure $m-1$ and the start of exposure m.

The look-up tables producing B_n and B'_n show four regions: zero, linear, approaching saturation and saturation. These result in a piecewise function generically described in Equation 13, where F represents fluence, r represents a band-dependent rate that also depends upon the flag conditions of the previous exposure, F_1, the fluence at which the rate changes to r_1, and $F = F_{sat}$, the band-dependent value at which the persistence current saturates at band-dependent I_{sat}.

$$B_n = \begin{cases} 0 & F < 0 \\ r \times F & 0 \leq F \leq F_1 \\ r_1 \times F + F_1(r–r_1) & F_1 \leq F \leq F_{sat} \\ I_{sat} & F > F_{sat} \end{cases} \tag{13}$$

There are several instances represented by the flag layer of each image in which the fluence is improperly determined by the multiplication of the flux and the elapsed time from start to stop of the exposure. The flag layer is used to identify these cases and properly assign persistence current according to our interpretation of the specific flag combinations (see Table 14). To this end, important effects that have to be accounted for are Source Blooming and Snowball (see Sect. 3.2.1).

Table 14: Flag Conditions Affecting Predicted Persistence

OVERFLOW	SUR_ERROR	TRANSIENT	SRC_BLOOM	SNOWBALL	**Interpretation**	**Overwrite F with F_{sat}**
1	1	0	0 or 1	0 or 1	Early Overflow	YES
1	1	1	1	0	Early Bloom	YES
1	1	1	0	1	Early CR[4] Center	YES
1	0	1	0	1	Late CR Center	YES
1	0	0	1	0	Source Overflow	NO
1	0	0	0	1	Very Early CR center	YES
0	1	1	1	0	Source Blooming	NO

This module generates several diagnostic quantities to evaluate temporal trends in residual persistence. These include the total number of pixels flagged for persistence in each exposure frame; the cross-correlation between the current image and the previous exposure, computed both with and without application of the persistence mask; and the auto-correlation of the current exposure to assess residual artifacts originating from bright sources observed prior to the start of the integration.

3.2.5 Bad Pixel Flagging

This processing unit generates a pixel-level map for each detector array, identifying pixels that should be excluded from downstream photometric measurements. For each exposure, the module produces a lookup table flagging the small subset of instrument-frame pixels deemed unsuitable for use beyond Level 1 processing. Rather than employing a simple binary mask, the system encodes the reason for exclusion in a coded map. While this approach entails a modest increase in data volume, the added diagnostic detail enhances the utility of the product for future performance analysis and troubleshooting throughout the mission. The corresponding inputs and outputs of this processing step are summarized in Table 15.

Table 15: Inputs and Outputs of the Bad Pixel Correction Module

Input	**Output**
Level 1 detector images, Flag maps generated by onboard SUR processing, Persistent images from prior exposures, Map of permanently inoperative pixels	Bad pixel mask images

Input and Output Description The input to this module includes Level 1 photocurrent FITS images, each with dimensions of 2,040 × 2,040 pixels in units of e^-/s, and corresponding flag maps in FITS format generated by the onboard SUR system for each of the six detectors. These flag maps are telemetered along with the science data and share the same dimensionality as the science images. Additional inputs include a 2,040 × 2,040 FITS map of permanently non-functional pixels for each of the six flight arrays, based on pre-flight laboratory characterization, as well as flags set by the Correct Nonlinearity (Sect. 3.2.2), Update Persistence Mask (Sect. 3.2.4), Create Source Mask (Sect. 3.2.9) and Outlier Pixel Detection (Sect. 3.2.10) Level 2 modules.

The output comprises a per-exposure, per-detector bad pixel mask, delivered as a 2,040 × 2,040 FITS image in which each pixel is annotated with a symbolic flag indicating its classification. Each flag corresponds to a specific bit position, with standardized symbolic identifiers assigned to defined conditions. The full set of flag names is recorded in the header of the associated spectral image output file (see, e.g, Table A.35 in Sect. 2.2).

Image Pixel Flag Definitions Pixel flags are generated across multiple modules within the image-processing pipeline. For each spectral image released as part of the QR dataset, these flags are preserved and publicly distributed through IRSA. IRSA's visualization interface supports the display of these flags as overlay layers, enabling users to assess pixel-level data quality interactively. Table 16 summarizes the flag names, their corresponding bit values, and associated descriptions.

Table 16: Image pixel flags used in spectral images at Level 2

Symbolic name	Bit #	Description	Note
`TRANSIENT`	0	Transient (such as cosmic ray hit) detected during SUR. *Note:* Transients occurring during the first ten seconds of the observation may not be flagged. This flag can also indicate pixels affected by charge spillover (bloom) from very bright neighboring sources. When saturation from a bright star causes charge to spill into adjacent pixels, the onset of such spillover can trigger `TRANSIENT` flagging by the onboard SUR algorithm.	Determined onboard (Level 0)
`OVERFLOW`	1	Overflow threshold reached during SUR. This threshold is set at approximately half the level of full-well saturation.	
`SUR_ERROR`	2	`chksum_error` bit from instrument data processing. In the absence of other flags, it indicates a data handling error in the SUR algorithm onboard. When combined with the `TRANSIENT` or `OVERFLOW` flags, signals early transient (first half of exposure) or early overflow (first ∼5 seconds) conditions.	
`NONFUNC`	6	Static, initially pre-flight assessment that a pixel is permanently unusable/dead. May be updated from time to time during the mission. This is unusable for any purpose.	Static

continued . . .

. . . continued

Symbolic name	Bit #	Description	Note
DICHROIC	7	Pixels in the "dark corners" of Bands 3 and 4, where the "smile" effect results in pixels with a bandpass incompatible with which side of the dichroic they are on. This flag indicates pixels with low expected throughput that are not usefully calibrateable or of value for photometry.	
MISSING_DATA	9	Pixels for which the onboard data was lost before ingest by the SSDC, e.g., as corrupted packages on the downlink that were not retransmitted successfully, resulting that there is no data available for this pixel in this image.	Set by the Level 1 pipeline based on per-image data content and quality assessment.
HOT	10	Hot pixel – noisy or otherwise affected by spurious signal. Determined per-exposure; permanently hot pixels are flagged as NONFUNC. Not usable for science.	
COLD	11	Pixel that appear unresponsive to light or otherwise has an anomalously low signal in a particular exposure; permanently dead pixels are flagged as NONFUNC. Not usable for science.	
FULLSAMPLE	12	Pixel for which the full sample history is available, because of the rotating 8×32 pixel region for full readout. Not usable for science, purely informational.	
PHANMISS	14	Applied for pixels that can not be corrected due to missing phantom pixels.	
NONLINEAR	15	Pixel for which a reliable nonlinearity correction could not be determined. Due to poor photometric accuracy, this pixel should be excluded from most scientific analyses.	Set by the Level 2 pipeline based on per-image data content and quality assessment.
PERSIST	17	Pixel found to have been affected by persistent charge above the Level 2 threshold for this.	
OUTLIER	19	Pixel flagged by "Detect Outlier Pixels" module (Sect. 3.2.10).	
CROSSTALK	20	Pixel found to have been affected by "ordinary" crosstalk (Sect. 3.2.9).	
SOURCE	21	Pixel mapped to a known source.	
GHOST	22	Pixel found to have been affected by an optical ghost from a bright source inside the exposure frame (Sect. 3.2.9).	
GHOST_FPA	23	Pixel found to have been affected by an optical ghost from a bright source seen on another detector in the FPA. This flag is currently unused (subsumed into GHOST_EXT) and will be removed in Year 2 processing.	
GHOST_EXT	24	Pixel found to have been affected by an optical ghost from a bright source outside the field of view. Currently in development.	
STREAK	25	Pixel found to have been affected by a streak detected in the image, presumably from an object in Earth orbit (Sect.3.2.10).	

continued . . .

. . . continued

Symbolic name	Bit #	Description	Note
BLOOM	26	Pixel found to have been affected by source blooming (Sect. 3.2.1).	
SNOWBALL	27	Pixel found to have been affected by snowball events in which very large quantities of electrons are released (Sect. 3.2.1).	
HALO	28	Pixel found to have been affected by the halo of a transient. Caution is recommended when using this pixel in science analysis (Sect. 3.2.1).	
SATELLITE_HALO	29	Pixel found to have been affected by the halo of a satellite streak. This pixel is not recommended for use in science analysis (Sect. 3.2.1).	

3.2.6 Dark Subtraction

Dark current (with units of e^-/s) is estimated simultaneously with the flat-field response derivation, as described in 4.2.1. This additive component is first subtracted from the 2,040 × 2,040 active pixel region of the Level 1 image prior to applying the absolute gain matrix that converts to physical units.

3.2.7 Absolute Gain Correction

This processing step multiplies the dark current-subtracted 2,040 × 2,040 Level 1 image by the absolute gain matrix, described in more detail in 4.1.1. The absolute gain matrix is a 2,040 × 2,040 array with units (MJy/sr) / (e^-/s). It encodes pixel-to-pixel response variations within spectral channels as well as the absolute gain conversion for each spectral channel, such that multiplying it by the dark-subtracted Level 1 image brings the image to the physical unit of MJy/sr.

3.2.8 Astrometry

This processing unit refines the astrometric solution by determining the optimal translation, rotation, and updated distortion map required to align detected stars in each of the six exposures with their counterparts in the Reference Catalog. This correction ensures photometric accuracy at the sub-arcsecond level and supersedes the coarse astrometry computed during Level 1 pipeline processing. The corresponding inputs and outputs of this processing step are summarized in Table 17.

Table 17: Inputs and Outputs of the Fine Astrometry Module

Input	Output
Spectral images, First instrument distortion map then average empirical distortion map, Proper-motion-corrected Gaia reference catalog with predicted SPHEREx fluxes	WCS solution coefficients, Refined higher-order Simple Imaging Polynomial (SIP) polynomials, Fine Astrometry flag (FINAST)

Input and Output Description The input to this module includes spectral FITS images from all six detectors, each consisting of a 2,040 × 2,040 pixel array. These images contain initial coarse astrometric solutions encoded as WCS coefficients in their headers, as described in Section 3.1, accurate to a few arcminutes. The Gaia DR3 catalog [Vallenari et al., 2023] serves as the astrometric reference. To predict the SPHEREx fluxes of the Gaia stars, they are matched to Wide-field Infrared Survey Explorer (WISE) and Two Micron All Sky Survey (2MASS) photometry. The reference catalog is pre-processed to flag high-confidence astrometric calibration stars, *i.e.* stars which are non-saturated, high S/N, and spatially isolated

in SPHEREx bands. Proper motions provided by Gaia are used to propagate stellar positions to the current observation epoch; sources with poorly constrained proper motions are excluded. In addition, this module requires a prior distortion map (*i.e.* SIP coefficients). For the first run of this module, an instrument distortion map derived from ground testing is used. For pipeline versions R7 and later, the prior distortion map is generated from the mean of hundreds of empirical distortion maps derived by this module.

The output includes refined WCS coefficients and updated SIP distortion terms for each detector, which are written to the headers of the corresponding spectral image files (see Table A.35). In addition, an astrometry flag (`FINAST`) is added to the header, indicating a good (0) or poor (>0) astrometric solution.

Description of Algorithm Since pipeline version R7, this module is split into the *main astrometry module* as well as the *astrometry retry module*. The latter is used to remedy some astrometric failures left by the main module. Both modules are described below.

The algorithms employed by the *main astrometry module* are based on the `AstroPy`[5] Python library, the `Astrometry.net`[6] suite, the `scamp` software [Bertin, 2006], and the WISE astrometry pipeline[7]. The astrometric calibrators are selected to have *(i)* good Gaia astrometric solution [$astrometric_params_solved \geq 31$ in the Gaia catalog; Vallenari et al., 2023]; *(ii)* S/N > 10 but not saturated in bands Gaia RP, izy, JHK_s, and WISE $W1/W2$; and *(iii)* no sources within 2 SPHEREx pixels that are brighter than 10 % of the flux of the calibrator. Figure 15 illustrates the overall structure of the Fine Astrometry algorithm.

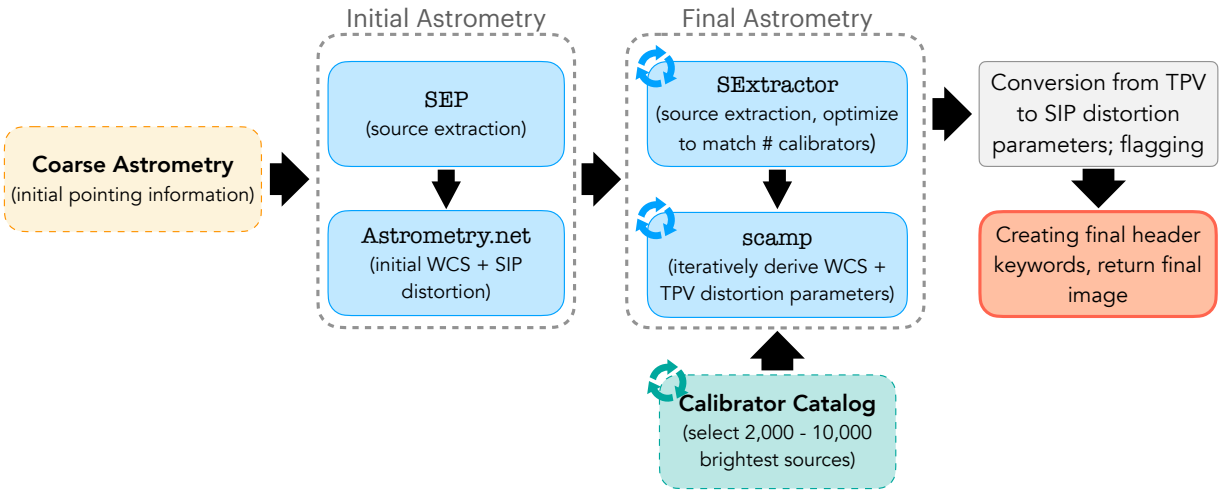

Figure 15: Schematic of the Fine Astrometry algorithm.

The following summarizes the step-by-step implementation of the module:

1. The module initializes with a linear WCS solution (origin, translation, rotation) obtained from the Level 1 coarse astrometry estimation as well as an initial distortion (SIP coefficients). The former first-guess solution is derived from the planned pointing as described in Section 3.1 and is accurate to a few arc-minutes. The latter is obtained from the median of measured distortion maps by this module (pipeline versions ≥ 6.5) instead of from ground testing (pipeline versions (6.5).
2. Using these initial pointing coordinates, the `solve-field` module from the `Astrometry.net` suite is run to derive an initial WCS solution including SIP distortion parameters. For the latter, we assume a 3rd order polynomial parameterization with a zero point `CRPIX` = (1020.5, 1020.5) (center of the spectral image). The `solve-field` module is run on point sources extracted from the spectral image using the `sep`[8] package with a detection threshold of 100σ. For the matching process, the `solve-field`

[5] `https://www.astropy.org/`
[6] `https://www.astrometry.net`
[7] `http://wise2.ipac.caltech.edu/docs/doc_tree/sds/sds-PRex.pdf`
[8] `https://sep.readthedocs.io/en/stable/`

module uses the 4,100 and 5,200 index files[9], which are based on Gaia DR3 and 2MASS stars. This second refined solution is accurate to a few arc-seconds.

3. In the next step, the astrometric calibrators (see above) are extracted over the extent of the spectral image. From this calibrator selection, the N brightest (below saturation limit) calibrators were selected and used to adjust the faint magnitude limit iteratively such that N is between 2,000 and 10,000. This adjustment is crucial to obtain a similar density of sources in crowded (e.g., galactic plane) vs. less crowded (e.g., extragalactic) fields.
4. Next, `SExtractor` is used to extract sources on the spectral image (with astrometric solution from above applied), which serve as reference sources on the SPHEREx images. At first, a pre-defined detection threshold depending on the galactic latitude is used. This threshold is then refined by running `SExtractor` iteratively until the number of extracted sources is within 20% of the number of calibrators from the reference catalog. This accounts for different source densities at different positions on the sky and ensures the best possible matching between calibrators and extracted sources.
5. Finally, the calibrator catalog and `SExtractor` catalog (both in *LDAC* format) are fed to `scamp`, which is used to derive the final WCS and distortion solution for a given detector image. To this end, `scamp` is run iteratively (re-extracting the sources by running `SExtractor` on the image with updated astrometry) until the solution converges. The convergence criteria is chosen to be a combination of contrast parameter (a measure of difference in correlation peaks in the matching process) and RMS in R.A. and Decl. (good values are $< 1''$). Alternatively, the fitting is stopped after the maximal number of iterations is reached. The convergence (hence the accuracy of the astrometric solution) are indicated by a designated flag output by this module. Successful fits show sub-arcsecond accuracies.
6. The distortion is parameterized as Tangent plane projection with parameter value (PV) polynomial distortion terms (TPV) polynomials [defined in sky coordinates; Shupe et al., 2012] by `scamp`. In a final step, the `wcs-sip2pv` module from the `Astrometry.net` package is used to convert the TPV representation to SIP, defined in pixel coordinates (thus fixed from exposure to exposure).
7. The resulting WCS solution, along with the most recent SIP distortion terms, is written to the header of the output spectral image file. Additionally, a flag (`FINAST`) is added to quantify the accuracy of the derived astrometry.

The performance of the astrometry is evaluated by computing a sigma-clipped RMS of the spatial difference between derived positions and the position of known Gaia and 2MASS stars, and reaches sub-arcsecond accuracy (see Section 4.2.2). The flag `FINAST` (provided in the calibrated image header) gives an overall estimate of the robustness of the solution based on the output of the last (best) `scamp` iteration. In addition to the `scamp` output parameters (listed in step #5 above), this flag is also determined by the uniformity of matches between calibrators and extracted sources (non-uniformity may indicate poor astrometry solutions at the image corners). The `FINAST` flag has values of 0 (good astrometry), 1 (partial good astrometry, meaning some offsets in the image corners of a couple of pixels due to bad distortion fit), and higher orders, which indicate poor astrometry (images should not be used).

In pipeline version R7, the main astrometry module run is followed up by the *astrometry retry module*. This step is used to mitigate some of the astrometry fit failures produced by the main astrometry module ($\approx 1-3\%$ and is run for all images with partial or poor astrometric solutions (*i.e.* a `FINAST` flag not equal to zero). The main idea is to use images with successful astrometric solutions as priors ("seeds") and rerun the above pipeline. Seed images are chosen for a failed image by this priority: *(i)* same detector and adjacent small slew, *(ii)* dichroic pairs in same small slew (e.g., detector pairs 1/4, 2/5, or 3/6), and *(iii)* same small slew (any detector). From each of these seeds, astrometric priors for the failed image are computed assuming the focal plane is a rigid body. Furthermore, the distortion of the seed image is used. The main astrometry module is subsequently run using these priors. With this approach, the number of images with failed astrometric solution is reduced to sub-percent level. After this retry, the `FINAST` flag is updated. In addition, four keywords are added to the image header. These are *WCSRETRY*, *RETRY_WCSMODE*, *WCSSEED*, and *WCSSEEDOBS*, which indicate that the image run through the retry mode, the retry mode (small slew, dichroic, etc), the detector number of the seed, and the observation ID of the corresponding seed image, respectively.

[9] `https://data.astrometry.net/`

3.2.9 Source Masks

This processing unit generates an image-plane mask for each spectral image to identify pixels with significant flux contributions from known sources. The module operates on spectral images with valid WCS information, assigning mask bits in a dedicated flag array at pixel locations corresponding to known source positions. The mask array is returned as output, while the original image data remains unaltered. The corresponding inputs and outputs of this processing step are summarized in Table 18.

Table 18: Inputs and Outputs of the Source Mask Module

Input	Output
Spectral images, Reference Catalog information, `SUR` flags propagated from the lower-level data	Binary array of mask flags

Input and Output Description The inputs to this module include a spectral image with dimensions of 2,040 × 2,040 pixels, along with WCS information derived from the astrometric solution described in Section 3.2.8. It also requires an associated mini-catalog that includes the pixel coordinates and estimated brightnesses of all sources expected to appear in the image or the surrounding frame. This catalog is generated from the Reference Catalog and the known Solar System object catalog. To properly account for sources that may fall partially off the detector edge or produce optical ghosts, the mini-catalog includes all relevant sources within 0.5° of the array boundaries. The Reference Catalog input used by this module includes all necessary flags that determine which sources should be masked. Pipeline version 6.4.0 and data products from qr-2 use a version of the Reference Catalog (v0.73) which updates the magnitudes for very bright sources. In addition, this module requires the SUR flags propagated from the lower-level data processing.

The output is a binary mask array with the same dimensions as the input image (2,040 × 2,040 pixels), where each bit encodes the presence of a masked source. The information contained in this mask array is used to update the pixel-level flag map described in Section 3.2.5 and is stored as metadata in the headers of spectral images (see Table A.35).

Description of Algorithm The current implementation of the module generates masks for astronomical sources. The masking framework also includes prescriptions for electrical crosstalk, DBS ghosts, and frame edge ghosts.

The module uniquely masks unresolved sources, such as stars and compact galaxies. Resolved objects such as large nearby galaxies or planetary nebulae are not currently included in the masking. Masking is based on the expected PSF profile in each band and the predicted source brightness.

The algorithm iterates over all cataloged sources requiring masking. These sources are flagged in the SPHEREx Reference Catalog with a `spherex_class` bit value ≤7. For each source, a masking radius is computed as a function of the predicted source brightness in the observed SPHEREx band. All pixels for which at least 20% of the pixel area lies within the circular masking region are assigned the value `SOURCE`.

The radius as a function of magnitude—originally approximated with simulated images—was re-derived using on-sky data. Circles were drawn around a large number of sources in narrow magnitude bins until the enclosed regions were visually consistent with encompassing the full source flux, including the faint wings of the PSF. Bright stars were intentionally included to determine the appropriate scaling at the highest fluxes. The measured radii were then fit with a smoothly blended exponential model having detector-dependent parameters:

$$r(m) = \exp[(1 - s(m))(a_1 + b_1 m) + s(m)(a_2 + b_2 m)]\,, \tag{14}$$

where

$$s(m) = \frac{1}{1 + \exp[-(m - m_0)/w]}. \tag{15}$$

The best-fit parameters for each array are summarized in Table 19, while Table 20 summarizes the parameter values implemented in the source masking algorithm. Sources fainter than 19 AB magnitude are not masked by default.

Table 19: Parameters fit to the source mask radius scaling relation in Eqs 14 and 15.

Band	a_1	b_1	a_2	b_2	m_0	w
1	6.020	−0.2364	1.623	−0.048	10.175	2.112
2	6.097	−0.3016	4.539	−0.212	8.190	1.552
3	5.845	−0.3020	2.245	−0.075	12.364	2.066
4	11.193	−0.1271	0.566	−0.001	0.998	6.278
5	6.005	−0.2561	2.729	−0.096	9.314	1.979
6	5.631	−0.2801	3.174	−0.124	10.950	2.007

Table 20: Implemented Algorithm Parameters

Parameter	**Value**
Masking radius versus source brightness	see Table 19
Default faint masking limit	19 AB mag
Class 1 crosstalk threshold	0.3 $e^- s^{-1}$ (SWIR only)
Class 2 crosstalk threshold	0.3 $e^- s^{-1}$
DBS ghost masking relations	see Tables 21 and 22
Frame edge ghost source brightness threshold	$m_{AB} \leq 11$
Frame edge ghost mask length	$\lceil 11\left(25,000 \cdot 10^{-m_{AB}/2.5} + 24\right)\rceil$ pixels
Frame edge ghost mask width	$2\lceil 4\left(25,000 \cdot 10^{-m_{AB}/2.5} + 1\right)\rceil$ pixels

Masking Type II: Electrical Crosstalk

The masking framework identifies three classes of electrical crosstalk from on-orbit calibration data. Type 1 consists of vertically displaced ghosts produced by the detector row-chopping readout and is present only in the SWIR detectors. Type 2 consists of horizontally displaced ghost images arising from electrical coupling between detector readout channels and is present in all detector arrays. Type 3 consists of streak-like artifacts associated with bright sources located near electrical channel boundaries and is observed in the MWIR detectors. The current implementation applies masking for Types 1 and 2 using calibration-derived coupling lookup tables; affected pixels are assigned the `CROSSTALK` mask bit. A prescription for Type 3 masking has been defined and is being tested but is not currently implemented in the pipeline for R7.

Dichroic Beamsplitter Ghosts: In addition to the adding the source mask flags, this module also calculates and sets the flags for the dichroic beamsplitter (DBS) reflection ghosts.

DBS ghosts are reflections from the filters in front of the instrument. Significant reflections are induced only by very bright sources, ≥100 Jy. To mask these reflections, we need information about sources falling in a region of interest (ROI) up to 0°.5 outside of the nominal array footprint for each of Bands 3−6 (Bands 1 and 2 do not suffer from this effect). While DBS ghost production is a continuous optical process, for modeling simplicity we define two regions that produce ghosts: the "main field" and the "edge". Main field ghosts are produced by Bands 4, 5 and 6, while edge region ghosts are produced by bands 3 and 4, concentrated close to the beam splitter spectral discontinuity region. Finally, due to an optical bleeding effect, in Band 4 only bright sources falling in the edge region also cause us to mask the entire strip nearest the short wavelength side of the detector. The masking prescription for each region and band is characterized by the following parameters: flux of source generating the ghost B; ghost spatial position function parameterized in terms of a shift with transformation given by α; and mask radius r. The geometric model for the bands all follow

the same pattern, which looks like a linear transformation:

$$x_g = x_s + \alpha_{xx} x_s + \alpha_{xy} y_s + \alpha_{ox} \tag{16}$$
$$y_g = y_s + \alpha_{yx} x_s + \alpha_{yy} y_s + \alpha_{oy} \tag{17}$$
$$\tag{18}$$

with the labels x_g for ghost image position, x_s for source image position, 'o' for offset, and the subscripts of α indicating they can be written in matrix form. Pixel positions are given according to the Level-2 standard, with $y = 0$ being the long wavelength side of a detector. The H-band flux of the sources are approximated in the pipeline by the predicted magnitudes in Bands 1-4 that come from interpolating the SPHEREx Reference Catalog fluxes.

Band 3 Band 3 only exhibits ghosts near the DBS discontinuity, so the ROI for masking in Band 3 is a rectangle that extends $-52 < x_s < 2092$, $-250 < y_s < 175$. The model parameters for Band 3 are given in Table 21.

Table 21: DBS Ghost Mask Model Parameters for Edge Region Bands

Band	B	α_{xx}	α_{xy}	α_{ox}	α_{yx}	α_{yy}	α_{oy}	r
1	Does not exist	0	0	0	0	0	0	0
2	Does not exist	0	0	0	0	0	0	0
3	100 Jy in H-band	−0.0051	0.0013	−5	0	0	225	52
4	100 Jy in H-band	0	0	10	0	0	221	52
5	Does not exist	0	0	0	0	0	0	0
6	Does not exist	0	0	0	0	0	0	0

Band 4 This Band exhibits both kinds of ghosts. For the main region ghosts, the minimum ROI is the rectangular region encompassed by $-52 < x < 2092$, $52 < y < 2261$. The model parameters for this region are listed in Table 22.

Table 22: DBS Ghost Mask Model Parameters for Main Field sources

Band	B	α_{xx}	α_{xy}	α_{ox}	α_{yx}	α_{yy}	α_{oy}	r
1	Does not exist	0	0	0	0	0	0	0
2	Does not exist	0	0	0	0	0	0	0
3	Does not exist	0	0	0	0	0	0	0
4	3000 Jy in H-band	0	0	5	0	0	221	52
5	10,000 Jy in H-band	−0.0042	0.0005	0.1	0	0	225	52
6	10,000 Jy in H-band	−0.0043	0.0013	9.4	0	0	225	52

For the edge region, the ROI extends $-52 < x_s < 2092$, $1760 < y_s < 2040$. Sources falling in this region are flagged using the geometric model given in Table 21.

In addition, for very bright sources with $B > 3000$ Jy in H-band), the entire region $-52 < x < 2092$, $y > 1920$ is masked to account for a optical bleeding effect that is difficult to fully model and rare.

Band 5 This Band only exhibits the main field ghost, and only for the very brightest sources. The minimum ROI is the rectangular region encompassed by $-52 < x < 2092$, $52 < y < 2265$. The model parameters for this region are listed in Table 22.

Band 6 This Band only exhibits the main field ghost, and only for the very brightest sources. The minimum ROI is the rectangular region encompassed by $-52 < x < 2092$, $52 < y < 2265$. The model parameters for this region are listed in Table 22.

For ghosts whose incident source falls on the same detector array as the ghost falls, the masking flag 'GHOST' is set for each pixel falling into the masking region. For ghosts whose incident source does not fall on the detector, the masking flag 'GHOST_EXT' is set for each pixel falling into the masking region.

3.2.10 Outlier Pixel Detection

This processing unit detects and flags transient events in each spectral image that may have bypassed onboard flagging procedures. It operates by applying a sigma-clipping algorithm to a median-filtered image with known sources masked. The output of this module contributes to updating the bad pixel inventory and is stored as metadata in the headers of spectral images (see Table A.35). The corresponding inputs and outputs of this processing step are summarized in Table 23.

Table 23: Inputs and Outputs of the Outlier Pixel Detection Module

Input	Output
Spectral images, `SOURCE` mask, Bad pixel mask, `VARIANCE` mask	New pixel mask images

Input and Output Description The inputs to this module consist of a spectral image with dimensions of 2,040 × 2,040 pixels, along with the associated `SOURCE` mask, bad pixel mask, and variance estimates.

For each exposure, the module generates a flag array matching the input image dimensions. This output array includes two new flag types (`OUTLIERS` and `STREAK`), identifying statistically significant deviations from expected signal levels and detected satellite streaks, respectively. Definitions of these flag values are listed in Table 16 in Sect. 3.2.5.

Description of Algorithm The algorithm begins by applying a median filter to the spectral image to suppress the overall mean signal and remove low spatial frequency variations. It then applies the `SOURCE` and bad pixel masks (Sect. 3.2.5) to exclude any pixels already known to be unreliable or associated with astrophysical sources. From the remaining unmasked pixels, the module identifies isolated statistical outliers as well as satellite streak seeds, i.e, pixels whose signal exceeds a pre-defined threshold in units of variance. For satellite streak seeds, the threshold is set to a slightly lower value to allow for detection of tracks even only marginally above the noise level. The isolated pixel outliers are immediately flagged as `OUTLIERS` in a 2,040 × 2,040 binary mask. As for the streak seeds, the modules continues by broadly following the steps of the Zwicky Transient Facility (ZTF) pipeline (see Laher et al. [2014]), that is: neighboring seeds are grouped together and fitted to a linear model, which allows the estimation of the length, width, aspect ratio and orientation for each group; elongated, line-like objects are retained and labeled as streak fragments; finally, contiguous tracks from adjacent, co-linear fragments are created, and all the pixels belonging to the same track are flagged as `STREAK` in the binary mask.

3.2.11 Zodi Prediction

One of the 2,040 × 2,040 pixel layers in the LVF multi-extension files provides a median estimate, per image and in units of MJy/sr, of the Zodiacal Light (ZL) spectrum obtained from the first-year SPHEREx measurements (see Section 2 for more information on the structure and content of the LVF multi-extension files). Importantly, this ZL median signal *is not* subtracted from the LVF images.

The ZL estimate is obtained by using, as a first guess, the predictions from the modified Kelsall et al. [1998] model (updated with Planck data) combined with the spectral measurements by Tsumura et al. [2013] (see more details in Crill et al. [2025]). A careful analysis performed by the SPHEREx Science Team has revealed that, although the Kelsall et al. [1998] model is able to capture quite accurately the ZL spatial and temporal variations as observed by SPHEREx, it typically underestimates its amplitude. For this reason, a scaling factor, as a function of wavelength, was derived from cross-correlating the ZL model-based predictions

with the actual SPHEREx measurements. For the purpose of this analysis, all SPHEREx Year-1 exposures at $|b| > 30\circ$ are used, and a median scaling factor is computed, per wavelength, across all considered exposures. At this high latitudes, the sky is assumed to be dominated by the ZL, with additional contributions from, e.g., the the Diffuse Galactic Light (DGL) and the Integrated Galaxy Light (IGL). The result of the comparison gives a per-wavelength, all-sky calibration of the modified ZL Kelsall et al. [1998] model, and this is recorded as a layer in the LVF multi-extension files. The scaling factor as a function of wavelength is one of the calibration files available from IRSA (Sec. 4.3.4).

3.2.12 Level 2 DQA

A series of simple, automated "sanity" checks is executed to verify the quality of the data, following the L2 processing, and before the data can be ingested into the archive.

The following tests are performed on a per-image basis:

- **Nonlinearity:** No pixel in the image has a measured flux corrected by more than 50%
- **Variance:** The measured per-pixel variance in the image is within the expected range
- **Persistence:** No more than 20% of the pixels in the image are flagged with the `PERSIST` flag
- **Bad-Pixel Mask:** No more than 1% of the pixels in the image are flagged;
- **Source Count:** The number of astronomical sources found in the image is within the expected range
- **Source Mask:** The number of masked pixels in the exposure is < 3 times the number of sources identified in the image from the Source Reference Catalog.
- **Outlier Pixels:** The number of pixels flagged as `OUTLIER` is within a factor of 2 of the total number of pixels already flagged for other reasons
- **LVF layers:** All required layers (data, flags, uncertainty, ZL, PSF cube) are present and correctly attached to the LVF file
- **Missing Value Pixels:** All `NaN` or `Inf` pixels are properly flagged
- **Distortion:** The image median of the pixel solid angles is within the expected range
- **Astrometry:** The image astrometry has been successfully computed (`FINAST` = 0).

If at least half of the eleven checks above are successful, the image is assigned an overall `PASS` grade. Overall, a spectral image is included in the archive at IRSA if the following three conditions are verified:

- `N_TRANSIENTS` $<$ 435,000
- Not included in the defined boundaries for the South Atlantic Anomaly (SAA).
- `FINAST` flag = 0 (Sec. 3.2.8)
- `L2DQA` = PASS

As the data quality assessments are evaluated per spectral image band, some observations will not include all 6 bands in the archive.

3.3 Photometric Measurements

The photometry module described here is used to derive photometric measurements used as part of deriving the absolute gain matrix (Sect. 4.1.1). It is also used in the Spectrophotometry Tool hosted at IRSA, which allows users to make photometric measurements of specified sources from the spectral images. Here we describe how those photometric measurements are made.

This processing unit performs photometric measurements of astrophysical sources by leveraging astrometric and source morphology information provided by the user, along with the pixel-level flag information propagated from preceding modules. The primary objective is to obtain optimally deblended photometry using prior knowledge. The corresponding inputs and outputs of this processing step are summarized in Table 24.

Table 24: Inputs and Outputs of the Forced Photometry Module

Input	Output
Spectral images, Source information, `ePSF` model, Variance map, Pixel solid angle map, Flag map,	Photometry catalog

Input and Output Description The inputs to this module include spectral images, each containing a WCS solution capable of translating RA/DEC coordinates to pixel positions and to the associated wavelength. These images are dark-subtracted, flat-fielded, and brought to the physical unit of flux surface density (MJy/sr), enabling conversion of photometric measurements to absolute fluxes. The module works by finding the maximum likelihood solution for source fluxes by comparing the measured image with a generative model that predicts the scene given the instrument `ePSF` and known source positions. While not required, intrinsic galaxy morphology can be supplied for the generative modeling. Additional inputs used by the photometry tool include the variance map (Sect. 3.2.3), the position-dependent `ePSF` calibration product (Sect. 4.1.2), a pixel solid angle map incorporating optical distortion information, and flag maps (Sects. 3.2.5 and 3.2.10). Eventually, a derived sub-pixel response map may be incorporated as well, but is not currently implemented.

The output of this module is a catalog of fluxes for all objects provided as input. For each source, the catalog reports the source ID (as defined in the input catalog), measured flux and associated uncertainty, the corresponding wavelength, and the (i, j) pixel coordinates. It also includes fit quality flags and a goodness-of-fit metric derived from the residual between the observed and modeled image. Please note that the best performance will in general be obtained if all sources that may contribute substantial flux in a given scene are provided for the fit.

Description of Algorithm The algorithm is based on the `Tractor` software package[10], which uses generative modeling of astronomical images to measure a maximum likelihood solution. The `Tractor` constructs a model of the image by combining this prior information with instrument characteristics and then optimizes the model parameters by fitting to the observed data. The spatially varying `ePSF` calibration models described in Sect. 4.1.2 are used to generate the point-source response appropriate for each detector location. This forward modeling approach has been adopted in other tools, such as `xID` [Hurley et al., 2017] and `T-PHOT` [Merlin et al., 2016], which are tailored for crowded-field photometry with point sources and extended morphologies, respectively. The flexibility of the `Tractor` makes it well suited for SPHEREx photometry.

Background subtraction A global spectral background is first computed for the full image using pixels not flagged as bad or containing source flux. This global background component is then removed. In addition, in the cutout provided to Tractor, a local background component is included as part of the generative model, with the residual local background level fit simultaneously with the source fluxes during the optimization.

Forced photometry We use the `Tractor` in forced-photometry mode, applying it to sources with known positions and morphological models provided by the user. Source positions are not floated in the fit. The statistical foundations and modeling framework are described in Hogg et al. [2010], while the underlying optimization methods are based on the `emcee` affine-invariant ensemble sampler [Foreman-Mackey et al., 2013].

The following outlines the step-by-step implementation of the photometry module:

1. Load the input catalogs containing source positions, flags, and optionally, morphological parameters.
2. Convert celestial coordinates to detector pixel coordinates (i, j).

[10] `http://thetractor.org`, `https://github.com/dstndstn/tractor`

3. Construct a cutout containing the source(s) of interest.
4. Estimate an initial local background from a 15×15 region surrounding the cutout after masking known sources.
5. Retrieve the position-dependent `ePSF` model for the corresponding detector region.
6. Use the `Tractor` to construct a generative model of the cutout, incorporating source positions, morphological models, the local `ePSF`, and a local background component.
7. Fit the generative model simultaneously for the source fluxes and local background using the cutout data and associated variance map.
8. Convert the fluxes reported by the `Tractor` to μJy using the local pixel solid angle, derived from the distortion map.
9. For each source in the central cutout, record the fitted flux, flux uncertainty, and corresponding wavelength.
10. Increase the reported flux uncertainties to account for an observed irreducible scatter not fully captured by the variance map (see Note 1 below).
11. Check for flagged pixels affecting each object and propagate the relevant flags to the output catalog. Apply additional photometry-specific flags indicating potential issues, such as strong non-linearity or saturation.
12. Compute a fit quality metric (as defined in Note 2) based on the residual between the model and data within a defined aperture around each source.

Note 1: Photometric Uncertainty Correction The statistical uncertainties reported by the `Tractor` are derived from the propagated variance map. Analysis of repeated measurements of stars indicates an additional irreducible scatter that is not fully captured by the variance layer. To account for this effect, the reported catalog uncertainties are increased according to

$$\sigma^2_{\text{reported}} = \sqrt{\sigma^2_{\text{Tractor}} + (0.03 \cdot F)^2} \tag{19}$$

where F is the measured source flux. The additional term corresponds to a 3% systematic uncertainty added in quadrature to the statistical uncertainty and primarily affects high signal-to-noise measurements. The image variance map itself is unchanged. The correction is applied only to the catalog-reported photometric uncertainties.

Note 2: Fit Quality Metric A simple metric will be reported for each photometered source based on the residual between the model and the image in comparison with the per-pixel uncertainty. For each source, we define a `CirclePixelRegion`[11] around its sub-pixel position of radius 2.5 SPHEREx pixels. For pixels k falling within this region, we compute

$$\texttt{fit_quality} = \langle |p_k - m_k| / \sigma_k \rangle, \tag{20}$$

where p_k is the pixel value in the Level 2 image, m_k is the `Tractor` model value at pixel k, and σ_k is the uncertainty in pixel k from the variance map. The fit quality should tend to be close to 1 for good fits and will be significantly larger if something went wrong.

Flag usage We suggest masking flagged pixels in the following ways when estimating photometry from the calibrated spectral images, following the behavior of the pipeline and photometry tool.

Flags for background estimation masking (see Table 16 for more info):

- OVERFLOW
- SUR_ERROR
- NONFUNC
- MISSING_DATA

[11] From the `AstroPy Regions` package.

- HOT
- COLD
- NONLINEAR
- PERSIST
- OUTLIER
- SOURCE
- TRANSIENT
- BLOOM
- SNOWBALL
- HALO
- SATELLITE_HALO

Flags for masking pixels for photometry calculations:

- SUR_ERROR
- NONFUNC
- MISSING_DATA
- HOT
- COLD
- NONLINEAR
- PERSIST
- BLOOM
- SNOWBALL
- HALO
- SATELLITE_HALO

In addition to excluding selected flagged pixels from the photometric fit as described above, the L3 photometry outputs an integer bitmask `flags` that encodes pixel flags that could have impacted the photometry. This bitmask includes a summary CONTAINS_BAD_PIXEL (bit 32) warning flag. This flag is set when one or more pixels within a radius of 2.5 SPHEREx pixels from the source position have any of the following pixel-level flags set: TRANSIENT, OVERFLOW, SUR_ERROR, NONFUNC, DICHROIC, MISSING_DATA, HOT, COLD, NONLINEAR, CROSSTALK, GHOST, GHOST_FPA, GHOST_EXT, STREAK, PERSIST, BLOOM, SNOWBALL, HALO, or SATELLITE_HALO. Thus, CONTAINS_BAD_PIXEL is a conservative warning that potentially problematic pixels occur near the source. However, it should only be interpreted as a warning and does not necessarily imply that the measurement should be excluded from scientific analyses. The exact combination of flags impacting a measurement can be inferred from the `flags` bitmask and used to make selection rules.

3.4 Mosaics

3.4.1 Overview

The SPHEREx pipeline has the ability to create image mosaics from SPHEREx Level 2 (L2) calibrated spectral images. This processing combines multiple L2 images taken at different times and spacecraft orientations to produce co-added images for each spectral channel. This capability is used within the Mosaic Tool hosted by IRSA and for the all-sky data cubes which are part of the Year 1 and Year 2 Data Releases (see Sect. 2.1). Currently, this document describes the functionality for the IRSA Mosaic Tool. The IRSA Photometry Tool will continue to use the L2 calibrated images and does not use mosaics as input. For science applications requiring precision photometry, we recommend using the L2 spectral images directly.

The mosaic creation process consists of the following high-level steps, each described in more detail below.

1. Query and load L2 spectral images covering the target region
2. Subtract the zodiacal light model (L2 image ZODI extension) from each image
3. Apply bad pixel masking based on quality flags (L2 image FLAGS extension)
4. For each spectral channel, extract pixels using a channel template (Sec. 3.4.4). The channel template and pre-calculated channel statistics are available as the spectral_channels calibration product.
5. Reproject extracted pixels to a common output grid
6. Accumulate weighted contributions from all images
7. Produce final averaged mosaic

3.4.2 Input Data

Each L2 FITS file contains data from one of the 6 detectors for a single exposure and includes IMAGE, ZODI and FLAGS extensions, as described in Sec. 2.2.

For the initial release of the Mosaic Tool, only L2 images from the All-Sky Survey are included. Images from Deep Field Surveys are excluded.

3.4.3 Data Loading and Preprocessing

When loading an L2 file, the tool performs the following steps:

1. Zodiacal Light Subtraction: The zodi-subtracted science image is computed as: data = IMAGE - ZODI
2. Bad Pixel Masking: Pixels with any of the following quality flags are set to NaN and excluded from the mosaic (see Sec. 3.2.5 for definitions):
   - TRANSIENT, SUR_ERROR, NONFUNC, DICHROIC, MISSING_DATA
   - HOT, COLD, PHANMISS, NONLINEAR, PERSIST
   - CROSSTALK, GHOST, GHOST_FPA, GHOST_EXT
   - STREAK, BLOOM, SNOWBALL, HALO, SATELLITE_HALO
3. Flag Propagation: The following flags are propagated to the output mosaic: OVERFLOW, SOURCE, OUTLIER (see Sec. 3.2.5 for definitions).

3.4.4 Spectral Channel Definition

SPHEREx uses Linear Variable Filters (LVFs) to provide spectroscopic capability. Each LVF creates a gradient across the detector where wavelength varies continuously with position along one axis (see Sec. 1). This combination of spatial and spectral information within each exposure must be disentangled by the mosaic process.

The tool uses a pre-defined spectral channel template to set the spectral channels. This template encodes which detector pixels belong to which spectral channel, following the natural geometry of the LVF response:

- Each detector array is divided into 17 standard spectral channels (subchannels).
- The contour boundaries follow iso-wavelength lines across the detector, but are not straight lines.
- The same contour template applies to all six bands, but each band covers a different wavelength range.

The spectral channels template is a 2D integer array where:

- Values 1-17 indicate the spectral channel number
- Other values (0 and 18) indicate pixels outside any standard channel (e.g., edges, corners)

A FITS file with the spectral channel definitions is available at IRSA and described in Sec. 4.3.2.

For each combination of array and subchannel, the following statistics are pre-computed from pixel-center wavelength and bandwidth calibration maps:

Parameter	Description	Derivation
WAVELENGTH	Median wavelength	Median of per-pixel wavelengths within channel mask
WL_MIN	Minimum wavelength	Minimum per-pixel wavelength (3-sigma clipped)
WL_MAX	Maximum wavelength	Maximum per-pixel wavelength (3-sigma clipped)
R	Median resolving power	Median of per-pixel R within channel mask
R_STD	R variation	Standard deviation of input per-pixel resolving power
BANDWIDTH	Median bandwidth	Median of per-pixel bandwidth within channel mask

These pre-computed statistics are stored in the SPECTRAL_CHANNELS extension of calibration products, eliminating the need to recalculate them during mosaic construction.

3.4.5 Mosaic Grid

The Mosaic Tool creates a grid for the requested mosaic using parameters defined by the user:

- The center of the grid in right ascension and declination
- Width and height of the mosaic
- Pixel size (minimum of 9 arcsec)
- Position angle

The output WCS is constructed with the following constraints:

- Odd pixel dimensions in both axes to ensure the reference pixel falls exactly at the grid center
- Reference pixel (CRPIX) at the geometric center using FITS 1-based indexing
- Pixel scale with RA increasing to the left (negative CDELT1) per standard convention
- TAN (tangent-plane) output map projection

For a grid of width W deg and height H deg with pixel scale p arcsec, the number of pixels in the x and y directions (nx and ny) are:

- $nx = floor(W * 3600/p)|1$ (force odd)
- $ny = floor(H * 3600/p)|1$ (force odd)
- $CRPIX = (nx/2 + 0.5, ny/2 + 0.5)$

3.4.6 Reprojection Algorithm

The mosaic tool uses a histogram-based reprojection as its primary method (see Cukierman et al. [2026], Section 4 for details). This is implemented as an intensity-weighted 2D histogram of the image-pixel position. In this binning scheme, each input pixel contributes to only a single mosaic pixel.

For each input image, the reprojection computes a mapping from input to output pixel coordinates:

- Build input pixel grid: Create coordinate arrays (ix, iy) for each pixel in the input image
- Input to Sky transform: Convert input pixel coordinates to sky coordinates (RA, Dec) using the input WCS
- Sky to Output transform: Convert sky coordinates to output pixel coordinates using the output WCS
- Nearest-neighbor assignment: Round output coordinates to the nearest integer pixel

Mathematically, for input pixel (x_{in}, y_{in}):

$$(RA, Dec) = \text{WCS_in.pixel_to_world}(x_{in}, y_{in})$$
$$(x_{out}, y_{out}) = \text{WCS_out.world_to_pixel}(RA, Dec)$$
$$(i_{out}, j_{out}) = \text{round}(x_{out}, y_{out})$$

Values are accumulated using histogram binning with the python function *np.bincount*:

$$\text{accumulator}[j_{out}, i_{out}] += \text{data}[y_{in}, x_{in}]$$
$$\text{nhits}[j_{out}, i_{out}] += 1$$

The final mosaic is the weighted average:

$$\text{mosaic} = \text{accumulator/nhits} \quad (\text{where nhits} > 0)$$
$$\text{mosaic} = \text{NaN} \quad (\text{where nhits} = 0)$$

where nhits is the number of contributing input pixels per output mosaic pixel.

The properties of the adopted reprojection algorithm are:

- Speed: O(N) complexity, fast for large images
- No smoothing: Each input pixel contributes to exactly one output pixel
- Integer hit counts: NHITS is always an integer pixel count
- No noise correlation: Independent pixel assignments
- Presence of gaps: Some output pixels may have no input data if coverage is sparse

This method is equivalent to the "pixel binning" approach described in Cukierman et al. [2026].

3.4.7 Mosaic building process

The mosaic builder uses a file-centric optimization: each L2 file is opened once, and all spectral channels are processed before moving to the next file. This reduces file I/O by a factor of 17x compared to processing one channel at a time.

For each spectral channel, the accumulation proceeds as:

```
Initialize:
    acc_data[ny, nx] = 0        # Weighted sum accumulator
    nhits[ny, nx] = 0           # Hit count
    acc_flags[ny, nx] = 0       # Bitwise OR of flags
```

```
For each L2 file:
    Load image and flags
    Apply bad pixel mask (set bad pixels to NaN)
    Extract pixels within a spectral channel mask
    Compute pixel mapping (input to output)

    For each valid (non-NaN) pixel:
        acc_data[j_out, i_out] += value
        nhits[j_out, i_out] += 1

    For each pixel (including NaN):
        acc_flags[j_out, i_out] |= propagated_flags

Finalize:
    mosaic = acc_data / nhits   (where nhits > 0)
```

The accumulation kernel is implemented using Numba's JIT (just in time) compilation for native performance, running outside Python's Global Interpreter Lock to enable multi-threaded file loading.

3.4.8 Output File

The individual channel mosaics are combined into a 3-dimensional spectral cube in FITS format with the following extensions:

Extension	Content	Shape	Description
PRIMARY	-	-	Version metadata
IMAGE	3D cube	(N, ny, nx)	Stacked mosaics (MJy/sr)
NHITS	3D cube	(N, ny, nx)	Number of contributing input pixels per mosaic pixel
FLAGS	3D cube	(N, ny, nx)	bitwise OR of flags propagated from contributing input pixels
SPECTRAL_CHANNELS	Table	N rows	Per-channel metadata
WCS-WAVE	Table	1 row	Spectral WCS lookup

The SPECTRAL_CHANNELS binary table contains:

- DETECTOR: Array number
- SUBCHAN: Subchannel number
- WAVELENGTH: Pre-calculated wavelength (μm) from spectral channels file provided by instrument team
- WL_MIN, WL_MAX: Pre-calculated wavelength range (μm) from spectral channels file provided by instrument team
- BANDWIDTH: Pre-calculated bandwidth (μm) from spectral channels file provided by instrument team
- R, R_STD: Pre-calculated resolving power statistics from spectral channels file provided by instrument team

The cube uses the FITS -TAB algorithm for tabular spectral coordinates. This allows non-uniform wavelength sampling to be accurately represented:

- Axis 3 (WAVE-TAB): Wavelength lookup from WCS-WAVE table
- Axis 4 (WAVE-TAB): Bandwidth lookup from WCS-WAVE table

The WCS has 4 world axes (RA, Dec, wavelength, bandwidth) even though the image has only 3 pixel axes.

3.4.9 Data Quality and Flagging

Bad pixels are identified by quality flags in the L2 input data, see Sect. 3.4.3 for the list of flags considered as bad by the mosaic algorithms. Pixels with bad flags are:

- Set to NaN before reprojection
- Excluded from accumulation (do not contribute to the weighted average)
- Not included in the NHITS counter

This ensures that bad pixels do not contaminate the final mosaic values.

Selected flags (OVERFLOW, SOURCE, OUTLIER) are propagated to the output using bitwise OR:

```
output_flags[j, i] = input1_flags | input2_flags | ... | inputN_flags
```

This preserves information about which output pixels may be affected by saturated pixels, point sources, or outliers from any contributing input image.

The FLAGS extension header includes MP_<FLAG_NAME> keywords defining the bit position of each propagated flag, following the IPAC Firefly visualization convention (needs reference)

3.4.10 Known Issues

There are several visual artifacts that occur in the output images, mainly due to the spectral sampling of the LVF (Sect. 2.2).

Striping from Airglow Emission Lines: As described in Sect. 2.3, there are several atmospheric emission feasures that can be seen in SPHEREx data. These airglow emission features can create prominent stripe artifacts in SPHEREx mosaics. The most significant is the helium line at 1.083 μm, which appears as a bright horizontal band across all band 1 images. Because the Linear Variable Filter maps wavelength to detector position, pixels sensitive to the airglow wavelength form a stripe pattern that follows the LVF contour geometry.

When multiple exposures are combined into a mosaic, the airglow signal varies both temporally and spatially between observations. This variation creates scan-correlated banding patterns in the final mosaic, where the stripe orientation and intensity depend on the survey scan pattern and the time-varying airglow amplitude. Without mitigation, these stripes can severely contaminate the mosaic, potentially overwhelming faint astrophysical signals at these wavelengths.

Striping from Extended Source Spectral Features: Extended sources with strong spectral features (emission lines, absorption bands) produce similar stripe artifacts. When an extended object has significant flux at a specific wavelength—such as Brackett α emission at 4.052 μm in nebulae — the LVF causes this signal to appear as a horizontal stripe across the detector at the corresponding y-position.

Because SPHEREx observes the same sky region at multiple spacecraft orientations, the stripe orientation rotates between observations. When these images are coadded, the stripes from different roll angles combine to create complex interference patterns. For sources with sharp spectral features, this can produce sawtooth or moiré-like artifacts that do not average down with increased coverage.

The underlying cause is the entanglement of spatial and spectral information inherent to the LVF design: different parts of the field of view are observed at different wavelengths simultaneously, making it impossible to fully separate spatial structure from spectral features within a single exposure.

Residual Artifacts from Incomplete L2 Masking: The L2 bad pixel masks may not capture all detector artifacts. The following known limitations apply:

- Snowballs, blooming, and halo artifacts: Masking for these features was introduced starting with planning period 2025W51_1A (December 2025) and pipeline version 6.5. Quick Release 2 images from prior planning periods have these artifacts unmasked. All images will include this masking after the Year 1 data release.
- Satellite streaks and crosstalk: Masking for satellite streaks is incomplete and crosstalk was not implemented in Quick Release 2 processing. All images will include this masking after the Year 1 data release.

These unmasked artifacts propagate through the mosaic pipeline and appear in the final products.

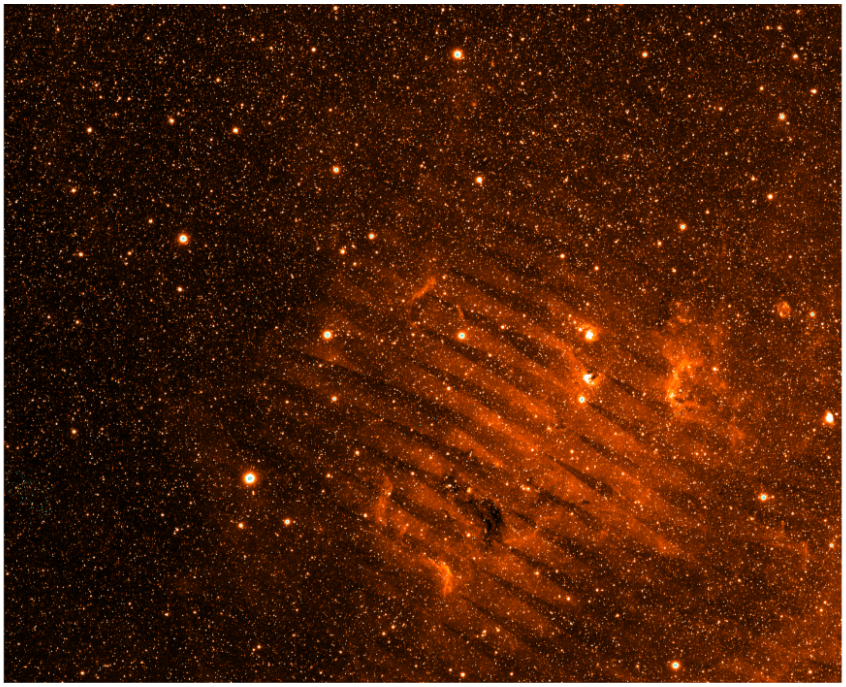

Figure 16: Example of mosaic striping due to an emission line fearure. This is the Brackett α line in the North American Nebula.

4 Calibrations

4.1 Calibration Products

Alongside its science products, SPHEREx generates calibration products that are routinely updated through the data processing pipelines (Sect. 3). These calibration datasets are delivered to the IRSA at regular intervals throughout the mission to ensure continued public access and scientific usability. The data processing pipeline and calibrations used for the QR products are initial versions, updated versions are provided for DR1 as part of the Year 1 reprocessing.

4.1.1 Absolute Gain Matrix

The absolute gain matrix is a calibration product generated by the SSDC Absolute/Photometric Gain Calibration pipeline (Sect. 4.2.1). It characterizes pixel-to-pixel gain variations within a given spectral channel k as well as relative gain differences between spectral channels. This product is delivered in parallel with the spectral images (Sect. 2.2).

Data Format Each matrix (one per detector) encodes the absolute gain G_{ij} for each pixel (i, j), calibrated in units of (MJy/sr) / (e^-/s). It is distributed as a FITS image file with dimensions of 2,040 × 2,040 pixels. This file serves as the input to the Absolute Gain Correction module of the Level 2 pipeline (see Fig. 5).

Image Header Description The header of an absolute gain matrix file encodes key metadata, including the array dimensions and the physical units of the pixel values. A representative header structure is shown in Table B.1.

Data Product Size Each absolute gain matrix file is approximately 16 MB in size.

4.1.2 Effective Point Spread Function (ePSF) models

For R7, we no longer attempt to measure the optical PSF with stacking and deconvolution. Instead, we measure the effective PSF (`ePSF`, Anderson and King [2000]). The `ePSF` calibration product is generated from `SSDC` Level 2 images (Sect. 4.2.3). The detector is divided into a regular spatial grid consisting of 21 × 21 zones for Detectors 1, 2, 4, 5, and 6, and 11 × 41 zones for Detector 3, where the finer sampling along the dispersion direction better captures the small variations present on that detector. The `ePSFs` are derived from stacks of bright, isolated stars accumulated over many exposures, providing high signal-to-noise measurements that show excellent stability with time. The stellar cutouts are combined at an oversampling factor of five relative to the native detector pixels. The `ePSF` building procedure directly measures the effective point spread function, including the combined effects of the optical response, pixel response, and the position of the star within the detector pixels. One `ePSF` is generated for each detector zone and provided as a calibration product alongside the spectral images (Section 2.2).

Data Format Each `ePSF` is represented by a two-dimensional array of size 33 × 33 pixels sampled at an oversampling factor of five relative to the native detector pixels. The calibration product is distributed as a `FITS` binary table containing one row per detector zone. For each zone, the table records the detector grid indices, the center and extent of the corresponding detector region, the number of stars contributing to the solution, the mean effective number of contributing observations, representative wavelength information, and the normalized 33 × 33 `ePSF` image. The detector coordinates stored in the table provide a direct mapping between detector position and the appropriate `ePSF`.

Image Header Description The primary header contains metadata describing the calibration product. The binary table extension contains the per-zone metadata required to associate each `ePSF` with its corresponding detector location, including detector coordinates, zone dimensions, representative wavelength, and summary statistics describing the stellar sample used to construct the calibration.

Data Product Size Each detector `ePSF` calibration file is approximately 8 MB in size.

4.1.3 Dark Current

The dark current maps are calibration products generated by the Absolute/Photometric Gain Calibration pipeline (Sect. 4.2.1).

Data Format Each dark current map (one per detector) encodes the dark current for each pixel (i, j) in units of e^-/s. They are distributed as FITS image files with dimensions of 2,040 × 2,040 pixels. These files serve as the input to the Dark Subtraction module of the Level 2 pipeline (see Fig. 5).

Data Product Size Each absolute gain matrix file is approximately 16 MB in size.

4.2 Calibration Procedures

4.2.1 Photometric/Absolute Gain Calibration Derivation

The absolute gain matrix is derived by combining a flat field / dark measurement with measured gain factors from primary calibrator stars.

Derivation of flat-field / dark current The flat field response of each detector is derived simultaneously with the detector dark current by fitting the response of each pixel in units of e^-/s against a reference flux level measured from the median brightness in the pixel's spectral channel in each image. We define 510 nominal spectral channels per detector for this procedure, such that the background within each channel is expected not to vary significantly in the spectral dimension. Because the detectors are always oriented the same way relative to the Sun, an additional linear tilt is fit within each spectral channel to account for changes in zodiacal background with solar elongation.

Each pixel value is then compared with the global flux prediction at its location. For each image, only pixels expected not to contain significant astrophysical source flux are included in the fit. The slope of the relation over many images for each pixel represents the relative pixel response, or flat field, within the spectral channel, while the intercept yields the detector dark current in e^-/s.

For the current calibration, the flat field and dark current solutions were derived independently from four groups of survey exposures spanning the observing period, with each group containing approximately 4,000 images per detector. The independently derived solutions were found to be stable within the statistical uncertainties, and a final calibration product was obtained by combining all groups into a single solution.

Because the regression procedure removes large-scale modes that resemble the spectral-channel decomposition, an additional restoration step is applied to the flight-derived dark current maps. Large-scale modes measured from laboratory dark-current observations are restored to the flight-derived dark current while preserving the high signal-to-noise small-scale structure measured from the flight data. This correction removes broad artifacts introduced by the regression procedure while retaining the superior sensitivity of the flight-derived solution. The derived flat field responses per detector are shown in Figure 17, and the corresponding dark current maps are shown in

Absolute gain measurement The absolute gain is determined from repeated observations of the primary spectrophotometric calibration stars as they are imaged across each detector. For each accepted observation, the previously calibrated photometry is first converted back into detector count rate by inverting the previous gain matrix and correcting for the local detector pixel solid angle. The expected stellar flux is then computed by integrating the appropriate stellar model through the SPHEREx transmission profile corresponding to the wavelength of the measurement. The predicted point-source flux is converted to an equivalent surface brightness using the detector-average pixel solid angle appropriate for that wavelength. The ratio of the predicted surface brightness to the measured detector count rate,

$$G_{\rm meas} = \frac{I_{\nu,\rm pred}}{(e^-, {\rm s}^{-1})_{\rm meas}} \tag{21}$$

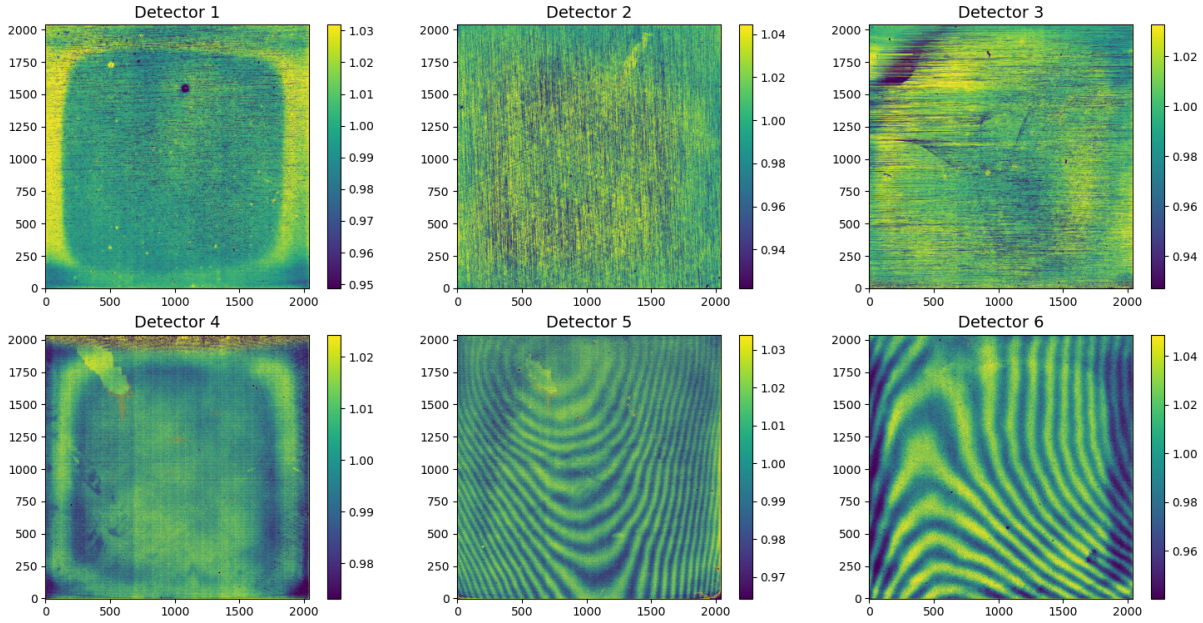

Figure 17: The relative flat field response derived for the six SPHEREx detectors.

constitutes an independent gain measurement for that wavelength.

The primary calibration stars are selected from the `CALSPEC` database [Bohlin et al., 2014, 2017, 2022]. For the current calibration, approximately 54,000 individual measurements of the 17 primary calibration stars were compared with updated HST and JWST stellar spectral models. Measurements are screened using the photometry quality flags and the wavelength range over which each stellar model is considered reliable before inclusion in the gain determination.

Table 25: Stellar magnitude criteria used to select calibrator stars for SPHEREx.

Band	**Wavelength Range** (μm)	**Saturation**†		**High-SNR Threshold (50σ)**	
		AB mag	**Flux** (μJy)	**AB mag**	**Flux** (μJy)
1	0.75–1.11	11.50	91,200	14.74	4,610
2	1.11–1.64	11.50	91,200	14.79	4,410
3	1.64–2.42	11.30	109,600	14.61	5,200
4	2.42–3.82	11.71	75,200	14.85	4,170
5	3.82–4.42	10.19	304,800	13.46	15,000
6	4.42–5.00	9.75	457,100	13.17	19,600

Notes: †: Magnitudes at which nonlinearity effects are expected to manifest based on a pre-launch performance model. All magnitudes are in AB. Flux densities are the corresponding AB flux densities in μJy.

The set of stars used for absolute calibration is summarized in Table 26. These gain measurements are combined as a function of wavelength to derive a one-dimensional gain solution for each detector. The measurements are first grouped in wavelength, a running median is computed, and the resulting trend is adaptively smoothed to suppress statistical noise while preserving genuine spectral structure. The smoothed gain solution is represented by a monotonic piecewise cubic (PCHIP) interpolator and evaluated on the detector wavelength map to produce the final two-dimensional gain matrix. Finally, the gain matrix is divided by the measured flat-field response to produce the absolute gain matrices used to convert detector count rates into physical units of MJy sr^{-1}.

For all standard stars included in the calibration, instrumental fluxes I_{ijk} at detector pixel p_{ijk} are

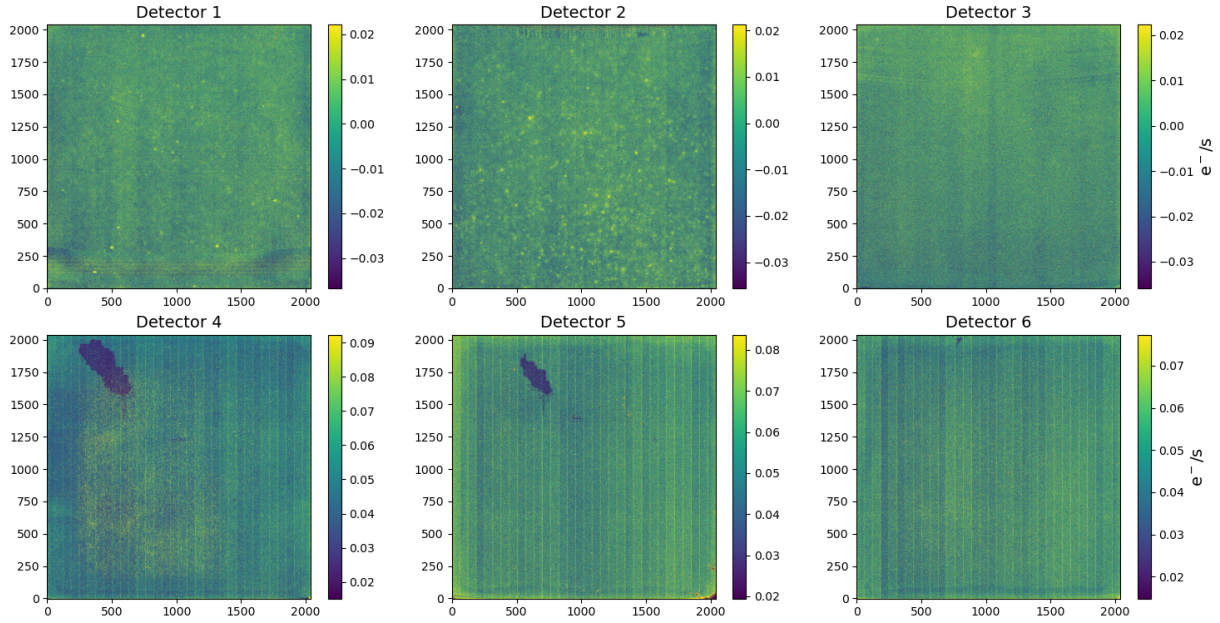

Figure 18: The dark current derived for the six SPHEREx detectors.

regularly collected. In this formulation, i is the detector index, which ranges from 1 to 6, j is the integer observation index, which increments every time a new observation occurs, and k identifies the calibrator star.

The SPHEREx spectral throughput function $t(p_{ijk}, \lambda)$ and the wavelength of peak response $\lambda_{\rm mean}(p_{ijk})$ for every detector pixel are determined from the pre-launch instrument calibration. For each calibrator observation, the corresponding high-resolution stellar spectrum $S_k(\lambda)$ is integrated through the transmission profile appropriate for the measurement wavelength to estimate the expected bandpass-averaged point-source flux,

$$F_{\nu,\rm pred} = \frac{\int t(p_{ijk}, \lambda)\, S_k(\lambda)\, {\rm d}\lambda}{\int t(p_{ijk}, \lambda)\, {\rm d}\lambda}. \tag{22}$$

The predicted point-source flux is converted to an equivalent surface brightness, denoted $I_{\nu,\rm pred}$, by dividing by the detector-average pixel solid angle appropriate for the corresponding wavelength.

The previously derived absolute gain matrix $G_{\rm abs}(p_{ijk})$ and the local detector pixel solid angle $\Omega_{ijk} = \Omega_{\rm pix}(p_{ijk})$ are then used to invert the previous calibration and recover the measured detector count rate,

$$(e^-\,{\rm s}^{-1})_{\rm meas} = \frac{I_{\nu,\rm meas}}{G_{\rm abs}(p_{ijk})}, \tag{23}$$

where $I_{\nu,\rm meas}$ is the measured surface brightness in the calibrated image. Comparing the predicted surface brightness $I_{\nu,\rm pred}$ with the recovered detector count rate yields an independent estimate of the detector gain.

In regions where the detector response varies smoothly with wavelength, the running-median solution provides an accurate representation of the gain. Around the dichroic transition, however, the gain changes more rapidly with wavelength. For the current calibration, measurements carrying only the `DICHROIC` quality flag are retained, and a more local interpolation is used through the transition region. This treatment substantially reduces residual structure in the primary calibrator measurements near the dichroic transition while preserving continuity with the remainder of the detector response.

The resulting one-dimensional gain solutions are evaluated on the detector wavelength maps and combined with the measured flat-field response to produce the final absolute gain matrices used to convert SPHEREx images from e^-/s to MJy,sr^{-1}. The resulting gain matrices are shown in Figure 19.

Calibration uncertainty The uncertainty in the absolute calibration is estimated using observations of the primary calibration stars after application of the final gain matrices. All the primary spectral calibrators are bright, well-known standards drawn from the HST / CALSPEC database, for which the team has assembled reference spectra with very high per-channel significance. They include A stars, white dwarfs, and F and G stars, i.e., a diversity of spectral types. Therefore, the dominant sources of uncertainty in the SPHEREx absolute calibration are the systematics attached to the HST / CALSPEC standards themselves, which we estimate to be of order 1% or less, once they are averaged over the stars. For the great majority of SPHEREx channels, the absolute flux calibration is determined to an accuracy of <1% relative to these reference spectra, with uncertainties of similar magnitude. See Ashby et al. 2026 (in prep) for more details.w

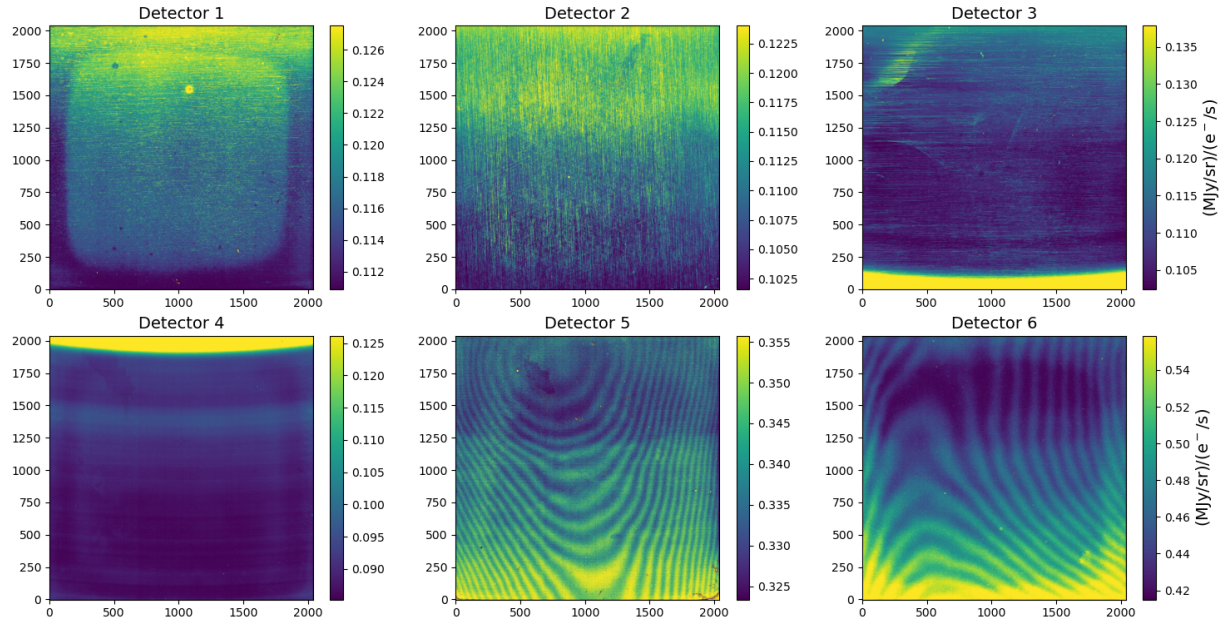

Figure 19: The absolute gain matrices used to convert SPHEREx images from engineering to physical units.

4.2.2 Astrometric Calibration Derivation

The initial pointing (coarse astrometry) for each exposure of each detector is derived from the planned pointing and rotation angle (Sect. 3.1). The predicted position of the six detectors is computed by extrapolating the coordinate grid from detector five assuming an average focal distortion map. In the pipeline version R6.5 and later, these calculations have been significantly improved with respect to past versions of the pipeline code. Specifically, additional shifts and rotations were added to the coarse astrometry solution, which are calculated from the true pointing. These additional adjustments lead to a final coarse astrometry pointing accuracy that is more than a factor of two better than in data processed with pipeline version < 6.5. The final astrometry solution (including the SIP distortion) is derived during the Fine Astrometry procedure as described in Section 3.2.8. In brief, during this two-step approach, an initial WCS+SIP solution is found using the `astrometry.net` package, which is then refined by iteratively running the `scamp` software. As astrometric calibrators, proper motion-corrected Gaia stars are used. Since pipeline version R6.5, the median distortion map created from real observations is used as prior for the SIP solution (instead of the distortion map from ground testing). The derivation of an astrometric solution is challenging as SPHEREx observes regions of different star densities (e.g., compare the galactic bulge to an extragalactic field where the stellar density differs by several 100–1,000×). An iterative approach to select the calibrators and extract sources on the SPHEREx images optimizes this approach, resulting in a very low fraction of failures (<3 %). A significant fraction of failures is due to excessive numbers of pixels flagged as transients. Furthermore, the

Table 26: SPHEREx Photometric Standard Stars.

Star	**Type**	**Band-Averaged Magnitudes (AB)**						σ**(sys)**
		Band 1	Band 2	Band 3	Band 4	Band 5	Band 6	
BD+29 2091‡	F5	**9.94**	**9.97**	**10.32**	**11.04**	11.76	12.03	2–4%
1802271*‡	A2V	12.39	12.84	13.43	14.22	**14.94**	**15.22**	2–4%
Feige110†	sdO	12.70	13.51	14.33	**14.90**	**...**	**...**	2–4%
AGK+81 266†	sdO	12.84	13.68	14.50	**15.08**	**...**	**...**	2–4%
1732526‡	A4V	12.84	13.23	13.87	14.59	**15.31**	**15.59**	2–4%
GRW+70 5824†‡	DA2.4	13.46	14.23	**14.97**	**...**	**...**	**...**	1%
P330E*	G2V	12.66	12.70	13.02	13.78	**14.49**	**14.79**	1%
WD2341+322	DA3.8	13.51	14.10	**...**	**...**	**...**	**...**	1%
P177D	G0V	13.12	13.15	13.49	14.25	**14.95**	**15.25**	2–4%
The three primary *HST* calibrators. They are all white dwarfs, and very blue.								
G191B2B	DA.8	12.62	13.51	14.29	**14.89**	**∼16.0**	**∼16.2**	1%
GD71	DA1.5	13.84	14.70	**15.48**	**16.05**	**∼17.2**	**∼17.5**	1%
GD153	DA1.2	14.17	**15.05**	**15.82**	**16.41**	**∼17.5**	**∼17.8**	1%
The *JWST* Cycle 1 calibrator targets that lie in the NEP EBL field.								
1743045*‡	A8III	13.63	13.91	14.47	**15.20**	**15.93**	**16.20**	2–4%
1757132*‡	A3V	11.94	12.26	12.82	13.55	**14.27**	**14.55**	2–4%
1805292*‡	A4V	12.61	13.00	13.63	14.36	**15.09**	**15.36**	2–4%
1808347*‡	A3V	12.29	12.62	13.20	13.93	**14.66**	**14.93**	2–4%
1812095*‡	A5V	11.96	12.32	12.92	13.65	**14.37**	**14.65**	2–4%
TOTAL STARS:		16	15	12	8	1	1	
TOTAL STARS w/ NEP:		16	15	12	9	6	6	

Notes: All suitable stars from the *HST*/CALSPEC database known to satisfy the brightness and saturation requirements in at least one SPHEREx band. **Bold** indicates either S/N $<$ 50 per observation, or that the star is so bright that it intrudes into the nonlinear regime (BD+29 2091). The models and spectra for all stars listed have been inspected; No other validation has yet been done. In-Band average magnitudes computed only using SPHEREx observations with S/N$>$ 50. † : Model not spanning all six SPHEREx Bands. ∗: Observed with NIRSpec in *JWST* Cycle 1 as part of PID 1678 or as part of the JWST instrumental cross-calibration program. ‡: Used for absolute calibration of the QR data.

large distortion corrections (up to 15 SPHEREx pixels corresponding to ∼90″ in the image corners) require an iterative approach to the final astrometric solution.

In pipeline versions R6.5 and higher (used to process QR-2 data after 12/15/2025), the method to recover a large fraction of exposures which previously failed fine astrometry due to transients and crowding has been further improved. First, the logic of the iteration approach was optimized. It is now run more efficiently, allowing more iterations for exposures that failed previously. Second, another loop was added for failed calculations (meaning non-zero `FINAST` flag) in the original loop. Specifically, in this additional loop a transient flagging was applied to remove affected sources and a restriction to the brightest stars was added. This improves the initial solution and leads to faster and more robust convergence. These improvement led to a reduction of astrometry failures by a factor of two, mostly in the crowded regions of the galactic plane.

In version R7 of the pipeline, an additional step following the main astrometry module was introduced to further reduce the number failed astrometric solutions. Specifically, the astrometry pipeline is rerun for images that failed (`FINAST` not equal to zero) using as prior the WCS and SIP solutions of so-called *seed* images. These were chosen to be images of adjacent small slews, dichroic detector pairs, or any other detectors within a small slew that have successful astrometry (*i.e.* `FINAST` equal to zero). This additional retry logic reduced the number of astrometric failures to sub-percent level.

The success of the astrometric fit is indicated by the `FINAST` flag. Generally, 0 means good astrometry, 1

means partial astrometric solution (expect offsets of a couple of pixels in the image corners where distortion solution is degraded), and everything else means poor astrometric solution (should not be used). Images processed with pipeline version R7 have additional indicators in their headers whether they have gone through the retry logic. These four header keywords include *WCSRETRY*, *RETRY_WCSMODE*, *WCSSEED*, and *WCSSEEDOBS* to indicate that the image run through the retry mode, the retry mode (small slew, dichroic, etc), the detector number of the seed, and the observation ID of the corresponding seed image, respectively (see Section A).

The final astrometric accuracy is tested and quantified by re-extracting bright stars on the images and matching them to the Gaia and 2MASS catalogs. Here we focus on exposures that are not in the SAA and have less than 300,000 pixels flagged as transients (`L2 N_TRANSIENT` flag). The left panel of Figure 20 shows the resulting difference in RA and DEC between extracted star positions and Gaia/2MASS stars for detector 3. We find RMS values of $<0.3''$. No significant changes in the residual are observed towards the corners (where larger distortion is expected), suggesting a robust astrometric solution. The right panel of Figure 20 shows the average distortion for each detector in pixels (1 px $\sim 6.15''$) derived from several hundred exposures. The maximum distortion in the corners of the exposures is $\sim$13 px or $\sim 80''$.

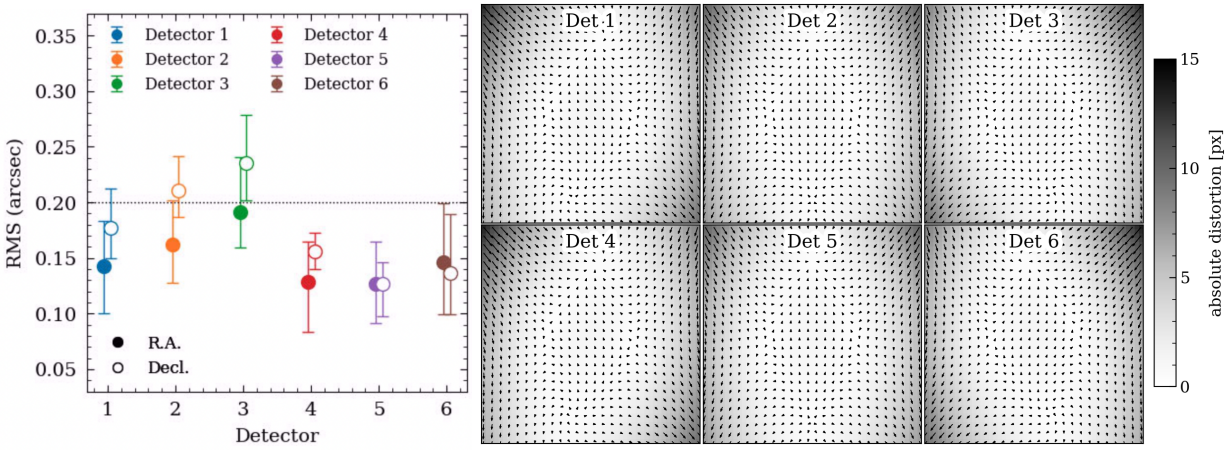

Figure 20: Left: SPHEREx astrometric performance measured after the Level 2 astrometric correction module, showing positional uncertainties (RMS, in arcsec) in Right Ascension (RA, blue circles) and Declination (Decl, red squares) for each detector. The performance has been measured by matching extracted stellar sources to the Gaia DR3 catalog. No statistical difference in performance is observed between the center and the corners of the detector, suggesting a well-fitted distortion solution. Right: Average distortion (in pixels) and its direction obtained across each SPHEREx detector by the Fine Astrometry module.

4.2.3 PSF Measurement

This processing unit generates a finely sampled grid of effective point-spread-function (`ePSF`) models across each detector array. The models are constructed empirically from measurements of isolated stars in the L2 spectral images. The resulting `ePSF` products are one of the key deliverables of the Year 1 release (Sect. 2.1). The corresponding inputs and outputs of this processing step are summarized in Table 27.

The `ePSF` representation was adopted following extensive testing against the previous optical-PSF reconstruction method. In particular, forced-photometry fits performed with the `ePSF` models produced systematically lower fit residuals compared with the previous optical PSF model. `ePSF` models constructed independently from data obtained during different planning periods were also found to be consistent, demonstrating that the PSF is stable with time at the level required for SPHEREx photometry.

Input and Output File Description The inputs to this module include calibrated L2 LVF exposures in units of MJy/sr, formatted as 2,040 × 2,040 detector-pixel arrays. Accurate astrometric solutions from the Fine Astrometry processing step (Sect. 3.2.8) are required to predict the sub-pixel locations of the calibration

Table 27: Inputs and Outputs of the PSF Measurement Module

Input	Output
Spectral images, Fine astrometry information, Gaia DR3 catalog	Effective PSFs

stars. Candidate point sources are selected from the Reference Catalog, including isolated, high-S/N stars from Gaia DR3 [Vallenari et al., 2023] with proper-motion determinations.

The star inputs are restricted to bright, isolated sources that are not bright enough to be affected by detector non-linearity. Measurements containing flagged bad pixels are rejected. A local background model is fitted to each stellar cutout and subtracted before the cutout is given to the `ePSF` reconstruction algorithm. Stars are collected from many spectral images so that each detector zone is represented by several hundred clean stellar measurements spanning a range of sub-pixel positions.

The output is a spatial library of normalized `ePSF` models for each detector. Detectors 1, 2, 4, 5, and 6 are divided into 21×21 zones. Detector 3 is divided into 11×41 zones, with finer sampling along the spectral direction. This denser sampling was found to better capture the more rapid position-dependent changes on Detector 3 associated with birefringence in the dichroic beamsplitter.

Each `ePSF` is sampled at five times the native detector resolution and is stored as a 33×33 array on the oversampled grid. The models and their associated metadata are stored in a FITS binary table, with one row corresponding to each detector zone. The table records the zone indices, its center and dimensions in detector coordinates, the number of stellar measurements used, the mean effective number of pixels, representative wavelength information, and the normalized `ePSF` model.

Meaning of the Effective PSF It should be emphasized that the `ePSF` is not the optical PSF. It describes the distribution of flux recorded by the detector for a point source at a specified sub-pixel position. It therefore includes the optical response together with the detector-pixel response and any other stable effects present in the point-source images. Following the `ePSF` formalism of Anderson and King [2000], the value of the model at a given offset represents the fraction of the total point-source flux expected in a detector pixel whose center has that offset from the source position.

The observed value in detector pixel j for an isolated point source may be written as

$$D_j = F \cdot P_{\rm eff}(x_j - x_\star,\ y_j - y_\star) + B_j + N_j, \tag{24}$$

where F is the source flux, $(x_\star, y_\star)$ is its continuous detector position, (x_j, y_j) is the center of pixel j, B_j is the local background, N_j is noise, and $P_{\rm eff}$ is the `ePSF`. Because $P_{\rm eff}$ describes the response of native detector pixels directly, the detector-pixel response is not deconvolved from the model.

The oversampled array provides a finely sampled numerical representation of $P_{\rm eff}$ and allows the model to be evaluated for arbitrary sub-pixel source positions. The $5\times$ oversampling provides the sampling required to predict the native-resolution pixel values as the source centroid moves within a detector pixel.

Description of Algorithm The construction of the `ePSF` library consists of the following steps:

1. **Identification and binning of point sources:** Bright, isolated stars are identified in the individual spectral images using the SPHEREx Reference Catalog. Sources affected by nearby objects, detector non-linearity, image boundaries, or flagged pixels are excluded. The accepted stellar measurements are assigned to spatial zones according to their detector coordinates.

   Detectors 1, 2, 4, 5, and 6 use a regular 21×21 zoning. Detector 3 uses an 11×41 zoning, with 41 zones along the spectral direction, to model the higher-frequency spatial variations induced by the dichroic beamsplitter. The center and width of every zone are recorded explicitly in the output table.

2. **Extraction and background subtraction:** A native-resolution cutout is extracted around each accepted star. The local background is estimated from a Tractor model fit to the cutout that includes

a free background term. The fitted background is then subtracted before reconstruction. It was found that careful treatment of the background had a significant impact on the `ePSF` model fidelity.

3. **Iterative `ePSF` reconstruction:** The clean stellar cutouts in each zone are supplied to an iterative `ePSF` builder[12] based on the formalism of Anderson and King [2000]. The stars sample a range of sub-pixel centroid positions. Taken together, these measurements constrain the point-source response on a grid finer than the native detector sampling.

   An initial oversampled model is estimated from the ensemble of stellar cutouts. The model is evaluated at the measured position of each star and compared with its native-resolution pixel data. Information from the ensemble of stars is then used to update the oversampled model, and the procedure is repeated until the model is stable or the specified iteration limit is reached. Unlike the previous reconstruction method, this procedure does not construct an optical PSF by explicitly deconvolving the detector-pixel response.

   The reconstruction uses an oversampling factor of five in both detector dimensions. The final model in each zone contains 33×33 oversampled samples and is normalized to unit total flux.

4. **Temporal validation:** The reconstruction and residual tests are repeated using stellar measurements drawn from different planning periods. The resulting models and forced-photometry performance are consistent across these data subsets. This test indicates that the spatially varying `ePSF` solution is stable with time and that a common `ePSF` calibration library can be applied.

5. `ePSF` **library generation:** The final models are written to a FITS binary table with one row per detector zone. Along with the 33×33 model array, each row contains the grid indices `BINX` and `BINY`, the detector-coordinate center and dimensions of the zone, the number of accepted stellar measurements, the mean effective number of pixels, and representative central-wavelength and bandpass information.

Effective size of the PSF ($N_{\rm eff}$): The effective number of pixels over which the PSF is spread is an empirical measure of the PSF size. It is defined as

$$N_{\rm eff} = \frac{\left(\sum_j P_j\right)^2}{\sum_j P_j^2}, \tag{25}$$

where P_j is the fraction of the source flux landing in native detector pixel j. For a model normalized such that $\sum_j P_j = 1$, this reduces to

$$N_{\rm eff} = \frac{1}{\sum_j P_j^2}. \tag{26}$$

Because the native-resolution flux distribution depends on the source's sub-pixel position, the `ePSF` is evaluated at a large number of random source positions distributed in sub-pixel position. For each realization, the model is realized on the native detector pixels, and $N_{\rm eff}$ is calculated from the resulting pixelized point-source model. The reported value, stored as NEFF_MEAN, is the mean over these Monte Carlo sub-pixel realizations. See Figure 21 for the result of this measurement.

$N_{\rm eff}$ provides a compact measure of the area over which the point-source flux is distributed and is directly related to the expected uncertainty of PSF-weighted photometry. Its spatial variation also provides a useful diagnostic of changes in the width and morphology of the point-source response across each detector. The output table additionally records `NSTAR`, the number of accepted stellar measurements contributing to the reconstruction in each zone.

4.3 Additional Products and Inputs

This section describes other calibration products or inputs to the pipeline that are available for users to download at IRSA.

[12] `https://photutils.readthedocs.io/en/stable/api/photutils.psf.EPSFBuilder.html`

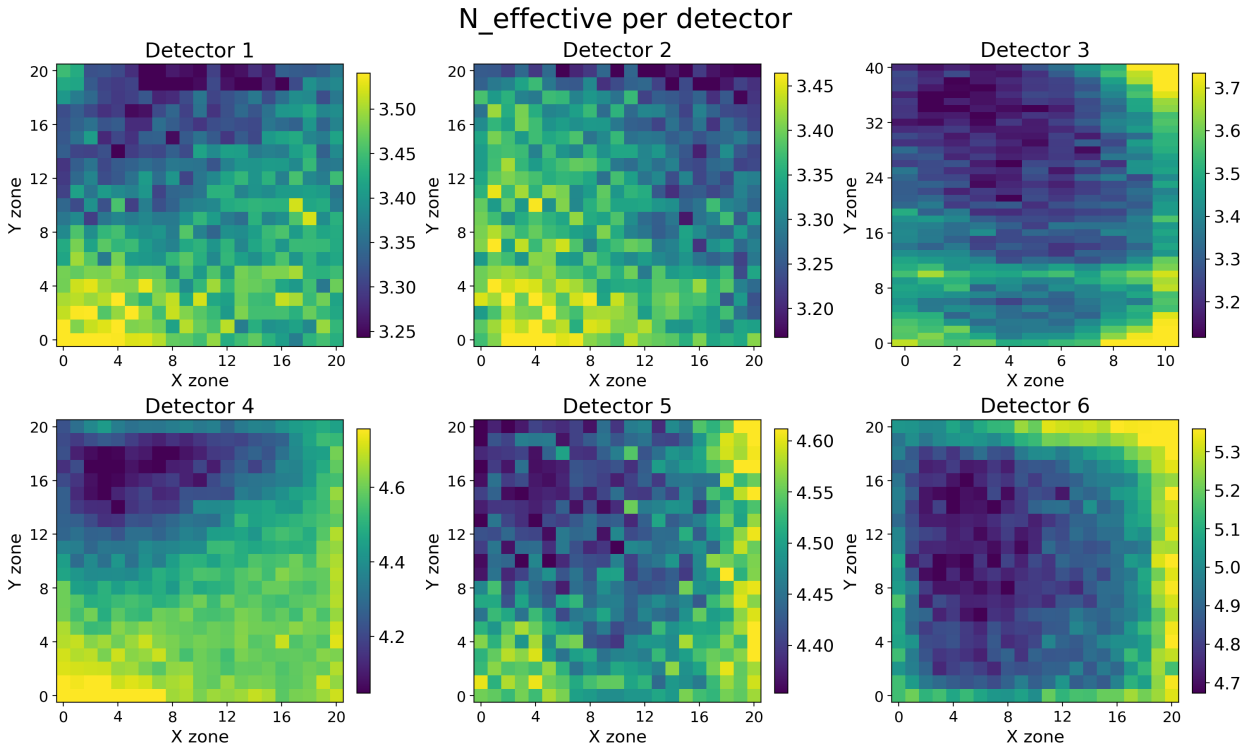

Figure 21: Mean effective number of native detector pixels, $N_{\rm eff}$, for the measured `ePSF` model in each spatial zone. Detectors 1, 2, 4, 5, and 6 use 21×21 zones, while Detector 3 uses 11×41 zones to resolve the more rapid variation along its spectral direction. Each value is the mean of $N_{\rm eff}$ calculated from Monte Carlo realizations of the `ePSF` at different sub-pixel source positions. Note that the color scale changes per detector as the $N_{\rm eff}$ varies with wavelength.

4.3.1 Spectral WCS

The spectral WCS files contain the central wavelengths and bandwidths for each pixel, as extensions in a separate FITS file for each spectral band. The central wavelengths are provided in the `CWAVE` extension, and are set to the point where the cumulative transmission curve reaches 50 % of its total area (i.e., each pixel's transmission curve's median value). The bandwidths are provided in the `CBAND` extension, and are computed as `CWAVE` divided by the detector's measured spectral resolution. The IRSA python notebook includes examples of how to access this product as well as an explanation of the astropy interpretation of the SIP (see `https://caltech-ipac.github.io/irsa-tutorials/tutorials/spherex/spherex_intro.html#b-spectral-wcs`). Users doing science analysis from the calibrated spectral images should use the `CWAVE` and `CBAND` extensions. These files were updated for the QR2 reprocessing (2.1) and all calibrated images for QR2 have been updated to contain the same WAVE-WCS extension, although those before planning period 2025W25_2A list a different file in the header. Instructions on how to access spectral WCS files at IRSA are given at `https://irsa.ipac.caltech.edu/onlinehelp/spherex/#overview`. For users running the spectrophotometry tool at IRSA, this tool switched to the QR2 version of the central wavelength values on December 17, 2025.

The per-pixel values in these extensions are also used to create a compact, piecewise-bilinear model of the spatial variation of the effective wavelength and bandwidth for each detector. This model is encoded using the FITS lookup-table "spectral WCS" standard as a `WAVE-TAB` WCS. This WCS is included in every spectral image, in order to allow an approximate readout of the central wavelength and bandwidth to be packaged with the images without the data volume for the full per-pixel data. This version of the wavelength information is intended for visualization and not for science analysis. The lookup table for the WCS is provided as a binary-table extension, `WCS-WAVE`, in the format mandated by the standard. The WCS

and its lookup table are also included, for reference, in the spectral WCS files, to facilitate comparisons. Table 28 shows a representative header from the spectral WCS file for Detector 1.

Table 28: Spectral WCS FITS Header Keywords (Example)

Header	Value	Units	Description
XTENSION	'IMAGE '	–	Image extension
BITPIX	−32	–	Array data type
NAXIS	2	–	Number of array dimensions
NAXIS1	2040	–	–
NAXIS2	2040	–	–
PCOUNT	0	–	Number of parameters
GCOUNT	1	–	Number of groups
ARRAY	1	–	Detector array
BUNIT	'um '	–	Unit
WCSAXES	2	–	–
WCSNAME	'Approximated per-pixel wavelength and bandpass'	–	–
CTYPE1	'WAVE-TAB'	–	–
CTYPE2	'WAVE-TAB'	–	–
CNAME1	'Wavelength'	–	–
CNAME2	'Bandpass'	–	–
CUNIT1	'um '	–	–
CUNIT2	'um '	–	–
CRPIX1	1	–	–
CRPIX2	1	–	–
CRVAL1	1	–	–
CRVAL2	1	–	–
CDELT1	1	–	–
CDELT2	1	–	–
PC1_1	1	–	–
PC1_2	0	–	–
PC2_1	0	–	–
PC2_2	1	–	–
PS1_0	'WCS-WAVE'	–	Lookup table extension name
PS2_0	'WCS-WAVE'	–	Lookup table extension name
PS1_1	'VALUES '	–	Column name for the coordinate values array
PS2_1	'VALUES '	–	Column name for the coordinate values array
PS1_2	'X '	–	Column name for the indexing vector
PS2_2	'Y '	–	Column name for the indexing vector
PS1_3	1	–	Axis number in coordinate values array
PS2_3	2	–	Axis number in coordinate values array
EXTNAME	'CWAVE '	–	Extension name

4.3.2 Spectral Channels

The spectral channels calibration product includes the definition of 17 spectral channels for each band, used to create image mosaics (Sec. 3.4).

The spectral channel calibration file `spectral_channels_YYYMMDD.fits` contains a 2040×2040 array in which each element corresponds to one detector pixel. The value assigned to each pixel identifies its spectral channel index within the detector. The FITS files also includes a table with the median band center, the range of band center, and the median resolving power R (see below).

The spectral channel map is defined geometrically rather than by the exact calibrated wavelength at each pixel. This convention is adopted because the survey strategy steps in units of spectral channel between

exposures, and these steps are designed to have uniform geometric spacing across the focal plane. The spectral channel definition should therefore be understood as a survey planning coordinate, not as a direct representation of the calibrated wavelength solution.

The curvature visible in the spectral channel boundaries arises from the fabrication of the linear variable filter. The detailed wavelength progression and the spectral calibration of the instrument are described in Hui et al. [2026], Korngut et al. [2026].

The channel values range from 0 to 18. Channels 1 through 17 correspond to the nominal spectral channels used in the mission design. Taken together across Bands 1 through 6, these channels span the nominal wavelength range from 0.75 to 5.0μm. The same geometric definition of spectral channel is applied to every detector, so there is only one FITS file.

Channels 0 and 18 denote pixels outside the nominal survey channel boundaries. These regions correspond to the non rectangular excess areas of the detector footprint, including the edge and corners extensions. Although they are outside the nominal channel set used for survey stepping, spectral information is provided for these pixels so they may be used for calibration, validation, or consistency checks.

For R7, the files for bands 5 and 6 have been updated based on calibration against on sky data, which resulted in a wavelength shift for these bands.

Spectral Band Definition: For each band and spectral channel, the tables below list the median band center λ_c, the range of band center $[\lambda_{\rm min}, \lambda_{\rm max}]$, and the median resolving power R. These values are also included as a table in the FITS file. Channel 0 and 18 correspond to the corners of the detector, and are not part of the nominal design coverage.

Table 29: Band 1

Band	**Channel**	$\lambda_{\mathbf{c}}$	$[\lambda_{\mathbf{min}}, \lambda_{\mathbf{max}}]$	R
1	0	0.741	[0.735, 0.746]	43 ± 1.2
1	1	0.753	[0.743, 0.762]	42 ± 1.1
1	2	0.771	[0.761, 0.781]	42 ± 1.0
1	3	0.790	[0.780, 0.800]	41 ± 0.9
1	4	0.809	[0.798, 0.819]	40 ± 0.9
1	5	0.828	[0.817, 0.839]	40 ± 0.8
1	6	0.848	[0.837, 0.859]	40 ± 0.8
1	7	0.868	[0.857, 0.879]	40 ± 0.7
1	8	0.889	[0.877, 0.900]	39 ± 0.7
1	9	0.910	[0.898, 0.922]	39 ± 0.6
1	10	0.932	[0.920, 0.944]	39 ± 0.6
1	11	0.955	[0.942, 0.967]	39 ± 0.5
1	12	0.978	[0.964, 0.990]	38 ± 0.5
1	13	1.001	[0.988, 1.014]	38 ± 0.5
1	14	1.025	[1.011, 1.039]	38 ± 0.5
1	15	1.050	[1.036, 1.064]	38 ± 0.5
1	16	1.075	[1.061, 1.090]	37 ± 0.4
1	17	1.102	[1.086, 1.116]	37 ± 0.4
1	18	1.117	[1.112, 1.127]	37 ± 0.5

Table 30: Band 2

Band	**Channel**	$\lambda_{\mathbf{c}}$	$[\lambda_{\mathbf{min}}, \lambda_{\mathbf{max}}]$	R
2	0	1.094	[1.085, 1.100]	43 ± 0.7
2	1	1.113	[1.099, 1.126]	43 ± 0.7
2	2	1.139	[1.124, 1.153]	42 ± 0.6
2	3	1.167	[1.152, 1.182]	42 ± 0.5
2	4	1.195	[1.180, 1.210]	41 ± 0.5
2	5	1.224	[1.209, 1.240]	41 ± 0.5
2	6	1.254	[1.238, 1.269]	41 ± 0.4
2	7	1.284	[1.267, 1.300]	42 ± 0.4
2	8	1.315	[1.298, 1.331]	42 ± 0.4
2	9	1.346	[1.329, 1.363]	42 ± 0.4
2	10	1.378	[1.360, 1.396]	42 ± 0.4
2	11	1.412	[1.393, 1.430]	41 ± 0.4
2	12	1.446	[1.426, 1.464]	41 ± 0.3
2	13	1.481	[1.461, 1.500]	41 ± 0.3
2	14	1.517	[1.496, 1.537]	41 ± 0.3
2	15	1.554	[1.533, 1.575]	41 ± 0.3
2	16	1.592	[1.570, 1.613]	41 ± 0.3
2	17	1.631	[1.608, 1.651]	41 ± 0.3
2	18	1.654	[1.647, 1.668]	41 ± 0.3

Table 31: Band 3

Band	**Channel**	$\lambda_{\mathbf{c}}$	$[\lambda_{\mathbf{min}}, \lambda_{\mathbf{max}}]$	R
3	0	1.629	[1.616, 1.637]	42 ± 0.3
3	1	1.656	[1.636, 1.676]	42 ± 0.3
3	2	1.695	[1.675, 1.715]	42 ± 0.3
3	3	1.735	[1.714, 1.756]	41 ± 0.3
3	4	1.775	[1.754, 1.797]	41 ± 0.3
3	5	1.818	[1.795, 1.840]	41 ± 0.3
3	6	1.861	[1.838, 1.884]	41 ± 0.3
3	7	1.905	[1.881, 1.928]	41 ± 0.3
3	8	1.949	[1.925, 1.973]	41 ± 0.3
3	9	1.995	[1.970, 2.019]	41 ± 0.3
3	10	2.041	[2.015, 2.067]	40 ± 0.4
3	11	2.089	[2.062, 2.115]	40 ± 0.3
3	12	2.139	[2.111, 2.165]	40 ± 0.3
3	13	2.189	[2.160, 2.216]	40 ± 0.3
3	14	2.240	[2.211, 2.268]	40 ± 0.3
3	15	2.292	[2.262, 2.321]	40 ± 0.3
3	16	2.345	[2.314, 2.375]	40 ± 0.3
3	17	2.399	[2.367, 2.421]	41 ± 4.0
3	18	2.423	[2.415, 2.439]	61 ± 8.6

Table 32: Band 4

Band	**Channel**	λ_c	$[\lambda_{min}, \lambda_{max}]$	R
4	0	2.414	[2.395, 2.426]	55 ± 3.1
4	1	2.445	[2.422, 2.474]	42 ± 7.6
4	2	2.506	[2.470, 2.542]	34 ± 0.4
4	3	2.575	[2.538, 2.612]	35 ± 0.5
4	4	2.646	[2.607, 2.684]	35 ± 0.5
4	5	2.719	[2.678, 2.758]	35 ± 0.6
4	6	2.794	[2.752, 2.835]	35 ± 0.8
4	7	2.871	[2.828, 2.914]	34 ± 0.6
4	8	2.951	[2.906, 2.995]	34 ± 0.6
4	9	3.033	[2.985, 3.079]	34 ± 0.6
4	10	3.118	[3.069, 3.164]	34 ± 0.6
4	11	3.204	[3.155, 3.252]	35 ± 0.5
4	12	3.293	[3.242, 3.342]	35 ± 0.5
4	13	3.383	[3.330, 3.434]	35 ± 0.6
4	14	3.476	[3.422, 3.528]	36 ± 0.6
4	15	3.570	[3.514, 3.624]	36 ± 0.6
4	16	3.667	[3.610, 3.723]	36 ± 0.8
4	17	3.768	[3.707, 3.827]	36 ± 0.9
4	18	3.831	[3.808, 3.867]	37 ± 1.2

Table 33: Band 5

Band	**Channel**	λ_c	$[\lambda_{min}, \lambda_{max}]$	R
5	0	3.809	[3.798, 3.818]	107 ± 1.1
5	1	3.834	[3.815, 3.852]	109 ± 0.4
5	2	3.867	[3.849, 3.885]	109 ± 0.6
5	3	3.901	[3.882, 3.919]	109 ± 0.4
5	4	3.936	[3.916, 3.954]	109 ± 0.5
5	5	3.970	[3.951, 3.989]	109 ± 0.5
5	6	4.005	[3.986, 4.024]	110 ± 0.6
5	7	4.041	[4.020, 4.059]	110 ± 0.6
5	8	4.076	[4.056, 4.095]	111 ± 0.7
5	9	4.112	[4.091, 4.131]	112 ± 0.6
5	10	4.148	[4.127, 4.167]	113 ± 0.6
5	11	4.184	[4.163, 4.204]	113 ± 0.6
5	12	4.221	[4.199, 4.240]	115 ± 1.1
5	13	4.257	[4.235, 4.277]	114 ± 0.9
5	14	4.294	[4.272, 4.314]	115 ± 0.8
5	15	4.331	[4.308, 4.351]	116 ± 0.9
5	16	4.368	[4.345, 4.388]	116 ± 1.0
5	17	4.405	[4.382, 4.427]	117 ± 1.2
5	18	4.429	[4.420, 4.445]	116 ± 1.8

Table 34: Band 6

Band	**Channel**	$\lambda_{\mathbf{c}}$	$[\lambda_{\mathbf{min}}, \lambda_{\mathbf{max}}]$	R
6	0	4.412	[4.401, 4.420]	124 ± 3.3
6	1	4.435	[4.418, 4.452]	129 ± 1.6
6	2	4.468	[4.450, 4.485]	125 ± 1.1
6	3	4.500	[4.483, 4.518]	127 ± 1.2
6	4	4.533	[4.515, 4.551]	126 ± 1.2
6	5	4.567	[4.548, 4.585]	127 ± 1.3
6	6	4.601	[4.582, 4.619]	126 ± 1.4
6	7	4.635	[4.616, 4.653]	127 ± 1.4
6	8	4.669	[4.650, 4.688]	126 ± 1.7
6	9	4.704	[4.684, 4.723]	128 ± 1.9
6	10	4.739	[4.719, 4.758]	130 ± 3.4
6	11	4.774	[4.753, 4.793]	131 ± 2.4
6	12	4.808	[4.788, 4.827]	132 ± 2.6
6	13	4.843	[4.823, 4.863]	131 ± 2.3
6	14	4.879	[4.858, 4.899]	130 ± 2.5
6	15	4.915	[4.894, 4.936]	131 ± 2.8
6	16	4.952	[4.930, 4.973]	132 ± 3.0
6	17	4.989	[4.966, 5.009]	135 ± 4.3
6	18	5.011	[5.003, 5.025]	135 ± 3.8

4.3.3 Atmospheric Templates

As described in Sec. 3.1, the Level 1 pipeline includes analysis of several atmospheric emission features using template emission line files. The results of these fits are included in the L2 calibrated image header (see Sec. A for keywords) and are NOT subtracted from the data layer. The three templates are:

Auroral Line Template This emission line template covers these atmospheric lines which are generated by excited atoms and molecules in the upper atmosphere, primarily nitrogen (N_2). The lines vary with solar activity, are more frequently seen when SPHEREx is above the polar regions. For R7, correlation is done only for band 1.

- **Data Format:** This product is distributed as one FITS image file with dimensions of 2,040 × 2,040 pixels for band 1. Each file name starts with `aurora_template`.

He Emission Template Bands 1 and 2 include emission from the atmospheric He line at 1.083 μm [Brammer et al., 2014], varying from a factor few to a factor of 30 greater surface brightness than the Zodiacal Light (ZL) background.

- **Data Format:** This product is distributed as two FITS image files with dimensions of 2,040 × 2,040 pixels for band 1 and 2. Each file name starts with `he_template_D`n where n is the band number.

Shuttle Glow Shuttle glow is an emission that arises when spacecraft in low Earth orbit interact with the residual atmosphere, particularly atomic oxygen [Viereck et al., 1991]. As the spacecraft travels through this environment, high-speed atomic oxygen impacts surfaces in the ram direction, exciting surface materials and producing a faint glow, including in the near-infrared. For R7, correlation is done only for band 5.

- **Data Format:** This product is distributed as one FITS image file with dimensions of 2,040 × 2,040 pixels for band 1 and 2. Each file name starts with `shuttle_glow_template`.

4.3.4 Additional Products

Dichroic impacted pixels This bit mask indicates pixels where the flux attenuation due to the dichroic filter is 50 % or higher and corresponds to the `DICHROIC` flag set in Section 3.2.5. The pixel value is 0 for unaffected pixels and 1 for impacted pixels. Note that only Bands 3 and 4 have any non-zero values. These values are supplied by the SPHEREx Instrument Team.

- **Data Format:** This product is distributed as one FITS image file with dimensions of 2,040 × 2,040 pixels per band. Each file name starts with `dichroic_Dn` where n is the band number.

Nonfunctional pixels This bit mask indicates pixels known to be permanently non-functioning and corresponds to the `NONFUNC` flag set in Section 3.2.5. The pixel value is 0 for unaffected pixels and 1 for impacted pixels. These values are supplied by the SPHEREx Instrument Team.

- **Data Format:** This product is distributed as one FITS image file with dimensions of 2,040 × 2,040 pixels per band. Each file name starts with `nonfunc_Dn` where n is the band number.

Non-linearity parameters This file contains the input non-linearity calibration parameters described in Section 3.2.2. The `Q_nl` HDU contains the values used in the equations in Section 3.2.2. The other HDUs represent coefficients that are currently not used in the pipeline but may be in a future version.

- **Data Format:** This product is distributed as one FITS image file with dimensions of 2,040 × 2,040 pixels per band. Each file name starts with `nonlinear_pars_Dn` where n is the band number.

Electronic Gain Factors As described in Section 3.1, the Level 1 data processing includes converting the raw pixel data from ADU to the engineering units of electrons per second. These values are per amplifier channel and are provided by the SPHEREx Instrument Team.

- **Data Format:** These gains are provided in a single YAML file, which includes the provenance information for the detectors and a list of 32 gain values per detector. The file name starts with `gain_factors`.

Read noise parameters This file contains the per-pixel electronic noise used in the variance map calculation (Sect. 3.2.3). The per-pixel values are given in units of electrons and are provided by the SPHEREx Instrument Team.

- **Data Format:** This product is distributed as a single FITS image file with dimensions of 2,040 × 2,040 pixels per band. Each file name starts with `readnoise_pars_Dn`, where n is the band number. The file contains two image extensions:
  - `READOUT-1`: Per-pixel electronic noise for a single readout ($N = 1$).
  - `READOUT-2`: Per-pixel electronic noise for $N = 71$ total reads.

Solid Angle Pixel Map This product is not currently used in the Level 2 pipeline, but is utilized by the photometry measurement (Sec. 3.3) and is provided for reference. It includes a measure of the solid angle per pixel in units of squared arcsec.

- **Data Format:** This product is distributed as one FITS image file with dimensions of 2,040 × 2,040 pixels per band. Each file name starts with `solid_angle_pixel_Dn` where n is the band number.

Initial Distortion in Simple Imaging Polynomials (SIP) This is the initial distortion used by the Fine Astrometry algorithm, expressed as SIP coefficients (Sec. 3.2.8).

- **Data Format:** This product is distributed as one FITS image file per band with the SIP coefficients in the header. Each file name starts with `sip_Dn` where n is the band number.

Crosstalk parameters As described in Sec. 3.2.9, pixels calculate to include electrical crosstalk are masked. These files include the masking parameters. There are currently files for type 1 and type 2 ghosts.

- **Data Format:** This product is distributed as ECSV (Enhanced Character separated value) files, one for each crosstalk type. Each file name starts with `xtalk_classn` where n is the crosstalk type. Type 1 has files for band 1, 2 and 3, while type 2 has files for all 6 bands.

Zodi scaling As described in Sec. 3.2.11, measurements using SPHEREx data showed an amplitude offset to the Kelsall et al. [1998] model. These files contain the scaling used to adjust the Kelsall model for the ZODI layer used in R7.

- **Data Format:** This product is distributed as one ECSV (Enhanced Character separated value) file per band. Each file name starts with `zodi_scaling_D`n where n is the band.

Flux Corrections The absolute gain calibrations were recalculated as part of the Year 1 data release (DR1). To allow users to combine QR2 data using the previous gains with QR3 data using the new gains, this file include the per pixel scaling factors.

- **Data Format:** This product is distributed as one FITS image file with dimensions of 2,040 × 2,040 pixels per band. Each file name starts with `l3_flux_corrections_Dn` where n is the band number.

References

Rachel Akeson, Gregory P. Dubois-Felsmann, Brendan P. Crill, Andreas L. Faisst, Tamim Fatahi, Candice M. Fazar, Tatiana Goldina, Daniel C. Masters, Christina Nelson, Roberta Paladini, Harry I. Teplitz, Gabriela Torrini, Phani Velicheti, Matthew L. N. Ashby, Dan Avner, Yoonsoo P. Bach, James J. Bock, Sean Bruton, Sean A. Bryan, Tzu-Ching Chang, Shuang-Shuang Chen, Asantha Cooray, Ari J. Cukierman, Olivier Doré, C. Darren Dowell, Spencer Everett, Richard M. Feder, Zhaoyu Huai, Howard Hui, Woong-Seob Jeong, Young-Soo Jo, Phil M. Korngut, Yuna G. Kwon, Bomee Lee, Gary J. Melnick, Giulia Murgia, Chi H. Nguyen, Milad Pourrahmani, Zafar Rustamkulov, Teresa Symons, Volker Tolls, Pao-Yu Wang, Yujin Yang, and Michael Zemcov. The SPHEREx Image and Spectrophotometry Processing Pipeline. *ApJS*, 285(2):67, August 2026. doi: 10.3847/1538-4365/ae8843.

Farah Alibay, Oleg V Sindiy, PA Trisha Jansma, Charles M Reynerson, Eric B Rice, Jennifer Rocca, Sara Susca, Stephen C Unwin, Rachel L Akeson, Shannon E Mihaly, et al. Spherex preliminary mission overview. In *2023 IEEE Aerospace Conference*, pages 1–18. IEEE, 2023.

Jay Anderson and Ivan R. King. Toward High-Precision Astrometry with WFPC2. I. Deriving an Accurate Point-Spread Function. *PASP*, 112(776):1360–1382, October 2000. doi: 10.1086/316632.

E Bertin. Automatic astrometric and photometric calibration with scamp. In *Astronomical Data Analysis Software and Systems XV*, volume 351, page 112, 2006.

James J. Bock, Asad M. Aboobaker, Joseph Adamo, Rachel Akeson, John M. Alred, Farah Alibay, Matthew L. N. Ashby, Yoonsoo P. Bach, Lindsey E. Bleem, Douglas Bolton, David F. Braun, Sean Bruton, Sean A. Bryan, Tzu-Ching Chang, Shuang-Shuang Chen, Yun-Ting Cheng, James R. Cheshire, IV, Yi-Kuan Chiang, Jean Choppin de Janvry, Samuel Condon, Walter R. Cook, Asantha Cooray, Brendan P. Crill, Ari J. Cukierman, Olivier Doré, C. Darren Dowell, Gregory P. Dubois-Felsmann, Tim Eifler, Spencer Everett, Beth E. Fabinsky, Andreas L. Faisst, James L. Fanson, Allen H. Farrington, Tamim Fatahi, Candice M. Fazar, Richard M. Feder, Eric H. Frater, Henry S. Grasshorn Gebhardt, Utkarsh Giri, Tatiana Goldina, Varoujan Gorjian, Salman Habib, William G. Hart, Chen Heinrich, Joseph L. Hora, Zhaoyu Huai, Howard Hui, Young-Soo Jo, Woong-Seob Jeong, Jae Hwan Kang, Miju Kang, Branislav Kecman, Chul-Hwan Kim, Jaeyeong Kim, Minjin Kim, Young-Jun Kim, Yongjung Kim, J. Davy Kirkpatrick, Yosuke Kobayashi, Phil M. Korngut, Elisabeth Krause, Bomee Lee, Ho-Gyu Lee, Jae-Joon Lee, Jeong-Eun Lee, Carey M. Lisse, Giacomo Mariani, Daniel C. Masters, Philip D. Mauskopf, Gary J. Melnick, Mary H. Minasyan, Jordan Mirocha, Hiromasa Miyasaka, Anne Moore, Bradley D. Moore, Giulia Murgia, Bret J. Naylor, Christina Nelson, Chi H. Nguyen, Hien T. Nguyen, Jinyoung K. Noh, Stephen Padin, Roberta Paladini, Sung-Joon Park, Konstantin I. Penanen, Dustin S. Putnam, Jeonghyun Pyo, Nesar Ramachandra, Keshav Ramanathan, Zafar Rustamkulov, Daniel J. Reiley, Eric B. Rice, Jennifer M. Rocca, Ji Yeon Seok, Roger Smith, Jeremy Stober, Sara Susca, Harry I. Teplitz, Michael P. Thelen, Volker Tolls, Gabriela Torrini, Amy R. Trangsrud, Stephen Unwin, Phani Velicheti, Pao-Yu Wang, Robin Y. Wen, Michael W. Werner, Abby E. Williams, Ross Williamson, James Wincentsen, Rogier A. Windhorst, Soung-Chul Yang, Yujin Yang, and Michael Zemcov. The SPHEREx Satellite Mission. *ApJ*, 999(1):139, March 2026. doi: 10.3847/1538-4357/ae2be2.

Ralph C. Bohlin, Karl D. Gordon, and P. E. Tremblay. Techniques and Review of Absolute Flux Calibration from the Ultraviolet to the Mid-Infrared. *PASP*, 126(942):711, August 2014. doi: 10.1086/677655.

Ralph C. Bohlin, Szabolcs Mészáros, Scott W. Fleming, Karl D. Gordon, Anton M. Koekemoer, and József Kovács. A New Stellar Atmosphere Grid and Comparisons with HST/STIS CALSPEC Flux Distributions. *AJ*, 153(5):234, May 2017. doi: 10.3847/1538-3881/aa6ba9.

Ralph C. Bohlin, Jessica E. Krick, Karl D. Gordon, and Ivan Hubeny. How Do Spitzer IRAC Fluxes Compare to HST CALSPEC? *AJ*, 164(1):10, July 2022. doi: 10.3847/1538-3881/ac6fe1.

G. Brammer, N. Pirzkal, P. McCullough, and J. MacKenty. Time-varying Excess Earth-glow Backgrounds in the WFC3/IR Channel. Instrument Science Report WFC3 2014-03, 14 pages, April 2014.

Sean Bryan, James Bock, Thomas Burk, Tzu-Ching Chang, Brendan P. Crill, Ari Cukierman, Olivier Doré, C. Darren Dowell, Gregory Dubois-Felsmann, Beth Fabinsky, Sergi Hildebrandt-Rafels, Howard Hui, Kyle Hughes, Phillip Korngut, Philip Mauskopf, Julian Mena, Chi Nguyen, Milad Pourrahmani, Dustin Putnam, Keshav Ramanathan, Flora Ridenhour, Cody Roberson, Amy Trangsrud, Stephen Unwin, and Pao-Yu Wang. Optimized observation sequencing in low-Earth orbit with the SPHEREx survey planning software. *Journal of Astronomical Telescopes, Instruments, and Systems*, 12:027001, April 2026. doi: 10.1117/1.JATIS.12.2.027001.

Brendan P Crill, Michael Werner, Rachel Akeson, Matthew Ashby, Lindsey Bleem, James J Bock, Sean Bryan, Jill Burnham, Joyce Byunh, Tzu-Ching Chang, et al. Spherex: Nasa's near-infrared spectrophotometric all-sky survey. In *Space Telescopes and Instrumentation 2020: Optical, Infrared, and Millimeter Wave*, volume 11443, pages 61–77. SPIE, 2020.

Brendan P. Crill, Yoonsoo P. Bach, Sean A. Bryan, Jean Choppin de Janvry, Ari J. Cukierman, C. Darren Dowell, Spencer W. Everett, Candice Fazar, Tatiana Goldina, Zhaoyu Huai, Howard Hui, Woong-Seob Jeong, Jae Hwan Kang, Phillip M. Korngut, Jae Joon Lee, Daniel C. Masters, Chi H. Nguyen, Jeonghyun Pyo, Teresa Symons, Volker Tolls, Yujin Yang, Michael Zemcov, Rachel Akeson, Matthew L. N. Ashby, James J. Bock, Tzu-Ching Chang, Yun-Ting Cheng, Yi-Kuan Chiang, Asantha Cooray, Olivier Doré, Andreas L. Faisst, Richard M. Feder, and Michael W. Werner. The SPHEREx Sky Simulator: Science Data Modeling for the First All-sky Near-infrared Spectral Survey. *ApJS*, 281(1):10, November 2025. doi: 10.3847/1538-4365/ae04cc.

Ari J. Cukierman, Shuang-Shuang Chen, Jae Hwan Kang, Mary H. Minasyan, Giulia Murgia, James J. Bock, Tzu-Ching Chang, Yi-Kuan Chiang, Brendan P. Crill, Olivier Doré, C. Darren Dowell, Andreas L. Faisst, Joseph L. Hora, Howard Hui, Miju Kang, Phil M. Korngut, Ho-Gyu Lee, Bomee Lee, Gary J. Melnick, Jordan Mirocha, Chi H. Nguyen, Zafar Rustamkulov, Volker Tolls, Michael W. Werner, Yujin Yang, and Michael Zemcov. Spectral Map Making with SPHEREx. *arXiv e-prints*, art. arXiv:2603.25790, March 2026. doi: 10.48550/arXiv.2603.25790.

Candice M. Fazar, Michael Zemcov, C. Darren Dowell, Brendan P. Crill, Chi Nguyen, and Howard Hui. A bestiary of low-level electrical artifacts in SPHEREx flight data. *arXiv e-prints*, art. arXiv:2608.09862, August 2026. doi: 10.48550/arXiv.2608.09862.

Daniel Foreman-Mackey, David W. Hogg, Dustin Lang, and Jonathan Goodman. emcee: The MCMC Hammer. *PASP*, 125(925):306, Mar 2013. doi: 10.1086/670067.

David W. Hogg, Jo Bovy, and Dustin Lang. Data analysis recipes: Fitting a model to data. *arXiv e-prints*, art. arXiv:1008.4686, Aug 2010.

Howard Hui, James J. Bock, Samuel Condon, C. Darren Dowell, Woong-Seob Jeong, Young-soo Jo, Phil M. Korngut, Kenneth Manatt, Chi Nguyen, Hien Nguyen, Stephen Padin, Sung-Joon Park, Jeonghyun Pyo, Yujin Yang, Matthew L. N. Ashby, Yoonsoo P. Bach, Tzu-Ching Chang, Yun-Ting Cheng, Yi-Kuan Chiang, Asantha Cooray, Brendan P. Crill, Ari J. Cukierman, Olivier Doré, Andreas L. Faisst, Joseph L. Hora, Jae Hwan Kang, BoMee Lee, Carey M. Lisse, Daniel C. Masters, Roberta Paladini, Zafar Rustamkulov, Volker Tolls, Michael W. Werner, and Michael Zemcov. Spectral Response of SPHEREx. *ApJS*, 284(1): 10, May 2026. doi: 10.3847/1538-4365/ae522c.

P. D. Hurley, S. Oliver, M. Betancourt, C. Clarke, W. I. Cowley, S. Duivenvoorden, D. Farrah, M. Griffin, C. Lacey, E. Le Floc'h, A. Papadopoulos, M. Sargent, J. M. Scudder, M. Vaccari, I. Valtchanov, and L. Wang. HELP: XID+, the probabilistic de-blender for Herschel SPIRE maps. *MNRAS*, 464(1):885–896, Jan 2017. doi: 10.1093/mnras/stw2375.

Željko Ivezić, Vedrana Ivezić, Joachim Moeyens, Carey M. Lisse, Schelte J. Bus, Lynne Jones, Brendan P. Crill, Olivier Doré, and Joshua P. Emery. Simulated SPHEREx spectra of asteroids and their implications for asteroid size and reflectance estimation. *Icarus*, 371:114696, January 2022. doi: 10.1016/j.icarus.2021.114696.

T. Kelsall, J. L. Weiland, B. A. Franz, W. T. Reach, R. G. Arendt, E. Dwek, H. T. Freudenreich, M. G. Hauser, S. H. Moseley, N. P. Odegard, R. F. Silverberg, and E. L. Wright. The COBE Diffuse Infrared Background Experiment Search for the Cosmic Infrared Background. II. Model of the Interplanetary Dust Cloud. *ApJ*, 508(1):44–73, Nov 1998. doi: 10.1086/306380.

Phil M. Korngut, James J. Bock, Samuel Condon, C. Darren Dowell, Candice M. Fazar, Howard Hui, Bradley D. Moore, Bret J. Naylor, Chi H. Nguyen, Stephen Padin, James Wincentsen, Asad M. Aboobaker, Rachel Akeson, John M. Alred, Farah Alibay, Matthew L. N. Ashby, Yoonsoo P. Bach, Joseph Bichel, Douglas Bolton, David F. Braun, Thomas Brown, Sean A. Bryan, Jill Burnham, Thomas A. Burk, Nicholas Burke, Ben Catching, Tzu-Ching Chang, Shuang-Shuang Chen, Yun-Ting Cheng, Yi-Kuan Chiang, Yong Chong, Asantha Cooray, Walter R. Cook, Velibor Cormarkovic, Brendan P. Crill, Ari J. Cukierman, Andrew Davis, Dan Darga, Thomas Disarro, Olivier Dore, Beth E. Fabinsky, Andreas L. Faisst, James L. Fanson, Allen H. Farrington, Tamim Fatahi, Richard M. Feder, Eric H. Frater, Tatiana Goldina, Varoujan Gorjian, William G. Hart, Warren Hendricks, Joseph L. Hora, Viktor Hristov, Zhaoyu Huai, Charles A. Hulse, Young-Soo Jo, Woong-Seob Jeong, Makenzie L. Kamei, Jae Hwan Kang, Branislav Kecman, Will Marchant, Giacomo Mariani, Daniel C. Masters, Gary J. Melnick, Hiromasa Miyasaka, Giulia Murgia, Christina Nelson, Hien T. Nguyen, Christopher Owen, Roberta Paladini, Sung-Joon Park, Harshad Patil, Konstantin Penanen, Chris Piazzo, Jeonghyun Pyo, Amelia Quon, Keshav Ramanathan, Zafar Rustamkulov, Daniel J. Reiley, Eric B. Rice, Flora Ridenhour, Amber Roberts, Jennifer M. Rocca, Alessandro Signorini, Sara Susca, Volker Tolls, Phani Velicheti, Pao-Yu Wang, Michael W. Werner, Casey White, Ross Williamson, Yujin Yang, and Michael Zemcov. The spherex instrument: Calibration, testing and performance measurements of the nir 2 spectroscopic surveyor from the laboratory to in-orbit commissioning, 2026. URL `https://arxiv.org/abs/2603.29835`.

Russ R. Laher, Jason Surace, Carl J. Grillmair, Eran O. Ofek, David Levitan, Branimir Sesar, Julian C. van Eyken, Nicholas M. Law, George Helou, Nouhad Hamam, Frank J. Masci, Sean Mattingly, Ed Jackson, Eugean Hacopeans, Wei Mi, Steve Groom, Harry Teplitz, Vandana Desai, David Hale, Roger Smith, Richard Walters, Robert Quimby, Mansi Kasliwal, Assaf Horesh, Eric Bellm, Tom Barlow, Adam Waszczak, Thomas A. Prince, and Shrinivas R. Kulkarni. IPAC Image Processing and Data Archiving for the Palomar Transient Factory. *PASP*, 126(941):674, July 2014. doi: 10.1086/677351.

E. Merlin, N. Bourne, M. Castellano, H. C. Ferguson, T. Wang, S. Derriere, J. S. Dunlop, D. Elbaz, and A. Fontana. T-PHOT version 2.0: Improved algorithms for background subtraction, local convolution, kernel registration, and new options. *A&A*, 595:A97, Nov 2016. doi: 10.1051/0004-6361/201628751.

Massimo Robberto. Analysis of the sampling schemes for wfc3-ir. *WFC3 ISR*, 12, 2007.

David L. Shupe, Russ R. Laher, Lisa Storrie-Lombardi, Jason Surace, Carl Grillmair, David Levitan, and Branimir Sesar. More flexibility in representing geometric distortion in astronomical images. In Nicole M. Radziwill and Gianluca Chiozzi, editors, *Software and Cyberinfrastructure for Astronomy II*, volume 8451 of *Society of Photo-Optical Instrumentation Engineers (SPIE) Conference Series*, page 84511M, September 2012. doi: 10.1117/12.925460.

Roger M Smith, Maximilian Zavodny, Gustavo Rahmer, and Marco Bonati. A theory for image persistence in hgcdte photodiodes. In *High energy, optical, and infrared detectors for astronomy III*, volume 7021, pages 180–191. SPIE, 2008.

Kohji Tsumura, Toshio Matsumoto, Shuji Matsuura, Jeonghyun Pyo, Itsuki Sakon, and Takehiko Wada. Low-Resolution Spectrum of the Zodiacal Light with the AKARI InfraRed Camera. *PASJ*, 65:119, Dec 2013. doi: 10.1093/pasj/65.6.119.

Antonella Vallenari, Anthony GA Brown, Timo Prusti, Jos HJ De Bruijne, F Arenou, Carine Babusiaux, Michael Biermann, Orlagh L Creevey, Christine Ducourant, Dafydd Wyn Evans, et al. Gaia data release 3-summary of the content and survey properties. *Astronomy & Astrophysics*, 674:A1, 2023.

RA Viereck, Edmond Murad, B David Green, P Joshi, CP Pike, R Hieb, and G Harbaugh. Origin of the shuttle glow. *Nature*, 354(6348):48–50, 1991.

Martin C. Weisskopf, Paolo Soffitta, Luca Baldini, Brian D. Ramsey, Stephen L. O'Dell, Roger W. Romani, Giorgio Matt, William D. Deininger, Wayne H. Baumgartner, Ronaldo Bellazzini, Enrico Costa, Jeffery J. Kolodziejczak, Luca Latronico, Herman L. Marshall, Fabio Muleri, Stephen D. Bongiorno, Allyn Tennant, Niccolo Bucciantini, Michal Dovciak, Frédéric Marin, Alan Marscher, Juri Poutanen, Pat Slane, Roberto Turolla, William Kalinowski, Alessandro Di Marco, Sergio Fabiani, Massimo Minuti, Fabio La Monaca, Michele Pinchera, John Rankin, Carmelo Sgrò, Alessio Trois, Fei Xie, Cheryl Alexander, D. Zachery Allen, Fabrizio Amici, Jason Andersen, Angelo Antonelli, Spencer Antoniak, Primo Attiná, Mattia Barbanera, Matteo Bachetti, Randy M. Baggett, Jeff Bladt, Alessandro Brez, Raffaella Bonino, Christopher Boree, Fabio Borotto, Shawn Breeding, Daniele Brienza, H. Kyle Bygott, Ciro Caporale, Claudia Cardelli, Rita Carpentiero, Simone Castellano, Marco Castronuovo, Luca Cavalli, Elisabetta Cavazzuti, Marco Ceccanti, Mauro Centrone, Saverio Citraro, Fabio D'Amico, Elisa D'Alba, Laura Di Gesu, Ettore Del Monte, Kurtis L. Dietz, Niccolò Di Lalla, Giuseppe Di Persio, David Dolan, Immacolata Donnarumma, Yuri Evangelista, Kevin Ferrant, Riccardo Ferrazzoli, MacKenzie Ferrie, Joseph Footdale, Brent Forsyth, Michelle Foster, Benjamin Garelick, Shuichi Gunji, Eli Gurnee, Michael Head, Grant Hibbard, Samantha Johnson, Erik Kelly, Kiranmayee Kilaru, Carlo Lefevre, Shelley Le Roy, Pasqualino Loffredo, Paolo Lorenzi, Leonardo Lucchesi, Tyler Maddox, Guido Magazzu, Simone Maldera, Alberto Manfreda, Elio Mangraviti, Marco Marengo, Alessandra Marrocchesi, Francesco Massaro, David Mauger, Jeffery McCracken, Michael McEachen, Rondal Mize, Paolo Mereu, Scott Mitchell, Ikuyuki Mitsuishi, Alfredo Morbidini, Federico Mosti, Hikmat Nasimi, Barbara Negri, Michela Negro, Toan Nguyen, Isaac Nitschke, Alessio Nuti, Mitch Onizuka, Chiara Oppedisano, Leonardo Orsini, Darren Osborne, Richard Pacheco, Alessandro Paggi, Will Painter, Steven D. Pavelitz, Christina Pentz, Raffaele Piazzolla, Matteo Perri, Melissa Pesce-Rollins, Colin Peterson, Maura Pilia, Alessandro Profeti, Simonetta Puccetti, Jaganathan Ranganathan, Ajay Ratheesh, Lee Reedy, Noah Root, Alda Rubini, Stephanie Ruswick, Javier Sanchez, Paolo Sarra, Francesco Santoli, Emanuele Scalise, Andrea Sciortino, Christopher Schroeder, Tim Seek, Kalie Sosdian, Gloria Spandre, Chet O. Speegle, Toru Tamagawa, Marcello Tardiola, Antonino Tobia, Nicholas E. Thomas, Robert Valerie, Marco Vimercati, Amy L. Walden, Bruce Weddendorf, Jeffrey Wedmore, David Welch, Davide Zanetti, and Francesco Zanetti. Imaging X-ray Polarimetry Explorer: prelaunch. *Journal of Astronomical Telescopes, Instruments, and Systems*, 8(2):026002, 2022. doi: 10.1117/1.JATIS.8.2.026002. URL `https://doi.org/10.1117/1.JATIS.8.2.026002`.

Gregory R Zengilowski, Craig W McMurtry, Judith L Pipher, Nicholas S Reilly, William J Forrest, Mario S Cabrera, Meghan L Dorn, Andre F Wong, and AK Mainzer. Signal nonlinearity measurements and corrections in mwir and lwir hgcdte h2rg arrays for neo surveyor. In *X-Ray, Optical, and Infrared Detectors for Astronomy IX*, volume 11454, pages 616–633. SPIE, 2020.

A Spectral Image Header Example

Table A.35: Spectral Image FITS Header Keywords (Example)

Header	Value	Units	Description
XTENSION	'IMAGE '	–	Image extension
BITPIX	−32	–	array data type
NAXIS	2	–	number of array dimensions
NAXIS1	2040	–	
NAXIS2	2040	–	
PCOUNT	0	–	number of parameters
GCOUNT	1	–	number of groups
EXTNAME	'IMAGE '	–	extension name
EXTTYPE	'IMAGE '	–	Extension supports mask overlay
BUNIT	'MJy	–	sr' / Unit of pixel value
DETECTOR	4	–	1-3: SWIR, 4-6: MWIR
OBSID	'2025W17_4B_0458_1'	–	Observation ID
EXPIDN	202517402045814	–	Integer Exposure ID
DATE	'2026-07-15T18:08:42.591'	–	HDU creation time (UTC)
TSAMP	1.5349	s	Interval between pixel readouts (frame)
KOVR_A	15000	adu	Overflow detection limit, active pixels
KOVR_R	15000	adu	Overflow detection limit, ref pixels
KOVR_P	15000	adu	Overflow detection limit, phantom pixels
OVRDLY	5	–	threshold for overflow error flag
SURLIM	77	–	Number of frames detector accumulated charge
SURDLY	3	–	Frame count when SUR sums accumulation begins
TRANDLY	7	–	Frame count when transient detection begins
TCUT	38	–	threshold for transient error flag
KEN_A	20000	adu2	Transient white noise threshold, active pixels
KEN_R	10000	adu2	Transient white noise threshold, ref pixels
KEN_P	500	adu2	Transient white noise threshold, phantom pixels
KSN_A	100	adu	Transient shot noise threshold, active pixels
KSN_R	0	adu	Transient shot noise threshold, ref pixels
KSN_P	0	adu	Transient shot noise threshold, phantom pixels
NSKIP	32	–	Number of rows skipped after a full row is read
NVISITROW	4	–	Number of visits to each reference row
NVISITCOL	1	–	Number of visits to each reference col
MPHAN	4	–	Number of phantom columns reads
NCHANNEL	32	–	Number of readout channels
WCHANNEL	64	–	Number of columns in each readout channel
JREF	8	–	Number of physical reference rows on H2RG
KREF	8	–	Number of physical reference cols on H2RG
JACTIVE	2040	–	Number of light-sensitive pixel rows
KACTIVE	2040	–	Number of light-sensitive pixel cols
SPS_TARGET	'SPS_048902_S12'	–	Extended target ID from Survey Planning

continued . . .

. . . continued

Header	Value	Units	Description
SPS_FLAGS	'all_sky '	–	Flags defined by Survey Planning
OBS_IN_SBAND	'False '	–	Observed during S-band transmission
NON_SURVEY	'False '	–	Observation is not part of a science survey
SGT_LAT_MIDPT	−48.547025	deg	Ground track latitude at midpoint
SGT_LON_MIDPT	179.653626	deg	Ground track longitude at midpoint
SGT_MIN_GCD2SAA	59.897487	deg	Closest ground track dist to SAA
SPS_ELON	310.099010	deg	Ecliptic longitude of planned telescope boresight
SPS_ELAT	−26.235340	deg	Ecliptic latitude of planned telescope boresight
SPS_EPA	0.000000	deg	PA of FP y axis at planned boresight, E of ecl N
DETCOORD	'sky '	–	MWIR pixels flipped on X to match SWIR view
L1DQAFLG	'Pass '	–	L1 DQA outcome
RADESYS	'ICRS '	–	Equatorial coordinate system
X_SC_START	3113.9101252945043	km	Exposure START x position
Y_SC_START	−3072.1030272082908	km	Exposure START y position
Z_SC_START	−5520.412374677981	km	Exposure START z position
VX_SC_START	2.926703004529437	km/s	Exposure START v_x velocity
VY_SC_START	−5.206089393871875	km/s	Exposure START v_y velocity
VZ_SC_START	4.557970719756261	km/s	Exposure START v_z velocity
XYZ_SC_SYSTEM	'GEOCENTER'	–	Reference frame for spacecraft position
VXYZ_SC_SYSTEM	'GEOCENTER'	–	Reference frame for spacecraft velocity
X_SC	3276.206634497534	km	Exposure MID x position
Y_SC	−3365.4370551471857	km	Exposure MID y position
Z_SC	−5248.13638205261	km	Exposure MID z position
VX_SC	2.7176211172748093	km/s	Exposure MID v_x velocity
VY_SC	−4.995455131471378	km/s	Exposure MID v_y velocity
VZ_SC	4.911266255305082	km/s	Exposure MID v_z velocity
X_SC_END	3426.1817585729295	km	Exposure END x position
Y_SC_END	−3646.114056187685	km	Exposure END y position
Z_SC_END	−4956.069575163918	km	Exposure END z position
VX_SC_END	2.4981871870794756	km/s	Exposure END v_x velocity
VY_SC_END	−4.765898733667429	km/s	Exposure END v_y velocity
VZ_SC_END	5.246252160838031	km/s	Exposure END v_z velocity
SNWSTRK	0	–	Saturating streaks from snowball-halo detection
NBLMSRCS	75	–	Number of Saturating Bloomed Srcs
SNW7-5CT	15	–	Early snowball count (first half of exposure)
SNW3-1CT	21	–	Late snowball count (second half of exposure)
SNW2-5CT	2	–	Very early snowball count (frames ~5-7)
SNW6-5CT	2	–	Very early snowball count (before frame ~10)
NSNOWSRC	40	–	Total Number of Snowball Srcs
NBLM5SCS	9	–	Number of Non-Overflow-Bloomed Srcs
L2.N_NONLINEAR	0	–	number of pixels flagged nonlinear
PSTHRESH	0.1	electron/s	persistence threshold
L2.N_PERSIST	2149	–	number of pixels flagged persist
L2.N_HOT	2	–	number of pixels flagged hot

continued . . .

. . . continued

Header	Value	Units	Description
L2.N_COLD	2037	–	number of pixels flagged cold
L2.N_TRAN_NB	24856	–	number of not bad transient pixels
L2.N_PERS_NB	2148	–	number of persistence and not bad pixels
OMEGA_MEDIAN	37.94501214284941	arcsec**2	solid angle pixel map m
OMEGA_STDDEV	0.2007015293130402	arcsec**2	solid angle pixel map
FINAST	0	–	good fine-astrometric solution
WCSAXES	2	–	Number of coordinate axes
CRPIX1	1020.5	–	Pixel coordinate of reference point
CRPIX2	1020.5	–	Pixel coordinate of reference point
PC1_1	−0.00156128637349	–	Coordinate transformation matrix element
PC1_2	−0.000644491133351	–	Coordinate transformation matrix element
PC2_1	−0.000704389040252	–	Coordinate transformation matrix element
PC2_2	0.00158566787328	–	Coordinate transformation matrix element
CDELT1	1.0	deg	Coordinate increment at reference point
CDELT2	1.0	deg	Coordinate increment at reference point
CUNIT1	‘deg’	–	Units of coordinate increment and value
CUNIT2	‘deg’	–	Units of coordinate increment and value
CTYPE1	‘RA—TAN-SIP’	–	TAN (gnomonic) projection + SIP distortions
CTYPE2	‘DEC–TAN-SIP’	–	TAN (gnomonic) projection + SIP distortions
CRVAL1	326.638119318	deg	Coordinate value at reference point
CRVAL2	−41.2871097351	deg	Coordinate value at reference point
LONPOLE	180.0	deg	Native longitude of celestial pole
LATPOLE	−41.2871097351	deg	Native latitude of celestial pole
DAXIS	0.9170387123780545	–	
CONTRAST	54.0	–	
MATCH_NSTARS	953	–	
QS_NMATCH_VAR	0.03940447355861505	–	
ASTRONETSOLVED	T	–	
PXSRCMSK	47.61	–	Percentage of pixels with SOURCE flag
L2.N_SOURCE	1981508	–	number of source flagged pixels
L2.N_XTALK	0	–	number of crosstalk flagged pixels
L2.N_GHOST	0	–	number of ghost flagged pixels
L2.N_GHOST_FPA	0	–	number of ghost_fpa flagged pixels
L2.N_GHOST_EXT	0	–	number of ghost_ext flagged pixels
L2.N_BLOOM_NS	0	–	number of BLOOM flagged pixels not flagged SOURCE
L2.N_SNOW_NS	350	–	number of SNOW flagged pixels not flagged SOURCE
L2.N_OUTLIER	80783	–	number of flagged outlier pixels
L2.SATSTRKS_PXS	0	–	Number of flagged satellite streak pixels
L2.SATSTRKS	0	–	Number of detected satellite streaks
PSF_FWHM	8.672612363488842	arcsec	PSF FWHM Median
HE_AG_MODL	‘[k0 + k1*(X-X0)] * template’	–	He-I airglow fitting model
HE_AG_AMPL	0.570368	–	He-I airglow best-fit model amplitude (k0)
HE_AG_XSLOPE	1.5\1$ˆ{-05}$	–	He-I airglow best-fit model slope (k1)
HE_AG_CHI2R	1.431947	–	He-I airglow best-fit reduced chiˆ2
HE_AG_RMS_PK	0.036069	–	Peak r.m.s of He-I airglow
HE_AG_BKG_MED	0.295114	–	Median bkg value for He-I airglow

continued . . .

. . . continued

Header	Value	Units	Description
HE_AG_BKG_MOD	'n-order 2d-polynomial'	–	Bkg model for He-I airglow
HE_AG_BKG_DEG	2	–	n-order of bkg poly mod for He-I airglow
HE_AG_BKG_COEFF	'c0_0,c0_1,c0_2,c1_0,c1_1,c2_0'	–	He-I bkg mod coeff
HE_AG_BKG_C0_0	0.745467	–	He-I best-fit bkg model c0_0
HE_AG_BKG_C0_1	−0.981728	–	He-I best-fit bkg model c0_1
HE_AG_BKG_C0_2	0.515161	–	He-I best-fit bkg model c0_2
HE_AG_BKG_C1_0	−4.9E-05	–	He-I best-fit bkg model c1_0
HE_AG_BKG_C1_1	6.8\1^{-05}	–	He-I best-fit bkg model c1_1
HE_AG_BKG_C2_0	−0.0	–	He-I best-fit bkg model c2_0
AURORA_CORR	0.0	–	Correl coeff with aurora template
SHUTTLE_GLOW_CORR	0.0	–	Correl coeff with shuttle-glow template
HE_AIRGLOW_CONT	F	–	True for detectors 1 and 2, False otherwise
SHUTTLE_GLOW_CONT	F	–	True if SHUTTLE_GLOW_CORR > 0.2
AURORA_CONT	F	–	True if AURORA_CORR > 0.2
L2DQAFLG	'Pass '	–	L2 DQA outcome
L2.N_TRANSIENT	35114	–	number of flagged flagged transient pixels
L2.N_OVERFLOW	2709	–	number of flagged overflow pixels
L2.N_SUR_ERROR	22645	–	number of flagged sur error pixels
L2.N_NONFUNC	22468	–	number of flagged nonfunctional pixels
L2.N_DICHROIC	112375	–	number of flagged pixels due to low efficiency
L2.N_MISSING	0	–	number of flagged pixels with missing data
L2.N_FULLSAMPLE	240	–	number of flagged full-sample pixels
L2.N_PHANMISS	0	–	number of flagged phanmiss pixels
L2.N_SNOWBALL	692	–	number of flagged snowball artifact pixels
L2.N_BLOOM	1555	–	number of flagged bloom artifact pixels
L2.N_HALO	79233	–	number of flagged transient halo pixels
L2.N_SAT_HALO	0	–	number of flagged streak halo pixels
A_ORDER	3	–	SIP polynomial order, axis 0, detector to sky
A_0_0	0.481698797086	–	SIP distortion coefficient
A_0_1	−0.000666079270444	–	SIP distortion coefficient
A_0_2	−1.42891241405E-06	–	SIP distortion coefficient
A_0_3	−5.8912710055E-11	–	SIP distortion coefficient
A_1_0	−0.000342078143197	–	SIP distortion coefficient
A_1_1	4.23814367317\1^{-06}	–	SIP distortion coefficient
A_1_2	6.42965612423\1^{-10}	–	SIP distortion coefficient
A_2_0	−1.58704697621E-06	–	SIP distortion coefficient
A_2_1	−2.01592724458E-10	–	SIP distortion coefficient
A_3_0	5.90778148414\1^{-10}	–	SIP distortion coefficient
B_ORDER	3	–	SIP polynomial order, axis 1, detector to sky
B_0_0	−1.14078669042	–	SIP distortion coefficient
B_0_1	−0.000584886219203	–	SIP distortion coefficient
B_0_2	1.91762345617\1^{-06}	–	SIP distortion coefficient
B_0_3	3.87846110345\1^{-10}	–	SIP distortion coefficient
B_1_0	−8.18453574726E-05	–	SIP distortion coefficient
B_1_1	−7.61577573871E-07	–	SIP distortion coefficient
B_1_2	−1.49882848608E-10	–	SIP distortion coefficient
B_2_0	6.76166519654\1^{-06}	–	SIP distortion coefficient
B_2_1	6.82727563049\1^{-10}	–	SIP distortion coefficient
B_3_0	−3.93615188176E-11	–	SIP distortion coefficient
AP_ORDER	3	–	SIP polynomial order, axis 0, sky to detector

continued . . .

. . . continued

Header	Value	Units	Description
AP_0_0	−0.478585431326	–	SIP distortion coefficient
AP_0_1	0.000672384220539	–	SIP distortion coefficient
AP_0_2	1.42053003732\1^{-06}	–	SIP distortion coefficient
AP_0_3	4.63338683443\1^{-11}	–	SIP distortion coefficient
AP_1_0	0.000334798118752	–	SIP distortion coefficient
AP_1_1	−4.22074803958E-06	–	SIP distortion coefficient
AP_1_2	−6.08514699101E-10	–	SIP distortion coefficient
AP_2_0	1.57477347604\1^{-06}	–	SIP distortion coefficient
AP_2_1	1.5636041651\1^{-10}	–	SIP distortion coefficient
AP_3_0	−5.55682167248E-10	–	SIP distortion coefficient
BP_ORDER	3	–	SIP polynomial order, axis 1, sky to detector
BP_0_0	1.13629182474	–	SIP distortion coefficient
BP_0_1	0.000579672109301	–	SIP distortion coefficient
BP_0_2	−1.90854552394E-06	–	SIP distortion coefficient
BP_0_3	−3.78788641072E-10	–	SIP distortion coefficient
BP_1_0	8.96226932925\1^{-05}	–	SIP distortion coefficient
BP_1_1	7.44789243453\1^{-07}	–	SIP distortion coefficient
BP_1_2	1.21422023514\1^{-10}	–	SIP distortion coefficient
BP_2_0	−6.74979582821E-06	–	SIP distortion coefficient
BP_2_1	−5.96514994393E-10	–	SIP distortion coefficient
BP_3_0	1.23709292361\1^{-11}	–	SIP distortion coefficient
WCSAXESA	2	–	Number of coordinate axes
CRPIX1A	1.0	–	Pixel coordinate of reference point
CRPIX2A	1.0	–	Pixel coordinate of reference point
CDELT1A	1.0	pixel	Coordinate increment at reference point
CDELT2A	1.0	pixel	Coordinate increment at reference point
CUNIT1A	‘pixel’	–	Units of coordinate increment and value
CUNIT2A	‘pixel’	–	Units of coordinate increment and value
CTYPE1A	‘LINEAR’	–	Coordinate type code
CTYPE2A	‘LINEAR’	–	Coordinate type code
CRVAL1A	0.0	pixel	Coordinate value at reference point
CRVAL2A	0.0	pixel	Coordinate value at reference point
LATPOLEA	90.0	deg	Native latitude of celestial pole
WCSNAMEA	‘0-based active pixel coordinates’	–	Coordinate system title
TIMESYS	‘UTC’	–	Time scale
MJDREF	0.0	d	MJD of fiducial time
DATE-OBS	‘2025-04-27T18:35:50.023’	–	ISO-8601 time of observation
MJD-OBS	60792.774884525	d	MJD of observation
DATE-BEG	‘2025-04-27T18:35:50.023’	–	ISO-8601 time at start of observation
MJD-BEG	60792.774884525	d	MJD at start of observation
DATE-AVG	‘2025-04-27T18:36:47.582’	–	ISO-8601 time at midpoint of observation
MJD-AVG	60792.775550715	d	MJD at midpoint of observation
DATE-END	‘2025-04-27T18:37:45.140’	–	ISO-8601 time at end of observation
MJD-END	60792.776216904	d	MJD at end of observation
XPOSURE	113.5826	s	Exposure (integration) time
TELAPSE	118.1873	s	Elapsed time (start to stop)
WCSAXESW	2	–	Two output axes: wavelength and bandwidth

continued . . .

. . . continued

Header	Value	Units	Description
WCSNAMEW	'Approximated per-pixel wavelength and bandwidth'	–	WCS label
CNAME1W	'Wavelength'	–	First output axis is central wavelength
CNAME2W	'Bandwidth'	–	Second output axis is bandwidth
CRPIX1W	1	–	Lookup table is in raw FITS coordinates
CRPIX2W	1	–	Lookup table is in raw FITS coordinates
CDELT1W	1	pixel	Lookup table is in raw FITS coordinates
CDELT2W	1	pixel	Lookup table is in raw FITS coordinates
CUNIT1W	'um '	–	Wavelength is reported in microns
CUNIT2W	'um '	–	Bandpass is reported in microns
CTYPE1W	'WAVE-TAB'	–	Bilinear lookup table, FITS Paper 3, Sect 6.1
CTYPE2W	'WAVE-TAB'	–	Bilinear lookup table, FITS Paper 3, Sect 6.1
CRVAL1W	1	pixel	Lookup table is in raw FITS coordinates
CRVAL2W	1	pixel	Lookup table is in raw FITS coordinates
PV1_3W	1	–	Index of wavelength in VALUES array
PV2_3W	2	–	Index of bandwidth in VALUES array
PS1_0W	'WCS-WAVE'	–	Extension with wavelength lookup table
PS2_0W	'WCS-WAVE'	–	Extension with bandwidth lookup table
PS1_1W	'VALUES '	–	Column with values for wavelength
PS2_1W	'VALUES '	–	Column with values for bandwidth
PS1_2W	'X '	–	Column with control points for detector in X
PS2_2W	'Y '	–	Column with control points for detector in Y
COMMENT	TELAPSE ends at MJD-END, starts prior to MJD-BEG:		
COMMENT	includes discarded frames		
COMMENT	XPOSURE is the scientifically meaningful exposure time:		
COMMENT	the time between the start and end of collecting data that		
COMMENT	contributes to the photocurrent		
HISTORY	GDS Image Association, SSDC-MS-002 v2.1.1		
HISTORY	Estimate Coarse Astrometry, SSDC-MS-003 v2.4		
HISTORY	Convert to Engineering Units, SSDC-MS-005 v3.2		
HISTORY	Correct Preamplifier, SSDC-MS-006 v1.5		
HISTORY	Create Image Data Files, SSDC-MS-007 v1.2.1		
HISTORY	Perform Data Quality Assessment for Level 1, SSDC-MS-009 v1.3		
HISTORY	[CALIB] dichroic 019f521b-3547-7804-8fac-f144308ff47a		
HISTORY	[CALIB] gain_factors 019f521b-4ad3-7698-b7c3-a40aefa6469e		
HISTORY	[CALIB] initial_distortion_table 019f521b-605a-79ba-ab36-caf4d55f5d5e		
HISTORY	[CALIB] nonfunc_v2 019f521b-b4f6-7eaa-b8fa-d2bb1fa9c0a2		
HISTORY	[CALIB] sband_mnemonics 019f521c-f507-7801-8542-ad9eb4fc903d		
HISTORY	[CALIB] spectral_wcs 019f4f99-3265-766b-b368-e28eb08fdbed		
HISTORY	GDS Image Association, SSDC-MS-002 v2.1.1		
HISTORY	Source blooming and cosmic ray halo flagging, SSDC-MS-0011 v1		
HISTORY	Correct Non-Linearity, SSDC-MS-010 v3.2		
HISTORY	Create Variance Map, SSDC-MS-011 v4.2		
HISTORY	Update Persistence Mask, SSDC-MS-012 v2.2.1		
HISTORY	[CALIB] gain_factors 019f521b-4ad3-7698-b7c3-a40aefa6469e		
HISTORY	[CALIB] nonlinear_pars 019f521c-358f-7a49-820c-fa015710cdc2		

continued . . .

. . . continued

Header	Value	Units	Description
HISTORY	[CALIB] readnoise_pars 019f521c-b665-77e2-a0c0-de0b531467f9		
HISTORY	Apply Bad Pixel Mask, SSDC-MS-013 v1.1		
HISTORY	Apply Flat Field and Photometric Calibration, SSDC-MS-014 v1.5		
HISTORY	Estimate Fine Astrometry, SSDC-MS-016 v2.5		
HISTORY	Create Source Mask, SSDC-MS-019 v3.5		
HISTORY	Detect Outlier Pixels, SSDC-MS-020 v1.4		
HISTORY	Get Zodi Model, SSDC-MS-022 v2.3		
HISTORY	Measure Per-Exposure PSF, SSDC-MS-023 v3.3		
HISTORY	Create Spectral Image, SSDC-MS-024 v2.2		
HISTORY	Perform Data Quality Assessment for Level 2, SSDC-MS-025 v1.4		
HISTORY	[CALIB] abs_gain_matrix 019f4f95-6173-79cb-872b-f0f8abd8ed65		
HISTORY	[CALIB] dark 019f4f96-1086-7845-9c97-d9a1076a80ed		
HISTORY	[CALIB] epsf 019f4f97-864d-7bee-8722-a634bea7288f		
HISTORY	[CALIB] sip 019f4f98-7f49-79e3-9a45-85e5641166aa		
HISTORY	[CALIB] spectral_wcs 019f4f99-3265-766b-b368-e28eb08fdbed		
HISTORY	[CALIB] xtalk_class2 019f521e-5e08-7cfe-942e-3cbb4851b510		
HISTORY	[CALIB] zodi_scaling 019f521d-4ada-70e7-a05f-b9791f90089b		
Primary HDU			
SIMPLE	T	–	Conforms to FITS standard
BITPIX	8	–	Array data type
NAXIS	0	–	Number of array dimensions
EXTEND	T	–	

Notes: The image extension is identified by `EXTNAME = 'IMAGE'` and `EXTTYPE = 'IMAGE'`, while the corresponding flags extension uses `EXTNAME = 'FLAGS'` and `EXTTYPE = 'MASK'`. The designation `EXTTYPE = 'MASK'` indicates that the values within the extension represent bit masks, where each bit encodes a distinct flag condition.
`HISTORY` and `COMMENT` are excluded from this example.

A.1 Transient Flags

The ICE flight software includes Transient flagging designed to reduce the effects of cosmic rays on the reported photocurrents. As an exposure proceeds, and for each detector pixel, the Transient detection algorithm compares the current readout value of the pixel with a prediction based on the prior four reads. If the difference is statistically unlikely (as quantified by configurable parameters), then the Transient flag is set and the reported photocurrent is based only on reads before the Transient event. This algorithm is applied starting with the 7th readout frame following detector reset (as determined by the TRANDLY parameter). The detailed condition for detecting a transient is as follows:

$$(2y_i - 2y_{i-1} - y_{i-2} + y_{i-4})^2 > 4 \times KEN + KSN \times (y_{i-1} - y_{i-4} - 3m) \quad (27)$$

Index i refers to the current readout frame, and $[y_{i-1} + (y_{i-2} - y_{i-4})/2]$ is an optimized predictor for the current read value y_i. The first term on the right-hand side of the equation is designed to look for statistical outliers for an approximately gaussian distribution of noise (applicable at low photocurrent), and the second term loosens the threshold to account for Poisson noise at higher photocurrent. The unit of y is ADU; 1 ADU corresponds roughly to 1 electron (see Electronic Gain Factors for a more accurate conversion). m is the amplifier drift rate measured during the prior exposure.

KEN and KSN are configurable parameters which could be updated at some point during the mission, but have been fixed from the start of commissioning to date. Different values are used for the three types of H2RG and amplifier signals read, as specified in Table A.35. If the Transient is detected when the frame index is less than TCUT, then the SUR_ERROR flag is set also (see Tables 16 and 14).

For the current value of KEN_A which is 20000, the Transient detection threshold is $\geq \frac{1}{2}\sqrt{4 \times KEN} =$ 141 ADU $\approx$ 100 e-. The effect on photocurrent of undetected transients below this threshold depends on when during the exposure that the transient occurred.

B Absolute Gain Matrix Header Example

Table B.1: Absolute Gain Matrix Header Keywords (Example)

Header	Value	Units	Description
XTENSION	'IMAGE '	–	Image extension
BITPIX	−32	–	Array data type
NAXIS	2	–	Number of array dimensions
NAXIS1	2040	–	Length of axis 1
NAXIS2	2040	–	Length of axis 2
PCOUNT	0	–	Number of parameters
GCOUNT	1	–	Number of groups
BUNIT	'MJy s / (electron sr)'	–	Unit of pixel value
EXTNAME	'IMAGE '	–	Extension name

C Average EPSF Header Example

Table C.1: Spectral Image FITS Header Keywords (Example)

Header	Value	Units	Description
XTENSION	'BINTABLE'	–	binary table extension
BITPIX	8	–	array data type
NAXIS	2	–	number of array dimensions
NAXIS1	8752	–	length of dimension 1
NAXIS2	441	–	length of dimension 2
PCOUNT	0	–	number of group parameters
GCOUNT	1	–	number of groups
TFIELDS	11	–	number of table fields
EXTNAME	'EPSF '	–	extension name
DETECTOR	'1 '	–	1-3: SWIR, 4-6: MWIR
OVSMPX	5	–	
OVSMPY	5	–	
MAXIT	10	–	
SMOOTH	'quartic '	–	
JUNKCLN	1	–	
KEEPNAT	3.5	–	
KEEPOS	17.5	–	
DETCOORD	'sky '	–	MWIR pixels flipped on X to match SWIR view
ORDERING	'x-fast then y'	–	
BINSRC	'filename'	–	
GEOMSRC	'uniform active-pixel tiling'	–	
NEFFSRC	'stats table exact filename match'	–	
WVMSRC	'stats table exact filename match'	–	
CWAVESRC	'spectral_wcs CWAVE'	–	
CBANDSRC	'spectral_wcs CBAND'	–	
TTYPE1	'BINX '	–	
TFORM1	'J '	–	
TTYPE2	'BINY '	–	
TFORM2	'J '	–	
TTYPE3	'XCENTER '	–	
TFORM3	'E '	–	
TUNIT3	'pixel '	–	
TTYPE4	'YCENTER '	–	
TFORM4	'E '	–	
TUNIT4	'pixel '	–	
TTYPE5	'XWIDTH '	–	
TFORM5	'E '	–	
TUNIT5	'pixel '	–	
TTYPE6	'YWIDTH '	–	
TFORM6	'E '	–	
TUNIT6	'pixel '	–	
TTYPE7	'NSTAR '	–	
TFORM7	'J '	–	

continued . . .

. . . continued

Header	Value	Units	Description
TTYPE8	'NEFF_MEAN'	–	
TFORM8	'E '	–	
TTYPE9	'CWAVE '	–	
TFORM9	'E '	–	
TUNIT9	'um '	–	
TTYPE10	'CBAND '	–	
TFORM10	'E '	–	
TUNIT10	'um '	–	
TTYPE11	'EPSF '	–	
TFORM11	'1089D '	–	
TDIM11	'(33,33) '	–	
HISTORY	Headers standardized by SSDC on 2026-06-26T22:53:35.593 (UTC)		
HISTORY	Calibration source file: epsf_1_20260507.fits		
	Primary HDU		
SIMPLE	T	–	Conforms to FITS standard
BITPIX	8	–	Array data type
NAXIS	0	–	Number of array dimensions
EXTEND	T	–	

Notes: The image extension is identified by EXTNAME = 'IMAGE' and EXTTYPE = 'IMAGE', while the corresponding flags extension uses EXTNAME = 'FLAGS' and EXTTYPE = 'MASK'. The designation EXTTYPE = 'MASK' indicates that the values within the extension represent bit masks, where each bit encodes a distinct flag condition.
HISTORY and COMMENT are excluded from this example.

D List of Acronyms

ADCS Attitude Determination and Control Subsystem . . . 5
ADU Analog Digital Units . . . 21
ASIC Application-Specific Integrated Circuit . . . 7
BAE BAE Space and Mission Systems . . . 9
Caltech California Institute of Technology . . . 5
CDH Command and Data Handling . . . 5
CDS Correlated Double Sampling . . . 27
DAPHNE Data Acquisition Processing & Handling Network Environment . . . 21
DBS Dichroic Beam Splitter . . . 15
DR Data Release . . . 11
EPDS Electrical Power Distribution Subsystem . . . 5
EBL Extragalactic Background Light . . . 4
ESO European Southern Observatory . . . 14
FITS Flexible Image Transport System . . . 14
FoV Field of View . . . 5
FPA Focal Plane Assemblies . . . 5
FSW Flight Software . . . 5
GDS Ground Data System . . . 21
HDU Header and Data Unit . . . 13
ICE Instrument Control Electronics . . . 5
IOC In-Orbit Checkout . . . 4
IRSA NASA/IPAC Infrared Science Archive . . . 9
IXPE Imaging X-ray Polarimetry Explorer . . . 4
JPL Jet Propulsion Laboratory . . . 9
KASI Korea Astronomy and Space Science Institute . . . 9
LEO low Earth orbit . . . 4
LVF Linear Variable Filter . . . 5
MEF Multi-Extension FITS . . . 11
MIDEX Medium-class Explorer . . . 4
MLTAN Mean Local Time of Ascending Node . . . 5
MOS Mission Operations System . . . 22
MWIR Mid-wave Infrared . . . 7
NIR Near-infrared . . . 4
NL Non-Linearity . . . 26
NSN Near Space Network . . . 9
PGSO Planning Generation and Simulation Operations . . . 10
PA Position Angle . . . 8
PI Principal Investigator . . . 9
PSF Point Spread Function . . . 13
QR Quick Release . . . 11
SAA South Atlantic Anomaly . . . 40
SIP Simple Imaging Polynomial . . . 33
SPS Survey Planning Software . . . 7
SSDC SPHEREx Science Data Center . . . 9
SSIRU Scalable Space Inertial Reference Unit . . . 5

SST SPHEREx Science Team 9
S/N Signal-to-Noise 7
SUR Sample-Up-the-Ramp 6
SWIR Short-wave Infrared 7
TMA Three Mirror Anastigmat 5
TPV Tangent plane projection with parameter value (PV) polynomial distortion terms 35
2MASS Two Micron All Sky Survey 33
WCS World Coordinate System 13
WISE Wide-field Infrared Survey Explorer 33
ZL Zodiacal, or Zodi Light 17